
# Modelling of Petroleum Wastewater Photodegradation in a Fluidized Bed Reactor

Thesis

M–Tech. Chemical Engineering

In the Faculty of Engineering and Technology

Surname and initial: Nyembe N

Student No: 209119594

Highest qualification of student: BTech. Chemical Engineering

Supervisor: Prof. Ochieng Aoyi

Co-supervisor: Ms L. Lerotholi

April 2018

# List of publications

## Conference papers

MHLANGA, R.J., NYEMBE, N., CHIRIRIWA, H. & OCHIENG, A. (2016). Hydrodynamic conditions and photodegradation of methyl orange in a fluidized bed reactor. *International Journal of Research in Chemical, Metallurgical and Civil Engineering (IJRCMCE)*. 3(1). p. 170.

NYEMBE, N., OCHIENG, A. & LETSABISA, L. (2016). CFD simulation of a fluidized bed reactor for petroleum wastewater photodegradation, *10th South African Conference on Computational and Applied Mechanics*. Potchefstroom. p. 1-10.

# Abstract

Petroleum wastewater is highly contaminated with toxic organic pollutants that are harmful to the environment. The heterogeneous photocatalytic oxidation (HPO) process has shown the ability to remove these pollutants through the application of a fluidized bed reactor (FBR). The purpose of the study was to apply response surface modelling (RSM) and computational fluid dynamics (CFD) to optimize the operating conditions for the photodegradation process in an FBR. This was done by investigating the hydrodynamics, photodegradation efficiency and reaction kinetics; that gave a holistic view on the performance of the FBR.

The hydrodynamic study focused on modelling the axial liquid velocity, gas hold-up and turbulence quantities due to their substantial impact on the design and performance of the FBR. This was done by implementing the Eulerian-Eulerian approach which solves the continuity and momentum equations for each phase. In addition, the standard $k$-$\varepsilon$ turbulence model was used to capture the turbulent characteristics in the liquid phase. A numerical optimization technique (desirability) was used to determine the optimal simulation setting methods; that were found to be a fine grid size (500 000 cells), 2nd Order Upwind discretization scheme and a small time step size (0.001) and gave the best desirability (0.985). The axial liquid velocity was maximal towards the centre of the reactor and decreased towards the wall. The same trend was seen with the local gas hold-up, where it was high towards the centre and low near the wall region. This was an indication that the bubbles tended to gather towards the central region as they move up. Furthermore, the bubbles had a spherical–like shape due to the low superficial gas velocity and operating within the homogeneous regime. The turbulent kinetic energy increased at distances away from the distributor region, due to the bubbles accelerating, and it balanced well with the energy introduced by the bubbles.

Central composite design (CCD), which is a type of response surface modelling technique, was used to investigate and optimize the photodegradation operating parameters. The maximal degradation efficiency in the current study was found to be 65.9%, which was relatively low when compared to literature (80.84%). This was attributed to the increase in the catalyst particle size from nanometer to micrometer. Furthermore, the second-order empirical model that was developed, using the analysis of variance (ANOVA), presented a sufficient correlation to the photodegradation experimental data. The optimal photodegradation operating conditions were found to be: superficial gas velocity of 17.32 mm/s, composite catalyst loading of 1.0 g/L,

initial pH level of 3.5 and reaction time being 210 min. Using the Langmuir-Hinshelwood model, it was found that the photocatalytic degradation of petroleum wastewater follows pseudo first-order reaction kinetics. Since the photocatalytic degradation mechanism of phenol follows three stages whereby the second stage is the photocatalytic degradation on the surface of the catalyst to form by-products. This is the rate dominant stage and follows the pseudo first-order reaction kinetics.

# Table of Contents

## List of Figures

## List of Tables

## Acknowledgement

I would like to convey my sincere gratitude and heartfelt thankfulness to both my supervisor and co-supervisor who helped me during my studies at the Vaal University of Technology (VUT).

Primarily my supervisor, Prof. Ochieng Ayoi, who provided me with an opportunity to enrol for my Master's degree at the Vaal University of Technology under the department of Chemical Engineering. Under his supervision, he introduced me to a complex field called computational fluid dynamics (CFD) and with his guidance, I could grasp and apply the few concepts of CFD into my research. Not only was he a supervisor, but he also played a role of a parent where from time-to-time he would give me advice relating to finance, social life, relationships and how to juggle that cocktail mixture into my research. On the other hand, Ms Letsabisa Lerotholi (co-supervisor) complemented the supervision umbrella by adding value to my research, career and spiritual life. She challenged my approach to research and was my pillar of light during the dark days of research.

Other stakeholders that were significant in my research was the VUT Mechanical Engineering department that provided me with the software ANSYS fluent that I used to conduct my CFD simulations. I am also thankful to the Water Research Commission (WRC) and the National Research Foundation (NRF) that funded both my research and personal needs.

## Acronyms

| | |
|---|---|
| AOP | Advanced Oxidation Process |
| ANOVA | Analysis of Variance |
| ASSE | Average Sum of Square Error |
| CWAO | Catalytic Wet Air Oxidation |
| CCD | Central Composite Design |
| CFD | Computational Fluid Dynamics |
| CFM | Cross-Flow Microfiltration |
| DEA | Diethanolamine |
| DNS | Direct Numerical Simulation |
| DMS | Dynamic Smagorinsky Model |
| GLSCFBPR | Gas-Liquid-Solid Circulating Fluidized Bed Reactor |
| HPO | Heterogeneous Photocatalytic Oxidation |
| L-H | Langmuir-Hinshelwood |
| LDA | Laser Doppler Anemometry |
| LES | Large Eddy Simulation |
| MS | Media of the Square |
| MUSIG | Multiple Size Group |
| PIV | Particle Image Velocimetry |
| PW | Petroleum Wastewater |
| PDA | PerkinElmer Diode Array |
| PBM | Population Balance Model |

| | |
|---|---|
| RANS | Reynolds-Averaged Navier-Stokes |
| RNG | Renormalization Group $k$-$\varepsilon$ model |
| RH | Relative Humidity |
| RSM | Response Surface Methodology/Modelling |
| SIMPLE | Semi-Implicit Method for Pressure-Linked Equations |
| TTIP | Titanium Isopropanol |
| TOC | Total Organic Carbon |
| UHPLC | Ultrahigh Performance Liquid Chromatography |
| UV | Ultraviolet |

## Nomenclature

| | |
|---|---|
| $A_i$ | Interfacial area, m |
| $b$ | Adsorption reaction rate constant |
| $C_D$ | Drag force coefficient |
| $C_0, C$ | Initial and final concentration of organic pollutant, mol/L |
| $C_L$ | Lift force coefficient |
| $C_{TD}$ | Turbulent dispersion force coefficient |
| $C_w$ | Wall lubrication force coefficient |
| $d_b$,$d_g$ | Bubble diameter, mm |
| d.f | Degrees of freedom |
| $d_i$ | Desirability function |
| $d$ | Distance closest to the wall |
| $D_{\mathrm{lg}}$ | Fluid-particulate dispersion tensor |
| $e$ | Residual error |
| $E$ | Energy supplied by the bubbles, J |
| $E_i$ | Relative error |
| $f$ | Friction function |
| $\vec{F}_k^D$ | Drag force, N |
| $\vec{F}_k^L$ | Lift force, N |
| $\vec{F}_k^T$ | Turbulent dispersion force, N |
| $\vec{F}_k^{WL}$ | Wall lubrication force, N |
| $\vec{g}$ | Gravitational acceleration, m/s$^2$ |
| $G$ | Production of turbulent kinetic energy |
| $H$ | Static liquid height |
| $H_D$ | Displaced height during sparging, mm |
| $I$ | Irradiation intensity (W/m$^2$) |
| $k$ | Turbulent kinetic energy, J/kg |
| $K_{app}$ | Apparent reaction rate constant, min$^{-1}$ |
| $L$ | Effective length of reactor, m |
| $L_s$ | Mixing length for the subgrid scales |
| $L_{t,l}$ | Length scale, m |
| $N$ | Number of experiments |
| $n_c$ | Number of replicates at the central point |
| $\vec{n}_w$ | Unit normal pointing away from the wall |
| $\nabla p$ | Pressure gradient, Pa |
| $\mathrm{Re}_p$ | Particle Reynolds number |
| $\mathrm{Re}_\omega$ | Vorticity Reynolds number |
| $RH$ | Relative humidity (%) |
| $SS_{lof}$ | Sum of square due to lack of fit |
| $SS_{pe}$ | Sum of square due to pure error |

$SS_{reg}$ Sum of square due to regression
$SS_{res}$ Sum of square due to residuals
$SS_{tot}$ Sum of square totals
$t$ Reaction time, min
$T_{ij}$ SGS stress tensor
$\vec{u}_g$ Velocity vector of gas phase, m/s
$\vec{u}_l$ Velocity vector of liquid phase, m/s
$\vec{u}_k$ Velocity vector of phase k, m/s
$\vec{U}_{dr}$ Drift velocity
$\vec{U}_{\lg}$ Relative velocity
$V_S$ Slip velocity

*Greek letters*

$\beta_i$ Coefficients of the linear variables
$\beta_{ii}$ Coefficients of the quadratic variables
$\beta_{ij}$ Coefficients of the interaction variables
$\varepsilon$ Turbulent kinetic energy dissipation rate, $m^2/s^3$
$\kappa_s$ Surface curvature
$\mu_{BIT,l}$ Bubble induced viscosity, Pa.s
$\mu_{eff,l}$ Effective viscosity, Pa.s
$\mu_l$ Molecular viscosity, Pa.s
$\mu_{ref}$ Reference viscosity of water
$\mu_{T,l}$ Turbulent viscosity, Pa.s
$\nu$ Von Kárman constant
$\varpi_j$ Molar extinction coefficient
$\phi_{ij}$ Pressure strain term
$\rho_k$ Density of phase k, $kg/m^3$
$\sigma_i$ Interfacial tension
$\sigma_k, \sigma_\varepsilon$ Prandtl numbers
$\sigma_{\lg}$ Schmidt number
$\sigma$ Surface tension
$\tau_k$ Shear stress term, Pa
$\vartheta_{t,l}$ Characteristic time
$\vartheta_{gl}^t$ Eddy particle interaction time
$\vartheta_k$ Particulate relaxation time
$\vartheta_l^t$ Time scale

| | |
|---|---|
| $\in_g$ | Global gas hold-up |
| $\in_k$ | Volume of fraction of phase k |
| $\Phi_i$ | Quantum yield |

Subscripts

| | |
|---|---|
| *k, j* | Phase index |
| *g* | Gas |
| *l* | Liquid |
| *s* | Solid |

# CHAPTER 1

## 1. Introduction

### 1.1. General introduction

South Africa (SA), as a water stressed nation, is faced with a great challenge of addressing its water crisis (Nastar & Ramasar, 2012). Several regions of South Africa are highly dependent on summer rainfall and with the current dwindling water supplies, SA needs robust and efficient technologies to treat the current available water. One of the primary causes of human, animal and aquatic health problems is due to an increase in contaminated water caused by industries such as petroleum, pharmaceutical, beverages and mining. Petroleum refineries consist of very large and complex chemical processes that provide us with useful products that include jet fuel, petrol, kerosene, diesel and feedstock for the petrochemical industry. Wastewater from petroleum refineries often contains a high concentration of organic pollutants that are often released into the environment. These organic pollutants include aliphatic, aromatic and polyaromatic compounds. Phenol and phenolic derivatives are the mostly found organic pollutants present in petroleum wastewater. They are extremely harmful to micro-organism life, aquatic life, the environment and humans (Zulfakar et al., 2011).

The commonly applied wastewater treatment techniques such as – coagulation, bio-decomposition, chemical precipitation, adsorption and catalytic wet air oxidation (CWAO) for the removal of toxic organic compounds are quite often inadequate (Abhang et al., 2011). In addition, these processes have a disadvantage of transferring the pollutant from one phase into another, thereby producing secondary wastes (Primo et al., 2007). The application of advanced oxidation process (AOP) for the degradation of organic pollutants is efficient due to the fact that it converts the pollutants into less harmful products. Fluidized bed reactors, often used in the AOPs, consists of three phases (gas, liquid, solid) and quite often the mixing inside the reactor is a challenge. Therefore, analysis of mixing inside the reactor is often conducted by using computational fluid dynamics (CFD) as it is a low-cost reactor optimization technique.

### 1.2. Motivation

The petroleum refining industry applies a wide range of physical and chemical treatment processes based on the crude oil composition and desired products. Consequently, a portion of the wastewater from these processes, containing organic pollutants, is released into the environment. These organic pollutants are hazardous to the environment, humans and animals.

Due to the inadequacy of biological treatment and the cost of reactor optimization techniques, the advanced oxidation process has been the potential solution for degrading organic pollutants in petroleum wastewater. The performance of the AOPs depends on the determination of both optimal reactor design and operating conditions. In this context, CFD simulation and response surface modelling have shown that they are low cost optimization techniques. The heterogeneous photocatalytic oxidation (HPO) process, that is an AOP process, was used in the current study due to its ability to convert organic pollutants into less toxic substances.

## 1.3. Problem statement

Organic pollutants found in petroleum wastewater are hazardous to the environment, humans and animals. Biological processes are ineffective in degrading them due to their non-biodegradability, and the use of other processes such as chemical precipitation is costly. For this reason, AOPs such as the heterogeneous photocatalytic oxidation, have attracted a lot of interest in recent years to photodegrade organic pollutants through the application of ultraviolet (UV) light and $TiO_2$ photocatalyst. Scale-up of the HPO process, that is a challenge, is due to factors such as the cost of UV irradiation, complexity of the mixing inside the photoreactor and the separation of the photocatalyst after treatment.

A thorough study regarding the hydrodynamics (mixing and fluid dynamics) will be conducted through CFD. In addition, optimization of the CFD setting methods will be conducted to obtain the finest accuracy and convergence. Response surface modelling along with reaction kinetics will be employed to optimize the photodegradation operating parameters. Sedimentation experiments will be conducted by settling the two different photocatalysts (micro- and nano-sized) to determine the impact on efficiency when increasing the particle size.

## 1.4. Aim

The aim of this study was to apply CFD techniques and response surface modelling to optimize the hydrodynamics and operating conditions of the photodegradation of petroleum wastewater.

## 1.5. Specific objectives:

a) To simulate and photodegrade petroleum wastewater using solar irradiation.
b) To apply CFD and experimental techniques to determine the optimal hydrodynamic operating parameters in a fluidized bed reactor.
c) To determine the photodegradation reaction kinetics of the process.

d) To optimize the photodegradation operating conditions using Response Surface Methodology (RSM).

## 1.6. Thesis outline

The second chapter of the thesis provides a detailed study on the fundamental concepts and relevant laws that were used in the study. The characteristics of petroleum wastewater were dealt with, along with the different methods that are found in literature to treat petroleum wastewater. The different types of reactors used in photocatalysis were surveyed and the application of CFD to optimize fluidized bed reactors was examined. A detailed analysis of response surface modelling was provided along with a detailed explanation of statistical optimization in photocatalysis.

A detailed explanation of how the specific objectives were achieved is given in Chapter 3. A clear mathematical modelling and numerical setup of the CFD simulations is shown. The photodegradation experiments are explained in detail including the experimental setup, analysis made, experimental design and the materials used. The method for determining the reaction kinetics is also given.

Chapter 4 includes a detailed discussion and analysis of the CFD simulation, photodegradation, sedimentation and reaction kinetics results. The CFD simulations were compared to the experimental results using a numerical optimization technique. The CFD simulation data was used to characterize the hydrodynamics of an FBR by investigating parameters such as axial liquid velocity, gas hold-up, turbulent kinetic energy and turbulent dissipation rate. The photodegradation results were modelled and optimized by using the central composite design. The reaction kinetics were determined by using the Langmuir-Hinshelwood model and the sedimentation results were used to investigate the efficiency of catalyst and wastewater separation post treatment.

Chapter 5 summed up the discussion and the specific objectives of the study. The CFD simulations revealed the hydrodynamic behaviour of the FBR and was optimized by using the numerical optimization technique. The CFD study showed the significant impact the hydrodynamics have on the photodegradation experiments. The response surface modelling study provided the optimal photodegradation operating parameters along with a highly significant empirical polynomial model. Lastly, further possible studies were suggested in the

recommendations section to improve both CFD simulations and photodegradation experiments.

# CHAPTER 2

## 2. Literature review

Petroleum refinery wastewater often contains high concentrations of aromatic and aliphatic hydrocarbons. Petroleum refineries generate polluted wastewater and the process configuration often controls the characteristics and composition of the wastewater generated. These organic contaminants are significantly toxic to water sources due to their low biodegradability, stability and toxicity (Shahrezaei et al., 2012a). Conventional wastewater treatment techniques that are currently being used include: coagulation, bio-decomposition, chemical precipitation, adsorption and catalytic wet air oxidation (CWAO) (Abhang et al., 2011). Furthermore, the disadvantage with these conventional removal techniques include: restricted pH range, control of operating conditions, disposal of activated sludge and low reaction rates and efficiency (Shahrezaei et al., 2012a).

In recent years, significant research has been intensified on the treatment methods that depend on the oxidation of refractory and harmful organic pollutants and most of these methods use the advanced oxidation process (AOP). The main feature behind AOP is the generation of hydroxyl radicals ($HO^{\bullet}$) that degrade aqueous organic contaminants. Substances such as ultraviolet light, ozone and hydrogen peroxide have been researched for the generation of hydroxyl radicals (Shahrezaei et al., 2012a). The HPO process has attracted several researchers for the degradation of pollutants found in gaseous and liquid phase through the use of artificial light or solar illumination (Zulfakar et al., 2011). This process has the ability to produce less harmful and biodegradable substances.

Fluidized bed reactors employed in the HPO process are referred to as photoreactors. The preference of these reactors to researchers over conventional chemical reactors is due to their low operational temperature and high selectivity (Mohajerani et al., 2012). Despite their preference by numerous researchers, photoreactors are less preferred for industrial application due to limitations such as fouling on lamps, size limitations, construction difficulties (Mohajerani et al., 2012) and cost of UV light manufacturing and post-treatment for catalyst (Boyjoo et al., 2013). Shahrezaei et al. (2012b) reported that irradiation intensity significantly affects the photodegradation of liquid phase organic contaminants. Mohajerani et al. (2012) reported that irradiation intensity is the main factor for determining reaction kinetics and photoreactor performance. It is therefore evident that understanding the reaction kinetics is essential in evaluating the performance of the reactor. It has been reported in literature that the

reaction kinetics of the HPO process can be described by the Langmuir-Hinshelwood model (Bechambi et al., 2015). This model has the ability to determine the reaction order and reaction rate constants for both the photodegradation and adsorption mechanism.

There have been several developments in the HPO process such as synthesis of novel catalysts, optimization of operating conditions and reactor configuration. Therefore, suitable optimization and design of photoreactors is of paramount importance. It has been argued that reaction kinetics alone does not establish proper optimization of the photoreactor performance (Qi et al., 2011). Other factors such as light distribution and hydrodynamics need to be considered. Hydrodynamics inside a photoreactor has been reported to be complex and unclear due to the existence of three phases (solid, gas and liquid). CFD has attracted interest as a technique to study the hydrodynamics in fluidized bed reactors, stirred tank reactors and bubble column reactors (Qi et al., 2011). CFD models have also been used as modelling tools to optimize the hydrodynamics in a photoreactor.

## 2.1. Petroleum wastewater

### *2.1.1. Characteristics*

There are various inorganic and organic substances that can be found in crude oil and these would include water-soluble metals, salts and suspended solids. The composition of petroleum wastewater (PW) depends on the complexity of the refinery process but in general, compounds in petroleum wastewater include dissolved and suspend materials. Table 2-1 shows the characteristics of petroleum wastewater that contains a blend of hydrocarbons (phenol, benzene, polyaromatic hydrocarbons, toluene, xylenes and ethylbenzene). In addition, cations and anions, that are dissolved inorganic substances, include heavy metals.

**Table 2-1.** Characteristics of petroleum wastewater ([1] – Coelho et al., 2006; [2] – Dold, 1989, [3] - Khaing et al., 2010).

| Parameter | [1] | [2] | [3] | Average |
|---|---|---|---|---|
| BOD (mg/L) | 570 | 150 – 350 | - | 357 |
| COD (mg/L) | 850 - 1020 | 300 – 800 | 330 - 556 | 643 |
| Phenol (mg/L) | 98 -128 | 20 – 200 | - | 111 |
| Oil (mg/L) | 12.7 | 30 | 40 - 91 | 43 |
| TSS (mg/L) | - | 100 | 130 - 250 | 160 |
| Heavy metals (mg/L) | - | 0.1 – 100 | - | 50 |
| Chrome (mg/L) | - | 0.2 – 10 | - | 5.1 |
| Ammonia (mg/L) | 5.1 - 2.1 | - | 4.1 - 33.4 | 22.4 |
| pH | 8.0 - 8.2 | - | 7.5 - 10.3 | 8.5 |
| Turbidity (NTU) | 22 -52 | - | 10.5 - 159.4 | 61 |

BOD: Biological oxygen demand
COD: Chemical oxygen demand
TSS: Total suspended solids

### *2.1.2. Methods of treatment*

From literature, it was observed that studies relating to the photodegradation of organic pollutants often involve optimizing and controlling reaction conditions such as irradiation time, temperature, catalyst loading and pH level to achieve maximal degradation efficiency. Furthermore, the reactor configuration in these studies is either re-circulatory and/or batch (Boyjoo et al., 2013; Abhang et al., 2011; Lee et al., 2016; Cheng et al., 2012; Kim Phuong et al., 2016).

Shahrezaei et al. (2012b) used titanium dioxide as a photocatalyst and achieved an optimal catalyst loading of 60 mg/L and reported that temperature had an insignificant effect on the process. Abhang et al. (2011) used sodium acetate to combine the silica gel together with the $TiO_2$ catalyst particles to form a composite catalyst. The composite catalyst was used to photodegrade wastewater contaminated with phenol. The temperature in the study was not considered and operating conditions such as catalyst loading, initial concentration of phenol and aeration rate were varied for two hours. It was reported that a maximal degradation of 95.27% was obtained in 1.5 hours for a 21 L of solution and that the initial concentration of phenol and aeration significantly affected the photodegradation efficiency.

Zulfakar et al. (2011) used a fluidized bed rector to investigate the photodegradation of phenol, contrary to Abhang et al. (2011), the $TiO_2$ catalyst was immobilized on quartz sand. The

photocatalyst was synthesized by using diethanolamine, titanium isopropoxide, (TTIP), Degussa P25 $TiO_2$ powder and isopropanol. They reported that an optimal catalyst loading of 0.33 g/L was obtained using the synthesized catalyst although this was significantly higher than that found by Shahrezaei et al. (2012a) (60 mg/L). This was due to the fact that Shahrezaei et al. (2012a) used Degussa P25 titanium dioxide photocatalyst whilst Zulfakar et al. (2011) used a composite photocatalyst.

## 2.2. Photoreactors

Effective application of the fluidized bed reactor for photocatalysis requires accurate understanding of reactor efficiency among other aspects such as geometry, illumination sources, hydrodynamics and catalysts. In addition, factors such as superficial gas velocity, fluid properties and material of construction are significant parameters for evaluating the efficiency of the reactor. The reactors that are used as photoreactors for wastewater treatment are quite often operated and/or designed using the fundamentals of fluidized bed reactors. The preference of photoreactors by researchers is due to their low operating temperature, good selectivity, and the catalyst can either be immobilized on support material or suspended in solution (Mohajerani et al., 2012).

There are several types of immobilized reactors that have been effectively used in literature; such as fixed-bed, flat plate, trickle beds, falling film closed and annular venture packed bed. Whereas the suspended reactors can take numerous forms such as externally aerated rectangular tanks, annular reactors, fluidized beds and moving beds where the catalyst is suspended in the wastewater (Boyjoo et al., 2013). The immobilized reactors are cost effective in the sense that they do not require post-treatment, that is, separation for micro-sized to nano-sized catalyst recovery. However, immobilized reactors perform poorly as compared to suspended reactors. The suspended reactors have high mass transfer coefficients, good catalyst-to-pollutant contact and guarantee better catalyst particle light exposure (Boyjoo et al., 2013).

However, factors such as high productions costs, fouling on lamp walls, difficulties in construction, size limitation and design are reported to inhibit the scale-up of photoreactors (Mohajerani et al., 2012; Boyjoo et al., 2013). Consequently, the photocatalytic degradation process, when compared to traditional wastewater treatment methods, is preferred as a secondary option. Since most reactors employed for the photodegradation of industrial wastewater are suspended in nature, the design of photoreactors is based on the concept of fluidized bed reactor. The optimization of the fluidized bed reactor that consists of a three phase

contact pattern and maximizes the UV irradiation area, has been studied by several researchers (Abhang et al., 2011; Mohajerani et al., 2012; Boyjoo et al., 2013). Abhang et al. (2011) applied a three-phase fluidized bed photocatalytic reactor to maximize the UV irradiation area. In their study, they optimized design variables such as: choice of catalyst, geometry of photoreactor and usage of irradiation energy. Mohajerani et al. (2012) reported that the main characteristic in the design of a photoreactor is radiation field, due to the fact that it influences the kinetics and performance of the photoreactor. Cheng et al. (2012) designed a novel gas-liquid-solid circulating fluidized bed photocatalytic reactor (GLSCFBPR) that was employed to investigate the effects of process parameters (catalyst loading, superficial liquid and gas velocity) on the performance of the reactor. The two main concepts that were used in the design of the GLSCFPR reactor were to facilitate the mass transfer of oxygen and carbon dioxide produced and to strategically place the internal multi-layered lamps due to the fact that internal lamps provide uniform illumination better than external lamps.

## 2.3. Computational fluid dynamics

Photocatalytic bubble column reactors are often employed in industries such as petroleum, mining and wastewater treatment. The physics (momentum, mass and energy balance equations) describing the phenomena inside these reactors is extremely intricate in that modelling it is sometimes complicated and/or tedious. Therefore, to achieve correct scale-up and design procedures, fundamental phenomena such as hydrodynamics, reaction kinetics, and thermodynamics need to be accurately modelled and exposed. To date, computational, mathematical and numerical methods have been extensively used to predict the hydrodynamics inside the bubble column reactor for design, scale-up and optimization (Pourtousi et al., 2015). In the past decades, computational fluid dynamics (CFD) has enhanced our knowledge of the complex hydrodynamics that occur inside a bubble column reactor and due to high computing power and advancements in numerical techniques; CFD has been found very useful in simulating multiphase flow (Pourtousi et al., 2015). Bubble column reactors are often simulated and/or operated using multiphase (gas and liquid), where the liquid is considered as the continuous phase and gas as the dispersed phase. Therefore, inside the bubble column reactor, there is an interaction between the two phases (gas and liquid) that affects the interfacial forces, turbulence and bubble characteristics. Furthermore, correct modelling of the bubble column reactor is highly dependent on the accurate simulation of the interfacial forces, turbulence model and bubble characteristics (Pourtousi et al., 2015).

### *2.3.1. Interfacial forces*

An interaction exists between the gas and liquid that affects the interfacial forces. Several models for interfacial forces have been reported in literature (Pourtousi et al., 2015; Masood et al., 2014; Pourtousi et al., 2014) and correct modelling of the bubble column reactor is dependent on the selection of the correct interfacial force. The models for interfacial forces are used to study the interaction between the phases in multiphase modelling and this is done by solving the differential momentum equations that consist of the interfacial forces. In multiphase modelling of the Eulerian-Eulerian approach, the drag force is considered as the predominant interphase force (Pourtousi et al., 2014). Numerous studies have used only the drag force to model the hydrodynamics inside the bubble column; on the other hand, some researchers have used a combination of different interfacial forces in solving the differential momentum equations (Zhang et al., 2006; Laborde-Boutet et al., 2009; Olmos et al., 2001). It has been reported that the use of a pair and/or all the interfacial forces improves the accuracy of the flow pattern prediction (Zhang et al., 2006).

The total interfacial forces that are caused by the physical effects of two phases coming in contact can be described by the following equation:

$$\vec{F}_k = \vec{F}_k^D + \vec{F}_k^L + \vec{F}_k^{WL} + \vec{F}_k^T \tag{1}$$

where $\vec{F}_k^D$ , $\vec{F}_k^L$ , $\vec{F}_k^{WL}$ and $\vec{F}_k^T$ are the interfacial forces due to drag force, lift force, wall lubrication and turbulent dispersion, respectively. A detailed description and modelling of the interfacial forces can be found in *Section 3.1.2*.

### *2.3.2. Turbulence*

Alongside the governing equations and interfacial forces, turbulence models are a key factor in capturing the hydrodynamic behaviour inside the photocatalytic bubble column reactor (Pourtousi et al., 2014). The interaction between the gas bubbles and the surrounding fluid is a complex and fascinating phenomenon. As the bubble rises, the wake generated behind it induces turbulence normally referred to as bubble induced turbulence (BIT). The bubble induced turbulence tends to amend the turbulent characteristics of the surrounding fluid and as a result influences the hydrodynamic behaviour of the bubbles resulting in a scientific concept that, till this day, has revolutionized the field of fluid mechanics (Santarelli & Fröhlich, 2015). Furthermore, the turbulence transferred into the surrounding fluid (normally liquid) is in a form

of energy (turbulent kinetic energy) and its intensity is dependent on the regime (homogeneous or heterogeneous).

In the homogenous regime, the energy transferred is restricted due to the fact that the bubbles rising are not hindered, whereas, hindrance of the bubbles results in substantial energy being transferred (heterogeneous regime). The energy absorbed by the liquid, regardless of regime, results in turbulent motion in a form of eddies of diverse time and length scales. These flow structures have a significant impact on the transport phenomena. Therefore, understanding turbulent structures and their influence on the physics of contacting reactors is essential. In this section, various turbulent models (Direct Numerical Simulation, Large Eddy Simulation, Reynolds Stress Model and standard $k$-$\varepsilon$) are reviewed.

## (a) Direct numerical simulation (DNS)

Direct numerical simulation has the ability to reveal the full picture of practical fluid mechanical behaviour by rigorously resolving the governing equations without applying any filtering and/or smoothing method (Santarelli & Fröhlich, 2016). The use of such an approach coupled with experimental validation can provide some insight into the turbulent flow structures. Furthermore, DNS can be used to increase the understanding of multiphase models, whereby two methods have been studied in literature regarding the simulation of swarm of bubbles (Santarelli & Fröhlich, 2015). The first method, that is triply periodic domain, consisted of an unrestrained infinite domain that was used to study the characteristics of a group of bubbles. The study focused on spherical bubbles and was later expanded to deformed bubbles where factors such as velocity fluctuations and bubble-to-bubble interaction were investigated.

The second method looked at a swarm of bubbles in a channel flow, where a multiphase was restricted between two vertical walls. This method was advantageous due to the fact that it resembles several industrial contacting equipment (Santarelli & Fröhlich, 2015). Although there has been a substantial improvement in computational power, it is not sufficient to allow for full direct numerical simulations of real reactors, therefore, making DNS a costly option (Santarelli & Fröhlich, 2016). Consequently, researchers have opted for the use of a simplified turbulence model (Large eddy simulation) that requires the definition of the turbulence variables.

The algorithm that can be used for a direct numerical simulation study takes the full Navier-Stokes equation as:

$$\left[\frac{\partial u}{\partial t} + u.\nabla u\right] = -\nabla P + \mu\nabla^2 u + \rho g + F, \nabla \cdot u = 0 \tag{2}$$

This type of formulation represents that of a single phase and is applied over the entire domain. In addition, a tracking function ($c$) is included and represents the volume fraction of the continuous phase.

$$\left[\frac{\partial c}{\partial t} + u \cdot \nabla c\right] = 0 \tag{3}$$

The properties are resolved by:

$$\begin{aligned} \rho &= c\rho_G + (1-c)\rho_L \\ \mu &= c\mu_G + (1-c)\mu_L \end{aligned} \tag{4}$$

The interfacial interaction has been included in the Navier-Stokes equation as a source term using the front tracking algorithm. In addition, this algorithm (that consists of the Dirac delta function ($\delta$)) allows for the determination of bubble-to-bubble interaction along with the deformation.

$$F = \delta\sigma_i\kappa_s n \tag{5}$$

where $\sigma_i$ is the interfacial tension and $\kappa_s$ is the surface curvature.

Theoretically, it is possible to solve the whole spectrum of turbulent scales using the direct numerical simulation. Here, modelling is not required, however, it is not practicable for problems concerning high Reynolds number flows due to the fact that this model resolves large eddies directly and the small eddies are modelled (ANSYS, 2010). This creates a need for high computing power, therefore, the LES model is much more suitable due to its filtering operation.

## (b) Large eddy simulation (LES)

Eddies are used to characterize turbulent flows with a wide range of length and time scales. The characteristic length scale is comparable to the largest eddies, whereas the turbulent kinetic

energy is dispersed by the smallest scales (ANSYS, 2010). In LES, the governing equations for each phase separate the small scale motions from the large scale motions by using a filtering operation. This is done by creating two sub-grid-scale models namely Smagorinsky-Lilly model and the Dynamic Smagorinsky model (DMS) and these two have been used to simulate bubble column reactors.

From the filtered equations, the dynamics of large scale structures are computed while the small scale turbulence is modelled using the SGS model. Therefore, the resulting flow field in the LES model is decomposed into large scale or resolved components and small scale or subgrid components. Subsequent subgrid scales from the filtering operation are unknown and require modelling and this is done by employing the Boussinesq hypothesis (ANSYS, 2010).

The most frequently used SGS model is the Smagorinsky model (1963) where the turbulent viscosity is modelled by:

$$\mu_t = \rho L_s^2 \left|\bar{S}\right| \tag{6}$$

where $L_s$ is the mixing length for the subgrid scales and is expressed as:

$$L_s = \min\left(\nu d, C_s V^{1/3}\right) \tag{7}$$

where $d$ is the distance to the closest wall, $\nu$ is the von Kárman constant, $V$ is computed according to the volume of the computational cell and $C_s$ is the Smagorinsky constant. Smagorinsky (1963) derived the value for $C_s$ = 0.23 for homogeneous isotropic turbulence, however, this value was found to cause excessive damping of large scale fluctuations in the presence of mean shear and in transitional flows as near solid boundary and must be decreased in such regions. Therefore, $C_s$ is not a universal constant, although a value of 0.1 was found to produce the best results for a wide range of flows. This was also shown in Tabib et al. (2008) research.

From Equation 6, $\bar{S}$ is represented by:

$$\bar{S} = \frac{\left(S_{ij}^d S_{ji}^d\right)^{3/2}}{\left(\bar{S}_{ij}\bar{S}_{ji}\right)^{5/2} + \left(S_{ij}^d S_{ji}^d\right)^{5/4}} \tag{8}$$

and can be further expressed as:

$$S_{ij}^{d} = \frac{1}{2}\left(\bar{g}_{ij}^{2} + \bar{g}_{ji}^{2}\right) - \frac{1}{3}\delta_{ij}\bar{g}_{kk}^{2} \tag{9}$$

$$\bar{g}_{ij} = \frac{\partial \bar{u}_i}{\partial x_j} \tag{10}$$

Germano et al. (1991) developed a procedure in that the Smagorinsky model constant can be solved based on the information obtained from the resolved scales of motion. This procedure then removes the necessity of specifying the model constant, $C_s$, in advance (ANSYS, 2010). The whole notion in the dynamic procedure is to apply a second filter (named test filter) to the equations of motion. At the test filtered field level, the SGS stress tensor is expressed as:

$$T_{ij} = \overline{\rho u_i u_j} - \left(\overline{\rho u_i u_j} / \bar{\rho}\right) \tag{11}$$

Both $\tau_{ij}$ and $T_{ij}$ are computed analogous to the Smagorinsky-Lilly model, with the assumption of scale similarity;

$$\tau_{ij} = -2C\bar{\rho}\Delta^2\left|\tilde{S}\right|\left(\tilde{S}_{ij} - \frac{1}{3}\tilde{S}_{kk}\delta_{ij}\right) \tag{12}$$

$$T_{ij} = -2C\bar{\bar{\rho}}\hat{\Delta}^2\left|\hat{\tilde{S}}\right|\left(\hat{\tilde{S}}_{ij} - \frac{1}{3}\hat{\tilde{S}}_{kk}\delta_{ij}\right) \tag{13}$$

(ANSYS, 2010). In Equations 12 and 13, the coefficient $C$ is assumed to be similar and independent of the filtering process, $C = C_s^2$ (ANSYS, 2010).

When compared to the Reynolds-Averaged Navier-Stokes (RANS) models, the LES model accurately predicts the gas hold-up and liquid velocity fluctuations for complex systems that are driven by buoyancy operating at high gas fractions (Pourtousi et al., 2014). It has been found that the LES model, that separates the large scale eddies from the small scale eddies, requires a considerably finer mesh than that found in the RANS model. In addition, the LES model fails to capture the wall boundary layers due to high resolution requirements (ANSYS, 2010). As a result, the large eddies are captured as ‘relatively small’ near the wall and this causes the LES model to be suitable for low Reynolds numbers wall bounded flows.

### (c) Reynolds-Averaged Navier-Stokes (RANS)

Another method for modelling turbulent flows is the Reynolds-Averaged Navier-Stokes approach. In this approach, the instantaneous solution variables in the equations are disintegrated to produce fluctuating and mean components (ANSYS, 2010). Furthermore, these instantaneous solution variables can be in the form of species concentration, velocity vectors, energy, pressure or any scalar quantity of interest. The decomposed instantaneous solution variables are then substituted into the instantaneous momentum and continuity equations. This process is referred to as time averaging of the Navier-Stokes and it results in a decrease in the number of scales present in the flow field. This creates a mean flow due to the fact that time-averaging is larger than the largest scale (Ruiz et al., 2015). At this point, the Reynolds-Averaged Navier-Stokes has the same general form as the instantaneous Navier-Stokes equations. However, the solution variables in RANS represent time-averaged values. The RANS equations require explicit modelling and closure relations, and this is done by modelling the Reynolds stresses. Various models (Reynolds Stress Model and Standard $k$-$\varepsilon$ Model) have been proposed as closure relations and they are widely used as turbulence models by several researchers.

The Reynolds Stress model is the most intricate type of Reynolds-averaged Navier-Stokes (RANS) turbulence model, in that it abandons the isotropic eddy-viscosity hypothesis thus closing the RANS equations by resolving the transport equations for the Reynolds stresses collectively with the equation of dissipation rate (ANSYS, 2010). Several researchers have used the Reynolds stress model to solve the hydrodynamics inside the bubble column. The Reynolds stress model has the ability to predict more appropriately the effects of streamline curvature, rotation, swirl and changes in strain rate (ANSYS, 2010; Pourtousi et al., 2014). Silva et al. (2012) used the Reynolds stress model to study the flow behaviour of a bubble column operating in a heterogeneous regime. They concluded that the Reynolds stress model was suitable for the flow prediction in the distributor region. When bubble induced turbulence and anisotropy of turbulence are significant, the Reynolds stress model has the potential to show the characteristics of the bubble column (Pourtousi et al., 2014).

The Reynolds stress model consists of individual Reynolds stresses ( $\mu_i'\mu_j'$ ) that are calculated using a differential transport equation. The Reynolds stress transport equations are derived from exact momentum equations, resulting in six Reynolds stress transport equations that are

solved together with the equation for dissipation rate (Tabib et al., 2008). The generic transport equations for the transference of Reynolds stresses ( $\mu_i'\mu_j'$ ) in the liquid phase are written as:

$$\frac{\partial}{\partial t}\left(\in_L \rho_L \overline{u_i'u_j'}\right)+\frac{\partial}{\partial x_k}\left(\in_L \rho_L u_k \overline{u_i'u_j'}\right)=\in_L \rho_L p_{ij}'+\in_L \rho_L \phi_{ij}$$
$$+\frac{\partial}{\partial x_k}\left[\in_L\left(\mu_L+\frac{2}{3}C_s'\rho\frac{k^2}{\varepsilon}\right)\frac{\partial\overline{u_i'u_j'}}{\partial x_k}\right]-\frac{2}{3}\delta_{ij}\in_L \rho_L\varepsilon+S_{user} \tag{14}$$

where the left-hand side of Equation 14 represents the local time derivative and convection term. Several terms in this equation do not require any modelling, however $\phi_{ij}$ and $\varepsilon$ need to be modelled in order to close the equations (ANSYS, 2010). $p_{ij}'$ is the exact stress production term and is written as:

$$p_{ij}'=-\rho\left[\overline{u_i'u_j'}(\nabla u)^T+(\nabla u)\overline{u_i'u_j'}\right] \tag{15}$$

$\phi_{ij}$ is the pressure strain term and is given by:

$$\phi_{ij}=-C_1\frac{\varepsilon}{k_t}\left(\overline{u_i'u_j'}-\frac{2}{3}k_t\mathrm{I}\right)-C_2\left(P_{ij}-\frac{2}{3}\mathrm{tr}(P_{ij})\mathrm{I}\right) \tag{16}$$

The source term, $S_{user}$, can be defined by the user (ANSYS, 2010) and it accounts for the bubble-induced turbulence that is quite often set to zero. Therefore, to account for the turbulence caused by the bubbles, Equation 16 is added to the laminar viscosity. The Reynolds stress model is closed by solving the transport equation of the dissipation rate:

$$\frac{\partial(\in_l \rho_l\varepsilon_l)}{\partial t}+\nabla(\in_l \rho_l u_l\varepsilon_l)=\nabla\left[\in_l\left(\rho_l C_\varepsilon\frac{k_l}{\varepsilon_l}\overline{u_i'u_j'}\right)\nabla\varepsilon_l\right]+\in_l\frac{\varepsilon_l}{k_l}\left(C_{\varepsilon1}G_{k,l}-C_{\varepsilon2}\rho_l\varepsilon_l\right) \tag{17}$$

where the model constants are listed as $C_1 = 1.8$, $C_2 = 0.6$, $C_\varepsilon = 0.15$, $C_{\varepsilon1} = 1.44$ and $C_{\varepsilon2} = 1.92$ (ANSYS, 2010).

The Reynolds Stress Model is limited by its closure assumptions in the transport equations. Although the Reynolds Stress Model is considered to be superior to the two-equation models (*k*-*ε* model), it struggles particularly in modelling the dissipation-rate and pressure-strain terms

(ANSYS, 2010). This forces the model to rely on scale equations such as the *k*-*ε* model to underlie the assumptions in its transport equations.

### (d) *k*-*ε* models

The *k*-*ε* models fall under a class of models referred to as two-equation models that allow the determination of both the turbulent length scale and time scale. This is done by solving two separate transport equations (ANSYS, 2010). In the last two decades, *k*-*ε* models have been extensively used to describe the flow pattern in bubble columns and fluidized bed reactors. In addition, incorporating turbulence models with the correct interfacial force models leads to an accurate solution of the hydrodynamic parameters (Pourtousi et al., 2015). The great preference of this model by researchers is due to its simplicity, low computational requirement and being relatively inexpensive and is preferred to predict the liquid velocity and gas hold-up profiles under low superficial gas velocity (Pourtousi et al., 2015).

Pourtousi et al. (2015) reported that the standard *k*-*ε* model showed an agreement with the mean experimental data when compared to the modified *k*-*ε* models (Realizable and Renormalization Group). They added that, when considering the fluctuating liquid velocity and turbulent kinetic energy near the wall, the modified *k*-*ε* models produce more accurate solutions. The experimental equipment commonly used to measure the liquid velocity profiles, bubble size distribution, gas rise velocity, turbulence and bubble plume oscillation is the laser Doppler anemometry (LDA) and particle image velocimetry (PIV). Pfleger & Becker (2001) used standard *k*-ε model to study the hydrodynamics inside the bubble column and compared the CFD simulation data with experimental results obtained using LDA and PIV. They showed that the standard *k*-ε model could accurately predict the flow behaviour inside the bubble column; particularly the results for turbulent kinetic energy and the liquid velocity. A comparison study on the different turbulent models (LES, Reynolds stress model and *k*-*ε*) was conducted by Tabib et al. (2008) and they found that the Reynolds stress model performed well in anisotropic flows involving acceleration, buoyancy, deceleration and swirls. After understanding turbulence formulation, it is important to consider the process of discretization of the mass, momentum and turbulence equations within the computation domain.

## *2.3.3. Importance of numerical discretization scheme*

Computational fluid dynamic simulations often consist of a computational domain that has been subdivided into cells (mesh). These cells can be tetrahedron, hexahedron or quadrilateral

in shape. The differential governing equations, momentum, mass and turbulent models, are discretized (transformed) into algebraic equations and are subsequently applied over each cell, thereby allowing the scalar value at the face of each cell to be estimated (Laborde-Boutet et al., 2009). This method of discretization is initially applied to the differential governing equations and turbulent models as a step toward making them more suitable for numerical evaluation and implementation in fluid behaviour studies. With that in mind, it is therefore necessary to employ the correct discretization scheme for a particular study. The numerical schemes available in the commercial ANSYS Fluent 16.0 are First-order Upwind, Second-order upwind and Quadratic Upstream Interpolation for Convective Kinematics (QUICK), amongst others.

The First-order scheme assumes that the cell-center values of any scalar variable are denoted by the cell-average value thereby computing the values at the cell faces (ANSYS, 2010). It further assumes that the face values are equal to the cell values and employs this assumption throughout the entire cell. As a result, the First-order Upwind scheme becomes easy to converge and results in an inaccurate solution (Laborde-Boutet et al., 2009). In the Second-order Upwind scheme, the cell face values are estimated by using the multidimensional linear reconstruction method (ANSYS, 2010). In this method, higher-order accuracy is obtained by using the Green-Gaus cell based approach to compute the scalar gradient and then unite with the value from the upstream cell to determine the value at any cell face. This results in second-order accuracy (Laborde-Boutet et al., 2009). ANSYS (2010) recommends the use of Second-order Upwind scheme for hybrid or unstructured meshes.

The QUICK scheme is preferable for grids consisting of hexahedral and quadrilateral meshes due to the fact that it calculates the higher-order value of the scalar quantity at the cell face. This is done by using the weighted average of the central interpolations and second-order upwind of the variable (ANSYS, 2010). The QUICK scheme will typically result in a more accurate solution, particularly in a structured mesh. In closure, although they are easier to converge, low-order schemes result in increased numerical diffusion errors, particularly, when the flow is misaligned with the mesh. In high-order schemes, the numerical diffusion error is significantly decreased even though they are tougher to converge.

Computational Fluid Dynamics has been preferred as a modelling technique to study and optimize the hydrodynamics in a photoreactor. It has, however, several setting methods that need to be considered during simulation, and proper selection of these settings is essential to

produce accurate simulation data that best predicts experimental results. A multicriteria optimization technique is required to resolve the selection of suitable setting methods in CFD.

## 2.4. Optimization using desirability function

As in many research investigations, the effects of several process variables are evaluated against multiple response variables simultaneously minimizing the variance. Quite often, the responses are inconsistent with one another making it problematic to optimize all means and variations at the same time. An example of a process that consists of numerous independent variables and multiple responses is computational fluid dynamic studies. In a typical CFD study, in order to achieve suitable accuracy and convergence (multiple responses) one requires experience and understanding of the turbulence models and interfacial forces amongst other setting methods (independent variables). Therefore, the desirability function that uses the multicriteria methodology, is a suitable tool to solve the problem of optimization of several responses. This method is used when several response variables have to be simultaneously evaluated and optimized.

The desirability function or Derringer function is the most currently utilized multicriteria methodology in optimizing analytical procedures (Bezerra et al., 2008). The procedure for applying desirability involves: (1) defining the levels of the independent factors that concurrently produce the optimal predicted responses on the dependent variables and (2) determine the maximal overall desirability associated with the controllable variables. As a result, desirability functions are applied to determine surface responses that are both quantitative and qualitative by converting the studied responses into one measurement (Islam et al., 2009). The overall process to desirability is to first transform all the responses into discrete desirability functions ($d_i$) that vary from 0 to 1, where 0 is the lowest desirability and 1 being the highest. Numerous forms of transformations were published to obtain the individual desirability. Taking the target value ($T$) for a response ($y$) is a maximal, the individual response can be determined by:

$$d = \begin{cases} 0 \text{ if } y < 1 \\ \left( \dfrac{y - L}{T - L} \right)^s \text{ if } L \le y \le T \\ 1 \text{ if } y > T \end{cases} \tag{18}$$

where $s$ is the weight and $L$ is the lower acceptable value. The criteria for the weight are as follows: (a) the desirability function is a linear ($s = 1$), (b) the major points near the target value are weighted as important ($s > 1$) and (c) the demand is of low importance ($s < 1$). By taking the target value ($T$) for a response ($y$) is a minimum, the individual response can be determined by:

$$d = \begin{cases} 1 \text{ if } \mathrm{T} < y \\ \left(\dfrac{U-y}{U-y}\right)^{t} \text{ if } T \le y \le U \\ 0 \text{ if } y > U \end{cases} \tag{19}$$

where $t$ is the weight and $U$ is the upper acceptable value. The criteria applied for $s$ similarly applies for $t$. Taking a target that is located between the upper and lower limits, forces the desirability function to become two-sided and the function can be expressed as:

$$d = \begin{cases} 0 \text{ if } \mathrm{y} < L \\ \left(\dfrac{y-L}{T-L}\right) \text{if } L \le y \le T \\ \left(\dfrac{U-y}{U-T}\right)^{t} \text{ if } T \le y \le U \\ 0 \text{ if } y > U \end{cases} \tag{20}$$

Each calculated desirability function is then combined, by computing their geometric mean, to determine the overall desirability function ($D$).

$$D = \left(d_1 \text{ x } d_2 \text{ x } d_3 \text{ x } ..... \text{ x } d_n\right)^{1/n} = \left(\prod_{i=1}^{n} d_i\right)^{1/n} \tag{21}$$

where $n$ is the number of responses studied and $d_i$ is the desirability of the response. If any of the responses falls beyond the desirability region, the overall desirability function tends to zero. To accommodate these kinds of responses, $v_i$ is added to Equation 21 to indicate the importance of the responses:

$$D = \left( d_1^{v1} \text{ x } d_2^{v2} \text{ x .... x } d_n^{1/n} \right)^{1/n}, \qquad 0 \le v_i \le 1 (i = 1, 2, ..., n), \sum_{i=1}^{n} v_i = 1 \tag{22}$$

Prior to computing the individual respective desirability, optimization goals need to be defined for each response. In this instance, the low and high values are allocated values similar to *L* and *U* for simultaneous optimization. The meanings of the goal parameters are:

Maximal:

$d_i = 0$ if $y <$ low value.

$0 \le d_i \le 1$ as $y$ varies from low to high.

$d_i = 1$ if $y >$ high value.

Minimum:

$d_i = 1$ if $y <$ low value.

$1 \le d_i \le 0$ as $y$ varies from low to high.

$d_i = 0$ if $y >$ high value.

Target:

$d_i = 0$ if $y <$ low value.

$0 \le d_i \le 1$ as $y$ varies from low to target.

$1 \ge d_i \ge 0$ as $y$ varies from target to high.

$d_i = 0$ if $y >$ high value.

Range:

$d_i = 0$ if $y <$ low value.

$d_i = 1$ as $y$ varies from low to high.

$d_i = 0$ if $y >$ high value.

Several studies have reported the use of desirability function in various fields of science and engineering. The desirability function, when used for multiple response optimization, creates an advantage of objectivity, economy and efficiency (Bezerra et al., 2008). It is unfortunate that the desirability function is mainly used in the field of Chemistry and there is no application of desirability in literature for CFD studies. Islam et al. (2009) used the desirability function for the optimization of the adsorption process to develop an efficient method to achieve maximal removal of quinalphos (organic pesticide) from aqueous solution. They concluded that the Box-Behnken design satisfactorily modelled the effect of different adsorption parameters. Furthermore, they obtained 96.31 % removal of quinalphos using optimal adsorption condition and desirability for optimization. On the other hand, Shahrezaei et al. (2012b), used CCD to model and optimize the degradation of organic pollutants in real petroleum refinery wastewater. They obtained a desirability value of 0.979 that gave an optimal operating condition to achieve high photocatalytic degradation efficiency.

Petrović et al. (2015), conducted a study where they synthesized a composite photocatalyst of $TiO_2/WO_3$. They varied the photocatalyst preparation conditions (reaction time, current density and concentration of 12-tungstosilicic acid solution) to decolourize methyl orange. Subsequent use of Derringer's desirability function resulted in an overall desirability value of 0.82 that is relatively lower than that obtained by Islam et al. (2009) and Shahrezaei et al. (2012b) that were 0.999 and 0.979, respectively. From the studies discussed, it has been shown that the desirability function can solve the problem of multiple responses that draw opposing conclusions. It has also shown that it can be applied in a wide range of analytical procedures that consist of multiple responses, such as the system used in the present work.

## 2.5. Photocatalysis

Photocatalytic reactions are believed to be significantly affected by two factors: mass transfer and photon efficiency and the reaction mechanism is dissimilar to traditional heterogeneous catalytic reactions (Zulfakar et al., 2011). The application of fluidized bed reactors in wastewater treatment has been the subject of interest to many researchers. The modelling of fluidized bed reactors is optimized by using the desirability function. Fluidized bed reactors used in photocatalysis are referred to as photoreactors. Photocatalysis is a process that is applied within the water treatment industry for the destruction of toxic organic pollutants. The process involves using a semiconductor catalyst that is activated by UV irradiation to create chemical oxidants that are responsible for the photodegradation of toxic and recalcitrant

organic pollutants. The photocatalysis process when applied in a heterogeneous photoreactor can be classified into five stages (Mohajerani et al., 2012) and is also graphically depicted in Figure 2-1.

a. Mass transfer of phenol from the bulk fluid to the surface of the photocatalyst.
b. Adsorption (pore diffusion) of phenol from the surface of the photocatalyst to inside the pore of the photocatalyst.
c. Photocatalytic degradation reaction on the surface of the photocatalyst and formation of by-products.
d. Desorption of the by-products from the photocatalyst surface.
e. Mass transfer of the products from the interface region to the bulk fluid.

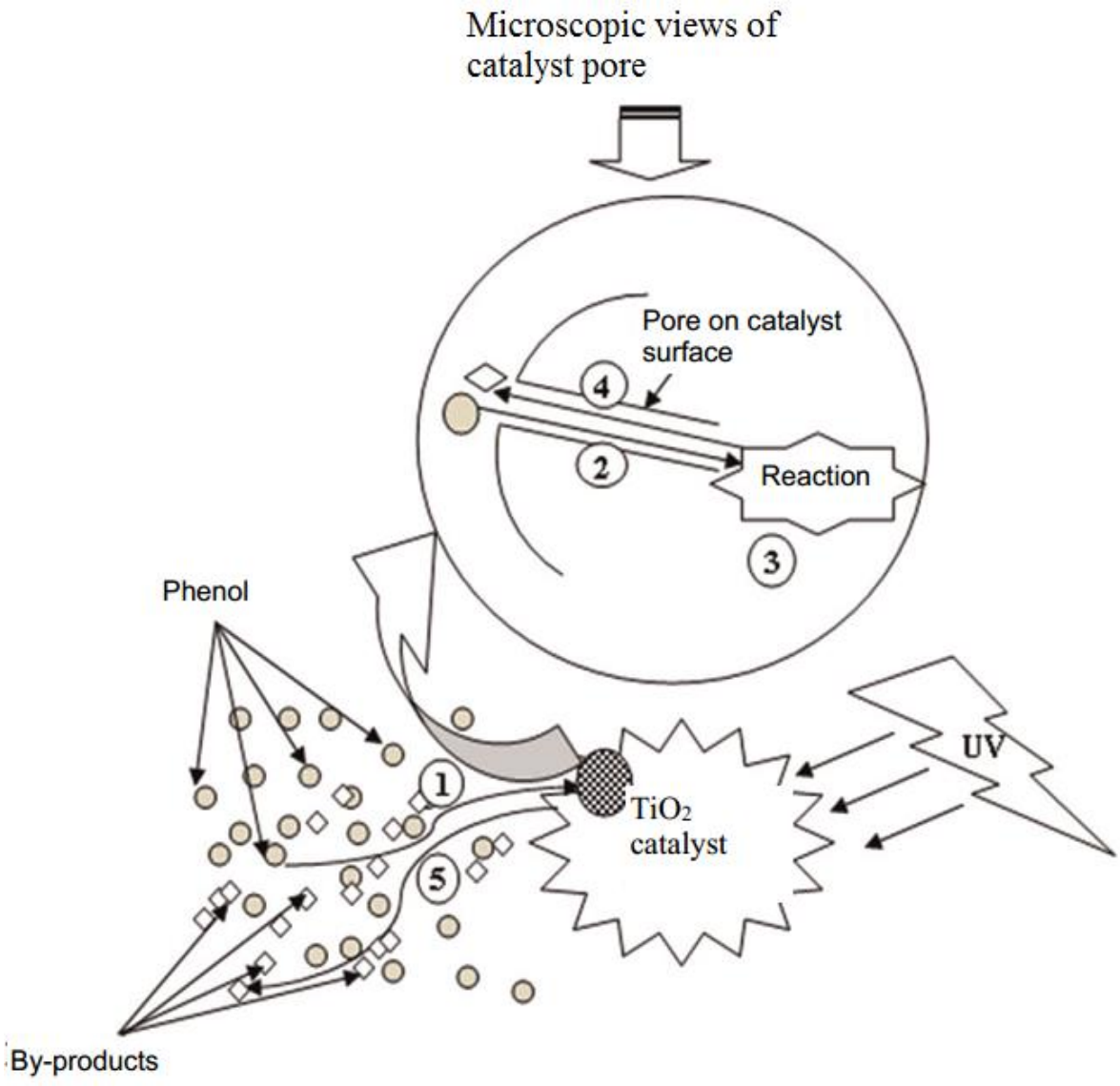


**Figure 2-1.** Schematic representation of mechanism for photocatalytic degradation of phenol (Sarkar et al., 2015).

Furthermore, the mechanism of photocatalysis can be broken down into elementary chemical reactions. The fundamentals of photocatalysis lie on the absorption of UV light by the catalyst, thereby, generating electron/hole pairs on its surface (Reaction 1). The holes generated in turn create the highly reactive hydroxyl radicals ($HO^{\bullet}$) as shown by Reaction 2:

$$TiO_2 + hv \longrightarrow h^+_{vb} + e^-_{cb} \quad \text{(R1)}$$

$$h^+_{vb} + OH^- \longrightarrow OH^{\bullet} \quad \text{(R2)}$$

The unaccompanied electron tends to recombine with the hole, resulting in a deactivated catalyst. Therefore, the presence of oxygen is essential due to the fact that it acts as an oxidant that prevents the recombination of the electron/hole pairs by reacting with the electron to form superoxide radicals as per the following reaction (Boyjoo et al., 2013):

$$e^-_{cb} + O_2 \longrightarrow O^-_2 \quad \text{(R3)}$$

The hydroxyl radicals drive the oxidation reactions that decompose the organic pollutants on the surface of the catalyst. The overall photodegradation reaction of phenol into less harmful products can be shown by:

$$\text{Phenol} + O_2 \xrightarrow{\text{Catalyst+ UV light}} CO_2 + H_2O + \text{Mineral acids} \quad \text{(R4)}$$

### *2.5.1. Photocatalyst*

Photocatalysts are robust in treating high strength effluents such as petroleum wastewater that typically contains bio-recalcitrant compounds. A typical example of a photocatalyst is the widely used nano-sized titanium dioxide ($TiO_2$) due to its affordability, resistance to various chemical compounds, insolubility in water and its non-toxicity. Haque et al. (2012) conducted a study relating to the reaction kinetics and mechanism of $TiO_2$ as a catalyst and it was reported that $TiO_2$ is stable in aqueous solutions and has the uppermost photocatalytic activity as a semiconductor. Lee et al. (2016) also stated that $TiO_2$ has the highest activity at photon energies of 300 nm < λ < 390 nm and remains steady after recurring catalytic cycles.

The four most commercially available $TiO_2$ powders are: Degussa P25, Sachtleben Hombikat UV100, Inorganic PC500 and Travancore Titanium Product. In addition, Degussa P25 is the

most preferred $TiO_2$ photocatalyst. Literature has shown that the use of Degussa P25 results in rapid photodegradation rates as compared to other $TiO_2$ powders (Colmenares et al., 2009). Khune et al. (2014) investigated the use of solar photocatalytic degradation for the treatment of phenolic wastewater under the influence of $TiO_2$ attached to silica. They showed that an increase in catalyst composite results in an increase in the photodegradation of phenol. They found that a catalyst composition of 60% $TiO_2$ was found to be optimal.

## 2.6. Reaction kinetics

The design and scale-up of small-scale processes is essential and can be achieved by correct determination of the kinetic coefficients (amongst other parameters) involved in the reaction. The reaction kinetics during the photocatalytic degradation of petroleum wastewater are complex due to the formation of intermediates and ultimate products. The photocatalytic degradation mechanism of phenol follows three main stages: (1) adsorption of phenol onto the surface of the catalyst; (2) photocatalytic degradation on the surface of the catalyst to form by-products and (3) desorption of the by-products from the catalyst surface (Sarkar et al., 2015).

Shahrezaei et al. (2012b) proposed that the second stage of the photodegradation mechanism of phenol is the rate-predominate step. Photocatalytic degradation of organic pollutants (phenol) is exemplary to the heterogeneous catalytic interaction between phenol and $TiO_2$ catalyst. This advanced oxidation reaction is carried out with the aid of hydroxyl radicals ($OH^{\bullet}$) that are created on or after the reaction between water molecules and $TiO_2$ under UV/solar irradiation (Sarkar et al., 2015). Since the oxidation reactions are greatly affected by reaction conditions (catalyst loading, pH level, etc.), it is therefore essential to understand the photodegradation reaction kinetics that in turn helps quantify the rate at that the oxidation reactions occur.

Shahrezaei et al. (2012b) reported that there are three stages in the degradation mechanism of aniline using $TiO_2$ as a photocatalyst whereby the second stage, that involves the photodegradation of aniline, is the principal step. It was also reported that the Langmuir-Hinshelwood (L-H) model (Equation 24) best described the pseudo first-order reaction kinetics. Bechambi et al. (2015) investigated the photocatalytic degradation of bisphenol A in the company of Ce-ZnO catalyst by evaluating the effectiveness of the Langmuir-Hinshelwood model. They mathematically solved or reformulated Equation 24 to produce an algebraic equation (Equation 25) that encapsulates both the photodegradation ($k_r$) and adsorption ($b$) reaction rate constants. It has been reported in literature that when the initial concentration of

pollutant is low (Bechambi et al., 2015) and/or adsorption is relatively weak (Kim Phuong et al., 2016), the denominator of the term on the right in Equation 24 becomes insignificant and hence it can be neglected. Therefore, Equation 24 can be transformed into a linearized algebraic model (Equation 26).

$$-\frac{dC}{dt} = k_r \frac{bC}{1+bC} \tag{24}$$

$$t = \left(\frac{1}{k_r b}\right)\ln\left(\frac{C_0}{C}\right) + \frac{C_0 - C}{k_r} \tag{25}$$

$$\ln\left(\frac{C_0}{C}\right) = (k_r b)t = K_{app}t \tag{26}$$

where $k_r$ is a degradation reaction rate constant that may rely on humidity, temperature and incident light and $b$ is the adsorption reaction rate constant that depends on the chemical affinity of the pollutant with the catalyst, $C_0$ and $C$ are the initial and final concentration of organic pollutant and $K_{app}$ is the apparent rate constant used as a simple kinetic variable for different photocatalysts (Bechambi et al., 2015).

Wang et al. (2012) used the L-H model to investigate the photocatalytic process for the odour abatement process to photodegrade organic gaseous substances. In addition, they stretched the L-H model by incorporating the irradiation intensity ($I$) (Equation 27). This was also evident in the work done by Sanongraj et al. (2007) where the photocatalytic destruction of organic contaminants in air was modelled using the modified L-H model (Equation 28).

$$-\frac{dC}{dt} = I^{\alpha}\frac{k_r bC}{1+bC} \tag{27}$$

where $I$ is the irradiation intensity.

$$-\frac{dC}{dt} = \frac{bC}{1+bC}\frac{kI}{A+I}\left(K_3 + K_4[C_o] + K_6[C_o]^2\right)\left(K_5 + K_2 RH\right) \tag{28}$$

where $A$ is the constant for influence of UV light intensity, $RH$ is the percentage relative humidity, $C_o$ is the initial concentration of organic pollutant, $K_2$, $K_3$, $K_4$, $K_5$, and $K_6$, are the fitting constants.

Primo et al. (2007) developed a mathematical model that was used to evaluate the kinetics of process toxicity for phenol photooxidation. They developed a generalized kinetic model by using the combination of Stark-Einstein law and Lambert-Beer law as shown by:

$$-\frac{dC_i}{dt} = I_0 \Phi_i f_i \left[ 1 - \exp\left( -2.3L \sum_{j=1}^{N} \varpi_j C_j \right) \right] \tag{29}$$

where $\varpi_j$ is the molar extinction coefficient, $L$ is the effective length of the reactor, $f_i$ is the ratio of light absorbed by $i$ to the sum of all the components in solution that absorbed the light, $I_0$ is the incident flux of radiation and $\Phi_i$ is the quantum yield.

Furthermore, it was stated that when the UV radiation is absorbed by substrate $i$ ($f_i = 1$) and the optical density is less than 1, then Equation 29 can be simplified into a first-order expression (Equation 30) that is often used to determine the quantum yield. They motivated that the use of this generalized kinetic model is due to the fact that it considers both direct photolysis by UV and degradation by hydroxyl radicals that are formed by the photolysis of hydrogen peroxide.

$$-\frac{dC_i}{dt} = 2.3 I_0 L \Phi_i \varepsilon_j C_j \tag{30}$$

In comparing the work done by Wang et al. (2012) and Sanongraj et al. (2007), the reaction kinetics of the photocatalytic degradation of gaseous contaminants is largely influenced by the irradiation intensity, in addition, Sanongraj et al. (2007) reported that the photodegradation of toluene was also affected by a relative humidity greater than 14 %. Shahrezaei et al. (2012b) showed that irradiation intensity significantly affects the photodegradation of liquid phase organic contaminants. The generalized kinetic model that was developed by Primo et al. (2007) is limited in a sense that it merely considers the photodegradation reaction kinetics that are due to direct photolysis (UV) and degradation by $HO^{\bullet}$ and disregards the adsorption kinetics.

## 2.7. Statistics and optimization

Researchers are constantly conducting experiments to evaluate conflicting theories. Within the process of resolving conflicting theories, the performance of a system needs to be improved to achieve maximal profit and this is done through optimization. From a research point of view, optimization has been frequently used as a tool for identifying experimental conditions, that

when combined together, produce the best possible response (Bezerra et al., 2008). In the past years, a systematic procedure to design experiments has been defined and researchers understand the wide variety of statistical methods to conduct experiments successfully. Other researchers find the approach very empirical in a sense that they occasionally use the Simplex method for optimization whilst others still find the need to use multivariate analysis (Araujo & Brereton, 1996). The conventional optimization technique commonly used by researchers is by monitoring the influence of one-factor-at-a-time on the experimental response. This is done by changing one parameter whilst keeping other parameters constant. The main drawback regarding this optimization technique is that it is non-feasible and does not include the interactive effects between the parameters (Islam et al., 2009).

In addition, one-factor optimization increases the number of experiments to be conducted, thus resulting in an increase in the operational cost and time. This optimization disadvantage needs to be resolved due to a demand by industrial applications for comprehensive optimization techniques (Petrović et al., 2015). For this reason, multivariate statistical techniques have been used as a statistical optimization tool. In the past years, factorial or fractional factorial designs, have been preferred over one-factor design due to its scientific approach to evaluate how inputs disturb the response. The response surface methodology (RSM) is the most frequently used statistical optimization tool (Petrović et al., 2015).

Response surface methodology involves the grouping of mathematical and statistical techniques to create an empirical model that is usually in the form of a polynomial equation (Bezerra et al., 2008). The empirical model is then applied on experimental data to describe the behaviour of the data set and to simultaneously optimize the levels of the parameters to obtain the best process performance. Before applying RSM modelling, it is essential to select an experimental design that will define how the parameters will be studied and to understand whether the experimental design will yield first-order, second-order or higher-order models. For linear functions, experimental designs such as one-variable-at-a-time, factorial designs should be used whilst for quadratic response surfaces, central composite, Box-Behnken and Doehlert designs should be used (Bezerra et al., 2008). The steps that are used when employing RSM as an optimization technique are:

a) Choosing the independent variables that have the main effect on the system;
b) The selection of the appropriate experimental design and performing the experiments according to the experimental matrix;

c) The mathematical-statistical analysis of the data by fitting the polynomial functions;
d) The evaluation of the model fitness and
e) Optimization of the studied variables.

### *2.7.1. Screening of variables*

Most experiments consist of numerous variables that may affect the response of a system. As a result, identifying and controlling all the variables that pose minor or major effects to the response variable is practically impossible. It is therefore advisable to select variables with major effects by conducting screening designs (Bezerra et al., 2008). Araujo & Brereton (1996) studied screening approaches to enable researchers to identify factors that are significant and to fine-tune the optimization process by using three to four significant factors. Callao (2014) stated that full factorial and reduced factorial designs can be used as screening approaches due to their efficiency.

### *2.7.2. Selection of experimental design*

The response variable to experimental data can be approximated by linear or quadratic (three-level factorials, Doehlert, central composite and box-Behnken) functions and this was introduced by Box & Wilson (1951). In the past 50 years, concepts such as rotatability and bias criterion have been applied in the statistical approach of experiments for experimental design purposes (Hill & Hunter, 1966). It should be noted that, in this context, the experimental data that can be modelled using first-order equations are referred to as first-order designs, whereas, experimental data that can be modelled using second-order or quadratic polynomials are referred to as second-order or quadratic designs.

A model that can be simply applied under RSM is the linear function. For suitable application of the linear function, the response variable must fit well in the following equation:

$$y = \beta_0 \sum_{i=1}^{k} \beta_i x_i + e \tag{31}$$

where $\beta_0$ is the constant term, $k$ is the number of variables, $x_i$ symbolises the variables, $e$ is the residual error observed in the response and $\beta_i$ signifies the coefficients of the linear variables.

A response surface that graphically produces a linear curve can be modelled using a low-order polynomial. However, a response surface that graphically produces curvature must be evaluated using second-order model. Two-level factorial designs are used to evaluate linearity,

however, the drawback is that they disregard responses where curvature is significant (Bezerra et al., 2008). This drawback can be resolved by adding a central point in the two-level factorial design and this improves the modelling of curvature. Therefore, second-order polynomial models can model curvature and evaluate the interaction between the different experimental factors. In addition, the second-order interaction model is extended to include the following terms:

$$y = \beta_0 + \sum_{i=1}^{k} \beta_i x_i + \sum_{1 \le i \le j}^{k} \beta_{ij} x_i x_j + e \tag{32}$$

where $\beta_{ij}$ signifies the coefficients of the interaction parameters and $x_i x_j$ represents the interaction between the different variables.

As opposed to the two-level factorial design, a three-level factorial design has to be carried out to compute the variables in Equation 31 resulting in two modelling and symmetrical response surface designs. Curvature producing experimental designs often consists of critical points, namely: minimum, maximal and/or saddle. Consequently, these critical points can be mathematically captured by extending Equation 32 to include quadratic terms:

$$y = \beta_0 + \sum_{i=1}^{k} \beta_i x_i + \sum_{i=1}^{k} \beta_{ii} x_i^{\,2} + \sum_{1 \le i \le j}^{k} \beta_{ij} x_i x_j + e \tag{33}$$

where $\beta_{ii}$ signifies the coefficients of the quadratic parameters. As mentioned earlier, the most commonly encountered second-order symmetrical designs are the three-level, Doehlert, central composite and Box-Behken design. These second-order designs vary from each other with respect to their number of levels, number of runs and selection of experimental points. The central composite design is the second-order design that was used in the current study and is further discussed in the subsequent section

### *2.7.3. Variable codification*

Second-order experimental designs are necessary to define the number of variables studied (major effects) and at what level each variable is set at. This is done by establishing a region so that each variable will be studied and this is referred to as the experimental region or domain (Hill & Hunter, 1966). It is therefore not guaranteed that the experimental results will be valid outside this experimental domain. The next step is to transform the studied real values into coded dimensionless quantities that must be proportional at its localization in the experimental

domain. This is referred to as codification of the levels of the variables studied and it enables the variables to be investigated at various orders of magnitude without influencing the evaluation of the lesser (Bezerra et al., 2008). The coded values are indicated by –α, -1 and 0 that are branded as low axial point, low factorial point and central point, respectively. In addition, the positive (+) symbols would refer to the respective high coded values. The real studied values are coded using the following equation:

$$x_i = \left( \frac{z_i - z_i^0}{\Delta z_i} \right) \tag{34}$$

where $x_i$ is the coded level, $\Delta z_i$ is the distance between the real value at the central point and the real value in the low or high level of a variable (step change), $z_i$ is the real value and $z_i^0$ is the real value in the central point.

### *2.7.4. Central composite design (CCD)*

The central composite design is the most popular class of designs used for fitting second-order models. It was introduced by Box & Wilson, (1951) and generally consists of a full factorial or fractional factorial design, central runs and additional points (star runs) that are at a distance α from the centre. Figure 2-2 shows the full CCD for the optimization of $k = 2$ and $k = 3$ factors. The second-order design that is being modelled by CCD should provide good predictions throughout the region of interest. Box & Wilson, (1951) proposed that the design should be rotatable, meaning that the variance of the predicted response should be the same in all direction from the central point. The RSM is an optimization technique and the location of optimal is unknown prior to running the experiment. Therefore, it is advantageous to use a design that will provide equal precision of estimation in all directions. The correct practical employment of the CCD is through sequential experiments, that is, a factorial design that was used to fit a first-order model and exhibits lack of fit. Therefore, axial runs are added to the experimental design resulting in quadratic terms being amalgamated into the model (Montgomery, 2012). The number of experiments ($N$) to be conducted is computed by the following equation:

$$N = k^2 + 2k + n_c \tag{35}$$

where $k$ is the number of factors (major effects) and $n_c$ is the number of replicates for the central point.

Central composite design is very appropriate for second-order modelling and requires two parameters to be defined: the number of central points and the distance of the axial runs (α) from the respective central points. The rotatability in CCD is caused by the choice of α (Montgomery, 2012). The distance of the axial runs depends on the number of factors used and is determined by $\alpha = 2^{(k-p)/4}$. Therefore, for two, three and four factors; the axial points will be 1.41, 1.68 and 2.00, respectively (Bezerra et al., 2008). A fully routable CCD is often studied in five levels: -α, -1, 0, +1 and +α.

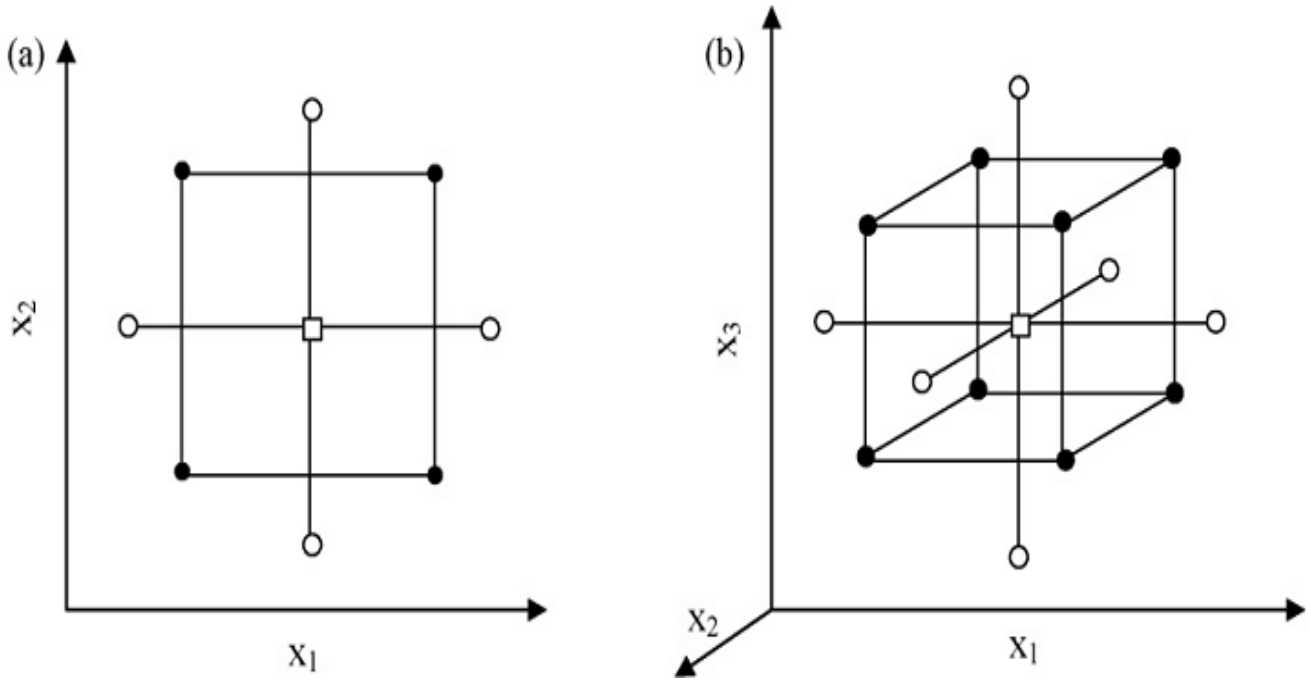


**Figure 2-2.** Representation of central composite design showing two-variable and three-variable optimization. (a) two-variables (α = 1.41) and (b) three-variables (α = 1.68). (□) central point, (○) axial points and (●) factorial design points (Bezerra et al., 2008).

### *2.7.5. Model fitting and verification*

Evaluating the combined effects of the experimental factors on the response variable is essential in experimental analysis. The predicted values need to exhibit negligible deviation from the actual values and they are obtained from the model fitting technique using Design Expert® Software of Stat-Ease Inc. In some cases, the fitted model does not reasonably describe the actual data within the experimental domain studied such that the model exhibits a significant deviation. A reliable way to evaluate the value of the fitted model is through the application of analysis of variance (ANOVA). The whole purpose of ANOVA is to associate the variance that is caused by changing the combination of the variable levels with the variation

due to random errors intrinsic to the measurement of the response surface (Bezerra et al., 2008). Furthermore, it is then possible to evaluate how significant the regression used is to the predicted responses considering experimental variance. The variation of the predicted values studied by evaluating its dispersion through the following equation:

$$d_i^2 = \left(y_{ij} - \bar{y}\right)^2 \tag{36}$$

where $d_i$ is the squared deviation, $y_{ij}$ is the replicate of the predicted value ($y_i$) and $\bar{y}$ is the observed value. The sum of the squared deviation for all observations relative to the media is referred to as the total sum of the square ($SS_{tot}$) that, alternatively, can be written as:

$$SS_{tot} = SS_{reg} + SS_{res} \tag{37}$$

where $SS_{reg}$ is the sum of the square due to regression (fitted mathematical model) and $SS_{res}$ is the sum of the square due to the residuals produced by the model. As aforementioned, CCD consists of replicates of the central point ($n_c$); this assists in determining the pure error associated with repetitions. Therefore, the sum of the squares due to residuals can be defined as:

$$SS_{res} = SS_{pe} + SS_{lof} \tag{38}$$

where $SS_{lof}$ is the sum due to lack of fit and $SS_{pe}$ is the sum of the square due to pure error. Media of the square (MS) is obtained by dividing the sum of the square (SS) of each source variation (lack of fit, total, pure error, residual and regression) by its respective numbers of degrees of freedom (d.f.). Determination of the degrees of freedom for each sum of the square variation is show in Table 2-2. The effect caused by the regression can be evaluated by the ratio of media of square of regression ($MS_{reg}$) to the media of square of the residuals ($MS_{res}$). The comparison of these variation sources is done by using the Fisher distribution ($F$ test), considering the respective degrees of freedom associated with regression and variance (Bezerra et al., 2008). A significant value for this ratio should be greater than the tabularized value for $F$. This shows that the polynomial model fits well to the experimental data.

**Table 2-2.** Analysis of variance of the fitted polynomial model to experimental data using multiple regression (Bezerra et al., 2008).

| Variation source | Sum of the square | Degree of freedom | Media of the square |
|---|---|---|---|
| Regression | $SS_{reg} = \sum_i^m \sum_j^{n_1} (\hat{y}_i - \bar{y})^2$ | $p-1$ | $MS_{reg} = \frac{SS_{reg}}{p-1}$ |
| Residuals | $SS_{res} = \sum_i^m \sum_j^{n_1} (y_{ij} - \hat{y}_i)^2$ | $n-p$ | $MS_{reg} = \frac{SS_{res}}{n-p}$ |
| Lack of fit | $SS_{lof} = \sum_i^m \sum_j^{n_1} (\hat{y}_i - \bar{y}_i)^2$ | $m-p$ | $MS_{lof} = \frac{SQ_{lof}}{m-p}$ |
| Pure error | $SS_{pe} = \sum_i^m \sum_j^{n_i} (y_{ij} - \bar{y}_i)^2$ | $n-m$ | $MS_{pe} = \frac{SS_{pe}}{n-m}$ |
| Total | $SS_{tot} = \sum_i^m \sum_j^{n_i} (y_{ij} - \bar{y})^2$ | $n-1$ | |

($p$) is the number of parameter of the model, ($m$) is the total number of levels in the design and ($n$) is the number of observations.

In summary, contamination of water sources by industrial processes has been a serious threat to human, animal and aquatic life. Advancement in wastewater treatment technologies, such as Heterogeneous Photocatalytic Oxidation (HPO), has shown great potential in the removal of toxic organic pollutants. An essential feature in the HPO process is the utilization of a fluidized bed reactor to aid uniform mixing of the different phases and provide good catalyst-to-light exposure. Computational fluid dynamics is a useful technique to offer insight regarding the mixing inside the fluidized bed reactor. It captures the hydrodynamic behaviour such as: gas hold-up, velocity vectors, bubble size distribution and turbulence structures. Moreover, the photodegradation operating variables and their subsequent optimization are equally important. The optimization is done using response surface modelling. The hydrodynamic behaviour can be married with the photodegradation data to obtain a complete picture on the performance of the HPO process.

# CHAPTER 3

## 3. Methodology

Petroleum wastewater is the industrial wastewater of interest that was photodegraded using the HPO process in a fluidized bed photoreactor. This is the process that was focused on due to its ability to degrade persistent organic pollutants and produce more biologically degradable and less toxic substances. This process is highly dependent on the generation of hydroxyl radicals and these radicals can transform several toxic organic pollutants, including non-biodegradable ones, into less harmful products such as carbon dioxide and water. The HPO process is highly influenced by operating conditions such as: reaction time, pH level, superficial gas velocity and catalyst loading. Therefore, these conditions were studied experimentally and optimized by using the central composite design.

The HPO process follows a three stage degradation mechanism where the dominant stage is the photocatalytic degradation of organic pollutants on the surface of the catalyst (Shahrezaei et al., 2012b). Therefore, understanding the photodegradation reaction kinetics is essential to understand the reaction mechanism. The photodegradation kinetics were determined using the L-H model due to its ability to account for both the adsorption ($b$) and photodegradation ($k_r$) kinetics. The modified L-H models developed by Sanongraj et al. (2007) and Wang et al. (2012) were not considered in the current study due to their inapplicability in liquid photodegradation.

A fluidized bed photoreactor was used to photodegrade the petroleum wastewater due to its ability to operate at low temperatures and its high selectivity. The fluidized bed reactor was operated in suspended mode as it provides good catalyst-to-pollutant contact, high mass transfer coefficient and better catalyst particle light exposure (Boyjoo et al., 2013). However, the hydrodynamics inside this reactor are complex due to the presence of three phases. Therefore, CFD was used as a modelling tool to determine the flow behaviour and optimize the hydrodynamics inside the reactor. This was done by varying the CFD settings (time step size, discretization scheme and grid size) that had a significant influence on the simulation accuracy and convergence. The varying of the CFD settings was done by using a 3-level factorial design which enables the study of the interdependency of the CFD settings and the simulation data was compare to Kulkarni et al., 2007.

## 3.1. Mathematical modelling

### *3.1.1. Governing equations*

Three-dimensional (3D) transient CFD models were used to solve the local hydrodynamics inside the photocatalytic bubble column reactor. The Eulerian-Eulerian approach was used to describe the flow characteristics of each phase. In this approach, liquid is considered to be the continuous phase, whereas gas is dispersed. This means that both phases (liquid and gas) are treated as interpenetrating continua (Qi et al., 2011). Furthermore, this approach permits the modelling of multiple separate, yet interacting phases for which equations such as mass and momentum are solved for each phase (ANSYS, 2010; Boyjoo et al., 2014). The governing differential continuity equation, neglecting the interphase mass transfer, for each phase in the photocatalytic bubble column reactor is given as:

$$\frac{\partial}{\partial t}\left(\in_k \ \rho_k\right)+\nabla\left(\in_k \ \rho_k \vec{u}_k\right)=0 \tag{39}$$

where $\in_k$, $\rho_k$ and $\vec{u}_k$ are the volume fraction, density and velocity vector of phase k, respectively. The subscript *k* represents liquid, gas or solid phase. The momentum equation is given as:

$$\frac{\partial}{\partial t}\left(\in_k \ \rho_k \vec{u}_k\right)+\nabla\left(\in_k \ \rho_k \vec{u}_k \vec{u}_k\right)=-\in_k \nabla P-\nabla\left(\in_k \ \tau_k\right)+\in_k \ \rho_k \vec{g}+\vec{F}_k \tag{40}$$

where $\vec{g}$ and *p* are the gravitational acceleration and pressure gradient, respectively. $\vec{F}_k$ represents the interfacial forces exerted on phase *k* due to the presence of phase *j*. $\tau_k$ is the stress term of gas bubbles and is given by:

$$\tau_k=-\mu_{eff,k}\left[\left(\nabla\vec{u}_k\right)+\left(\nabla\vec{u}_k\right)^T-\frac{2}{3}I\left(\nabla\vec{u}_k\right)\right] \tag{41}$$

where $\mu_{eff,k}$ is the effective viscosity of the liquid that in turn consists of three terms namely: molecular viscosity, turbulent viscosity and bubble induced turbulence.

$$\mu_{eff,l}=\mu_l+\mu_{T,l}+\mu_{BIT,l} \tag{42}$$

In addition, the gas phase effective viscosity is given as:

$$\mu_{eff,G} = \mu_{eff,l} \frac{\rho_G}{\rho_L} \tag{43}$$

### *3.1.2. Interfacial forces*

In the current study, a combination of all the interfacial forces (Equation 1) was used as recommended by literature. The source of the drag force is caused by the resistance experienced by the bubbles as they move through the liquid. The pressure distribution that surrounds the bubble creates form drag and the viscous stress creates skin drag (Tabib et al., 2008). The interphase momentum transfer due to the drag force is given as:

$$\vec{F}_{\lg}^{D} = \frac{3}{4} \frac{C_{D,\lg}}{d_g} \rho_l \in_g \left|\vec{u}_g - \vec{u}_l\right| \left(\vec{u}_g - \vec{u}_l\right) \tag{44}$$

where $C_D$ is the drag coefficient and $d_g$ is the bubble diameter. The superficial gas velocity in this study was varied between 5.77 and 23.1 mm/s, signifying a homogeneous flow regime. In this regime, the bubbles are assumed to be spherical, have similar sizes, shapes and velocities and the bubble break up, collision and coalescence are negligible (Pourtousi et al., 2015). Therefore the Grace et al. (1978) relation was chosen to compute the drag coefficient and is given by:

$$C_D = \frac{4}{3} \frac{g d_b}{u_T^2} \frac{\Delta\rho}{\rho_l} \tag{45}$$

where $d_b$ is the mean bubble diameter, $\Delta\rho$ is the density difference between the liquid and gas phases and $u_T$ is the terminal rise velocity of the bubble and is explained in Appendix F (List of equations).

The lift force acts on the particles of the secondary phase (bubbles) and is mainly due to the velocity gradients in the primary phase. Therefore, the lift force becomes more significant for larger bubble sizes. This force is created by the net effect of pressure and stress exerted on the surface of the secondary phase. The lift force acting on the primary (*l*) and secondary (*g*) phases can be calculated as:

$$\vec{F}_{\mathrm{lg}} = -C_L \rho_l \in_g \left(\vec{u}_g - \vec{u}_l\right) \mathrm{x} \left(\nabla \mathrm{x}\, \vec{u}_l\right) \tag{46}$$

The sign convention of this force depends on the orientation of the slip velocity with respect to the gravity vector. $C_L$ is the lift coefficient and was computed using the Saffman-Mei lift model (ANSYS, 2010):

$$C_L = \frac{3}{2\pi\sqrt{\mathrm{Re}_\omega}} C'_L \tag{47}$$

where $C'_L$ = 6.46 and $0 \leq \mathrm{Re}_p \leq \mathrm{Re}_\omega \leq 1$. Here, $\mathrm{Re}_p$ is the particle Reynolds number and is the voracity Reynolds number. Extention of the Saffman-Mei lift model is shown in Appendix F (List of equations).

The wall lubrication force can be used to model bubbly flows (liquid-gas) using the Eulerian approach. The wall lubrication force drives the secondary phase away from the wall resulting in the secondary phase concentrating in the area near but not immediately next to the wall. The wall lubrication force exerted on the secondary phase is given by (ANSYS, 2010):

$$\vec{F}_{w,l} = C_{w.} \rho_l \in_g \left|\left(\vec{u}_l - \vec{u}_g\right)\right|^2 \vec{n}_w \tag{48}$$

where $\vec{n}_w$ is the unit normal pointing away from the wall; $C_w$ is the wall lubrication coefficient and is computed using the Antal et al. (1991) model:

$$C_w = \max\left(0, \frac{C_{w1}}{d_b} + \frac{C_{w2}}{y_w}\right) \tag{49}$$

where $C_{w1}$ and $C_{w2}$ are the non-dimensional coefficients and for the current study were specified to be -0.0064 and 0.016 (Krepper et al., 2005), respectively.

The effect of turbulent fluctuations on the liquid velocity, caused by the turbulent eddies in the continuous phase, interact with the bubbles by transporting them from a region of high concentration to a region of low concentration (ANSYS, 2010). This phenomenon is described by the turbulent dispersion force that encapsulates the interphase turbulent momentum transfer and acts as a turbulent diffuser for the dispersed flow. The turbulent dispersion force, that was modelled using the Burns et al. (2004) model in the current study, can be derived from the Favre averaging of the drag term:

$$\vec{F}_{TD,l} = -\vec{F}_{TD,g} = C_{TD} K_{\lg} \frac{D_l}{\sigma_{\lg}} \left( \frac{\nabla \in_g}{\in_g} - \frac{\nabla \in_l}{\in_l} \right) \tag{50}$$

where $C_{TD}$ is the turbulent dispersion coefficient and was assigned a value of 0.2 for the current study and $\sigma_{\lg}$ is the Schmidt number and a value of 0.9 is typically used (ANSYS, 2010).

### *3.1.3. Turbulence modelling*

Modelling turbulence in a multiphase fluid flow problem is an extremely complex task due to the increase in the number of terms that require closure in the momentum equations. Closure models are essential in turbulence modeling due to the fact that they assist in unfolding the effects of turbulent variations of velocities and scalar variables (ANSYS, 2010). The standard *k*-*ε* model was used in the current study to capture the turbulent characteristics in the liquid phase. The choice of using the standard *k*-*ε* model is due to its simplicity, low computational requirements and being relatively inexpensive and is preferred to predict the liquid velocity and gas hold-up profiles under low superficial gas velocity (Pourtousi et al., 2015). Furthermore, it has been shown that it gives a fair prediction of the flow field. When the standard *k*-ε model is applied, the turbulent eddy viscosity model is used to determine the averaged fluctuating turbulent characteristics (length scale and characteristic time). The turbulent eddies can be defined in terms of the characteristic time as:

$$\vartheta_{t,l} = \frac{3}{2} C_\mu \frac{k}{\varepsilon} \tag{51}$$

where $\vartheta_{t,l}$ is the characteristic time. In addition, the energetic turbulent eddies can be described by the length scale ($L_{t,l}$) as (ANSYS, 2010):

$$L_{t,l} = \sqrt{\frac{3}{2}} C_\mu \frac{k^{3/2}}{\varepsilon} \tag{52}$$

The turbulent eddy viscosity ($\mu_{T,l}$) can be shown by the following equation:

$$\mu_{T,l} = \rho_l C_\mu \frac{k^2}{\varepsilon} \tag{53}$$

where $k$ and $\varepsilon$ are the turbulent kinetic energy and turbulent kinetic energy dissipation rate, respectively, and are calculated from their governing equations:

$$\frac{\partial}{\partial t}\left(\rho_l \in_l k\right)+\nabla\left(\rho_l \in_l u_l k\right)=-\nabla\left(\in_l \frac{\mu_{eff,l}}{\sigma_k}\nabla k\right)+\in_l \left(G-\rho_l \varepsilon\right) \tag{54}$$

$$\frac{\partial}{\partial t}\left(\rho_l \in_l \varepsilon\right)+\nabla\left(\rho_l \in_l u_l \varepsilon\right)=-\nabla\left(\in_l \frac{\mu_{eff,l}}{\sigma_\varepsilon}\nabla \varepsilon\right)+\in_l \frac{\varepsilon}{k}\left(C_{\varepsilon 1}G-C_{\varepsilon 2}\rho_l \varepsilon\right) \tag{55}$$

where $\sigma_k = 1$ and $\sigma_\varepsilon = 1$ are the Prandtl numbers. The standard values of all the model constants are $C_\mu = 0.09$, $C_{\varepsilon 1} = 1.44$ and $C_{\varepsilon 2} = 1.92$. The term $G$ in Equations 70 and 71 is the production of turbulent kinetic energy and is formulated by:

$$G = \tau_L : \nabla u_L \tag{56}$$

The hydrodynamic characteristics that were predicted by the CFD simulations need to satisfy the energy balance. It has been shown in literature that the energy, E, that is supplied by the bubbles to the liquid is described by (Kulkarni et al., 2007; Tabib et al., 2008):

$$E = \frac{\pi}{4}D^2\left(\rho_l - \rho_g\right)gH \in_l \left[V_l + \left(C_B - 1\right)\in_g V_S\right] \tag{57}$$

where $V_S$ is the slip velocity, $\in_l$ is the liquid volume fraction and $C_B$ represents the influence of the bubble induced turbulence that is transported into the liquid phase.

## 3.2. Numerical techniques

Computational fluid dynamics (CFD) makes a substantial contribution in the modelling of chemical industrial equipment due to its ability to model complex hydrodynamic phenomena efficiently. The shortfalls regarding the application of CFD are the endless parameters that need to be adjusted to achieve accuracy and convergence at minimal expense. Previous simulations have shown that the most influential parameters that affect accuracy and convergence in transient simulations are: grid size, discretization scheme and time step size. Furthermore, 18 simulations were carried out by varying the aforementioned parameters and comparing to experimental results from Kulkarni et al. (2007) as a reference case.

In the current study, a set of governing equations, explained in the Mathematical Modelling section, were solved numerically by following these stages: (i) generation of the appropriate grid domain; (ii) transformation of the governing equations into algebraic equations; (iii) selecting the discretization schemes; (iv) formulation of the discretized equation at every grid location; (v) formulation of the pressure equation and (vi) the development of a suitable iteration scheme to obtain a final solution. These solution steps were carried out using ANSYS Fluent 16.0 software and the equations of motion and continuity were solved, coupled with *k*-ε equations, to obtain complete a flow pattern by scrutinizing the gas holdup, liquid velocity and turbulence modelling profiles.

### *3.2.1. Geometry*

The geometry studied is similar to that discussed in *Section 3.5*. It consists of a cylindrical shaped body comprising of 4 side ports and a conical shaped top section suited for degassing. The cylindrical shaped section contains an inside diameter of 40.8 mm with a height of 600 mm and the conical section has an inside diameter of 80 mm with a height of 100 mm. Appendix E shows a study of the effect of computational domain size on the accuracy of the simulation results. Based on the study, there was no significant difference between the full and half domain, although the quarter domain showed significant error in the simulation data, particularly at distances towards the top of the reactor where the flow is fully developed. The 3D geometry of the current reactor was sliced into half, thereby reducing the computational domain and time and imposing an assumption of symmetrical flow.

### *3.2.2. Grid generation*

A grid independent study was conducted using three types of grids (fine, medium and coarse). The grids were created using ANSYS mesh as shown in Figure 3-1, where all the grids consisted of hexahedral cells structurally placed throughout the computational domain. When compared to the tetrahedral or triangle mesh, the hexahedral mesh can estimate a complex geometry resulting in fewer cells, lower computational cost and better numerical analysis (Pourtousi et al., 2015). The fine grid consisted of a total of 500 000 elements, with an element size of 1.2 mm, medium grid consisted of a total of 166 000 elements, with an element size of 2.56 mm and the coarser grid consisted of a total of 80 000 elements, with an element size of 25 mm.

The inflation feature was activated to capture the boundary layer at the walls and consisted of a maximum of 5 layers. Inflation is a boundary layer capturing method in CFD that is useful for resolving gradient variations at the wall of a variable of interest (ANSYS, 2011). The orthogonal quality of the fine, medium and coarse grids were 0.253, 0.245 and 0.247, respectively and these values are well within the acceptable range (ANSYS, 2010). Grid independent studies are still essential for multi-phase contacting equipment such as fluidized bed (photo)reactors. Detailed grid independent studies have revealed the relationship between particle size and cell size. Cloete et al. (2014) reported that small particle sizes require finer grids, whereas, larger particle sizes (~ 500 µm) are less strict to grid sizes. On overall, grid independent studies are useful in reducing the number of simulations and computational time.

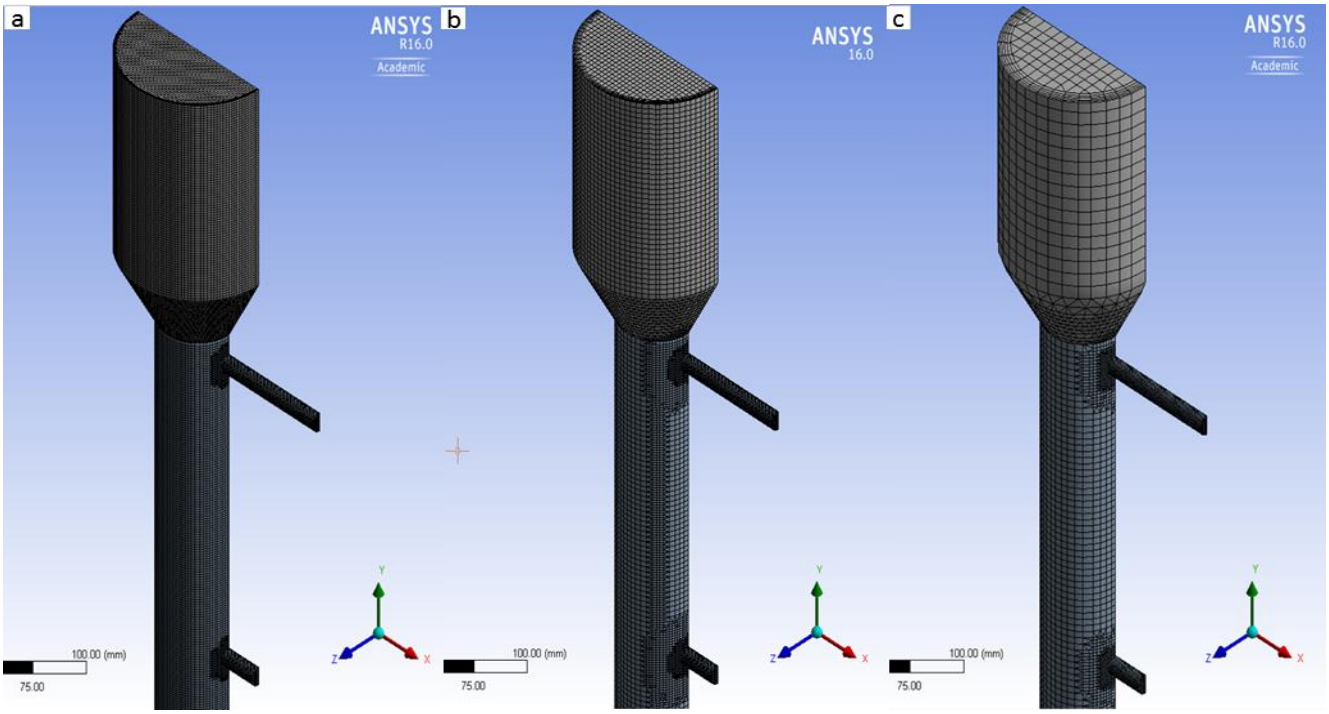


**Figure 3-1.** Simulation grid for a fluidized bed reactor: (a) fine grid; (b) medium grid and (c) coarse grid.

### *3.2.3. Initial and boundary conditions*

All simulations were carried out using air as the gas phase and deionized water as the liquid phase. The walls were set as a stationary wall with a no slip condition for both phases (Kulkarni et al., 2007). The air inlet, which was modelled as a distributor, was defined as a fully open inlet where the gas velocity was computed based on the superficial gas velocity of 20 mm/s with an air volume fraction of 1. The pressure outlet boundary condition was applied at the

liquid outlet and the degassing for the gas outlet (Li et al., 2009). The initial conditions specified are essential due to the fact that they influence the direction and accuracy of the solution. Therefore, to initialize the solution, parameters such as turbulence, volume fraction, axial, radial and tangential liquid and gas velocities were assigned the value of 0 at $t$ = 0 s as shown in Table 3-1.

For all the simulations, the gas distributor (that is a sintered plate) was modelled as a uniform gas inlet with a superficial gas velocity being specified (Li et al., 2009). The bubble diameter at the inlet of the gas distributor was assumed to be 1.96 mm based on experimental data (Kulkarni et al., 2007). The use of a single mean bubble size in bubble columns is a reasonable assumption when operating within the homogeneous flow regime (Liu & Hinrichsen, 2014).The specified bubble size was smaller than the medium grid cells (2.56 mm) but larger than the fine grid (1.2 mm). The backflow volume fraction was specified as 1 to reduce the entrainment of liquid.

**Table 3-1.** Solution initiation.

| Parameter | Value |
|---|---|
| $u_l$ , $v_l$ , $w_l$ , $v_g$ , $w_g$ (mm/s) | 0 |
| $u_g$ (mm/s) | 20 |
| $\in_g$ | $1x10^{-08}$ |
| $k$ (J/kg) | 0 |
| $\varepsilon$ ($m^2/s^3$) | 0 |

### *3.2.4. Numerical procedure*

All simulations were carried out using ANSYS Fluent 16.0 software that uses the finite control volume discretization method. There are several discretization methods: finite difference, Lattice Boltzmann and finite control volume, however, the finite control volume method can accurately compute single and multiphase flow inside a computational domain consisting of uniform and non-uniform grid (Pourtousi et al., 2015). The equations of continuity and momentum balance were solved, together with $k$-$\varepsilon$ equations, using the Euler two-fluid approach to obtain a complete flow pattern. What this approach does is that it captures the water (primary phase) as a continuous phase and air as a secondary dispersed phase thereby solving the continuity and momentum equations for each phase. The CFD simulations were carried out by varying the number of cells, discretization scheme and time step size to determine the combination that would produce the best accurate simulation data with minimal

simulation time. The interfacial forces were kept constant in all simulations and are listed in Table 3-2.

**Table 3-2.** Interfacial forces obtained from literature.

| Force | Law | Constant | Source |
|---|---|---|---|
| Drag | Grace | | Qi et al. (2011) |
| Lift | Saffman | | Qi et al. (2011) |
| Wall lubrication | Antal et al. | $C_{w1}$ = 0.0064, $C_{w2}$ = 0.016 | Krepper et al. (2005) |
| Turbulent dispersion | Burns et al. | 0.2 | |
| Turbulent interaction | Sato | 0.6 | Default |

The phase coupled SIMPLE algorithm, which is an extension of the SIMPLE algorithm for multiphase flow, was used for the pressure-velocity coupling and correction. The time step size was varied and all the simulations were computed for 30 s to obtain pseudo-steady state. The pseudo-steady state period was obtained by allowing the fluctuations of the surface monitors to stabilize, which occurred after 30 s of simulation time. The Under-Relaxation parameters were kept constant along with the convergence criteria of $1.0 \times 10^{-03}$ (Kulkarni et al., 2007). The CFD simulations were validated by comparing them to experimental data obtained from Kulkarni et al. (2007) and the average sum of square errors (ASSE) was used as a response parameter. The ASSE data between simulation and experiment was computed as:

$$E_i = \sum_{i=1}^{N} \left(x_i - \hat{x}_i\right)^2 \tag{58}$$

$$\overline{E} = \left(E_1 + E_2 + ... + E_n\right)/n \tag{59}$$

where $E_i$, $x_i$ and $\hat{x}_i$ are the relative error, predicted and experimental values of point i, respectively. $\overline{E}$ is the average of all the relative errors (ASSE).

## 3.3. Experimental methods

### *3.3.1. Materials and chemicals*

The photocatalyst that was used in the current study was the commercially available titanium dioxide ($TiO_2$) Degussa P25 due to its affordability, availability, insolubility in water, resistance to various chemicals and non-toxicity (Shahrezaei et al. 2012a). Titanium dioxide

mainly consists of anatase (± 98%) with a particle size of 30 nm (nano-sized) and a surface area of 49.2-50 $m^2/g$ (Shahrezaei et al., 2012b; Ohno et al., 2001) and was purchased from Sigma Aldrich (South Africa). Hydrochloric acid [32% (v/v)] and sodium hydroxide (solution) were used to adjust the initial pH level of the stock solution and were purchased from Labchem and Associated Chemical Enterprises, respectively. Phenol, that was used as a model pollutant to simulate petroleum wastewater, was purchased from Labchem. The chemicals used were of analytical reagent-grade quality and were used without any further purification. All the photodegradation and hydrodynamics experiments were conducted using deionized water that was obtained from a Milli-Q® Direct Water Purification System that purified tap water to reach a resistivity of 18.2 MΩ·cm (25°C) and a total organic carbon (TOC) value of 5 ppb.

### *3.3.2. Catalyst and wastewater preparation*

For economic reasons, a catalyst should have the capability to be recycled or regenerated in order to be reused as this reduces the cost of the catalyst loading. A limiting factor with the $TiO_2$ photocatalyst is its nano-sized character and therefore creates the difficulty of separating it from the petroleum wastewater post treatment. Due to this limiting factor, the $TiO_2$ photocatalyst in the current study was agglomerated to form denser particle sizes using colloidal silica, consequently enhancing separation after treatment. The petroleum wastewater was simulated by synthesizing a stock solution consisting of phenol (model contaminant) at a specific concentration (30 ppm). The motive behind using phenol as a model pollutant is due to the fact that it is the most common pollutant present in petroleum and/or industrial wastewater systems (Ochieng et al., 2003). In addition, the concentration of phenol used in the experiment falls between the range found in literature (Coelho et al., 2006).

A catalyst composite, containing 60% $TiO_2$ in silica solution, was synthesized based on a study of Khune et al. (2014). Specific amounts of $TiO_2$ and colloidal silica solution were mixed together inside a beaker by hand to form a Bingham plastic mixture (non-Newtonian). The mixture was then laid on a glass bowl and oven dried at 60°C to remove moisture. The dried sample was then crushed and screened to a particle size range of 300 – 1000 µm. The screened particles were then washed with 0.1 M HCl to remove left-over alkalinity. The acidified particles were neutralized several times, by using deionized water and air dried for 24 hours to obtain the final composite catalyst. During the neutralization process, the pH level of the wash was monitored until it reached a neutral value (~ 6.8).

### *3.3.3. Analytical methods*

As aforementioned, phenol was used as a model pollutant and before analysis, the samples were filtered through a 25 mm syringe filter consisting of a 0.45 µm glass fiber prefilter (GHP) membrane. The concentration of phenol was determined using a PerkinElmer Flexar™ FX-10 ultrahigh performance liquid chromatography (UHPLC) system. The system consisted of a PerkinElmer Series photodiode array (PDA) plus detector, autosampler, Brownlee Validated C8 column (150 mm x 4.6 mm, 5 µm particle size) and two UHPLC pumps. The PDA detector operated at specific excitation and emission wavelengths that were 275 nm and 313 nm, respectively. The mobile phase was made up of methanol and pure water at 60% and 40% (v/v), respectively, and were pumped at a flowrate of 1.0 mL/min. The injection volume was 50 µL and the detection response time was 0.1 s.

The total organic carbon (TOC) was analysed using the Teledyne Tekmar TOC Torch analyser. The Torch analyser uses a Static Pressure Concentration for the analysis of TOC using high temperature combustion. It has an autosampler with three vial rack choices, automated calibration and intellidilution that dilutes over-range samples to within the working calibration, PC driven control and has a carbon detection level range of 50 ppb to 30 000 ppm.

### *3.3.4. Experimental design*

The HPO process consists of numerous operating variables that affect the response of the system. The performance of this process is highly dependent on proper selection and optimization of the process variables. Some of the effects are minimal whilst others are quite significant. Past experiments have shown that the HPO process is primarily influenced by four operating variables which are: reaction time, pH level, superficial gas velocity and catalyst loading (Shahrezaei et al., 2012a; Cheng et al., 2012). Therefore, based on literature, these were the operating variables that were investigated by determining their effect on the photodegradation of phenolic wastewater using the central composite design.

The experimental design used in the current study was the full factorial with axial points and was selected due to its ability to examine the results changing several variables simultaneously; thereby revealing the interdependency of the parameters. While this design is complex, the advantages are, it is less costly and less time consuming. Table 3-3 shows the factorial design set-up consisting of four variables (k = 4) and the coded variables, determined by using Equation 34, were set at five levels: -2 (minimum), -1 (low), 0 (central), +1 (high) and +2

(maximum). After conducting the experiments according to the experimental matrix (Table 3-3), response surface modelling was conducted by applying the central composite design (CCD), using Design Expert® Software of Stat-Ease Inc. (version 6.0.6), to model and optimize the reaction conditions.

**Table 3-3.** Experimental design.

| Parameter | Levels | | | | |
|---|---|---|---|---|---|
| | **-α (-2)** | **-1** | **0** | **+1** | **+α (+2)** |
| Initial pH level | 2 | 3.5 | 5 | 6.5 | 8 |
| Catalyst loading (g/L) | 0 | 1 | 2 | 3 | 4 |
| Reaction time (min) | 60 | 120 | 180 | 240 | 300 |
| Superficial gas velocity (mm/s) | 5.77 | 8.66 | 11.55 | 17.32 | 23.10 |

Accordingly, the overall experimental design consisted of 30 experiments, determined by using Equation 35, that were made up of 8 axial points ($n_A$), 16 full factorial points ($n_F$) and 6 replications at the centre ($n_C$). In CCD, the major operating parameters' pH level (A), catalyst loading (B), superficial gas velocity (C) and reaction time (D) were considered as independent variables, whereas the phenol degradation (%) was observed as a response variable. A sequential model fitting test was conducted to select a suitable model. A second-order polynomial model (Equation 33) was used to fit the data found from the 30 experiments. Analysis of variance (ANOVA) was used to attain the interaction between the process variables and the response parameter, to determine the statistical significance and reliability of each term in the polynomial model and to determine the graphical analysis of the data. The regression coefficients in the polynomial equation were used to produce 3D surface response and contour plots. Optimization of the process variables was carried out by solving the regression equation and graphical analysis of the data.

## 3.4. Hydrodynamic experiments

The global gas hold-up measurements were carried out to validate the effectiveness of the developed model and to characterize the hydrodynamic behaviour of the reactor. The global gas hold-up gives a direct indication of the amount of gas present in the reactor and the availability of oxygen for the oxidation-reduction reactions. The global gas hold-up ($\in_G$) is defined as the average volumetric gas fraction present in the entire domain of the reactor and

was determined by observing the displaced height of the clear liquid (Ellenberger & Krishna, 2003; Li & Zhong, 2015).

$$\epsilon_G = \frac{H_D - H}{H_D} \tag{60}$$

where $H_D$ is the displaced height during gas sparging and $H$ is the static clear liquid height with no gas sparging.

## 3.5. Photodegradation experiments

The photocatalytic degradation of phenol was performed using a solar photocatalytic fluidized bed reactor. All the photodegradation experiments were conducted outdoors (rooftop) to utilize the sunlight as an ultraviolet (UV) source and the reactor was operated in batch mode. The light intensity of sunlight fluctuates throughout the day, therefore, to capture as much sunlight as possible, the experiments were conducted between 09:00 to 15:00. Figure 3-2 shows a schematic diagram of the reactor that is cylindrically shaped ($H$ = 600 mm and $d_i$ = 40.8 mm) with a top conical section ($H$ = 100 mm and $d_i$ = 80 mm) that was used for degassing.

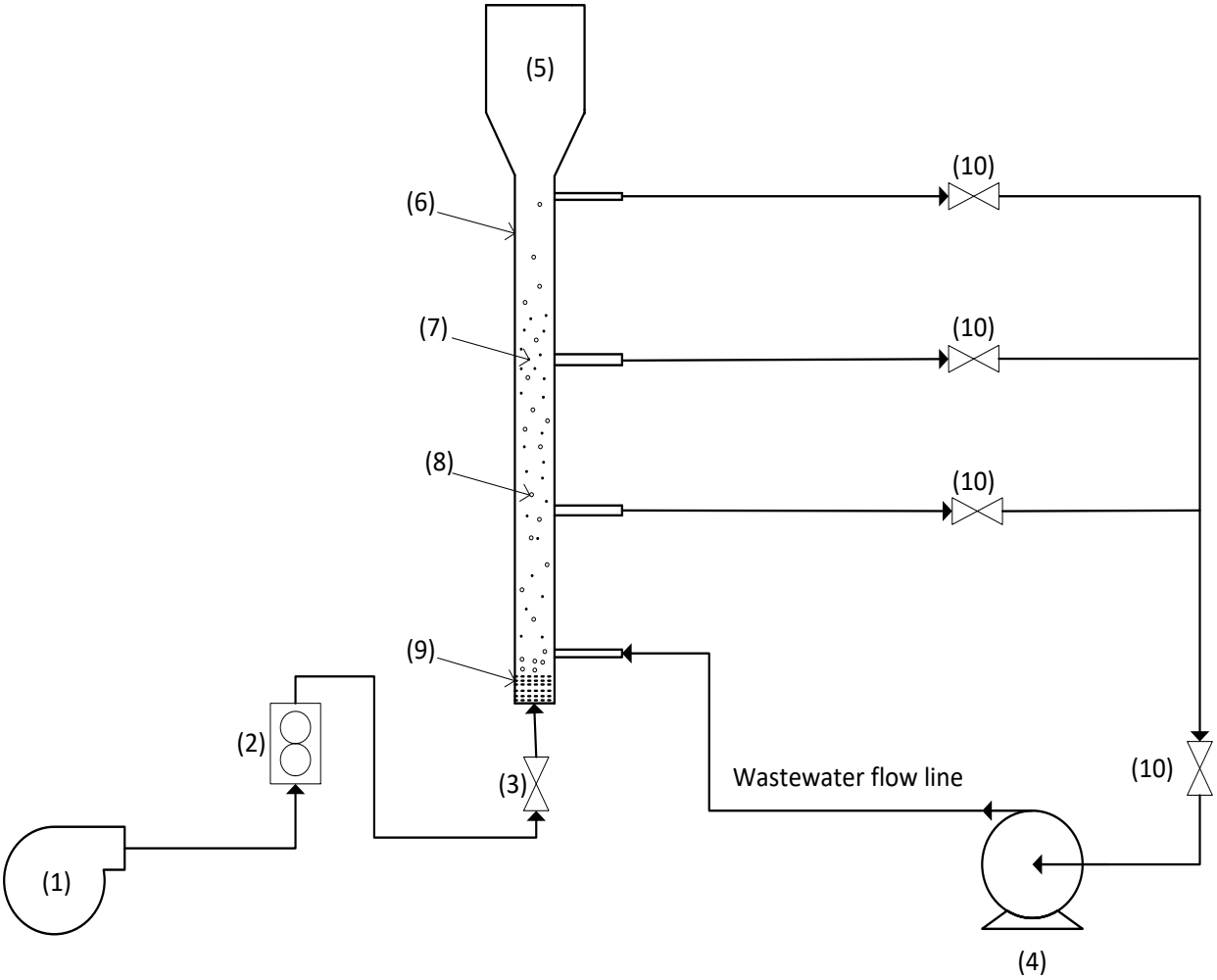


**Figure 3-2.** Experimental setup of a solar photocatalytic fluidized bed reactor. (1) Compressor; (2) Flowmeter; (3) Non-return valve; (4) Peristaltic pump; (5) Degassing zone; (6) Fluidized bed photoreactor; (7) Catalyst particles; (8) Air bubbles (9) Gas distributor and (10) Ball valves.

The reactor consisted of 4 strategically placed side-ports, where the top (wastewater outlet) and bottom (wastewater inlet) side-ports were used for wastewater recirculation by a peristaltic pump. The purpose of wastewater recirculation was to assist in the hydrodynamic mixing within the reactor. Although it somewhat complicates the hydrodynamic behaviour it is more effective than having a static column of liquid. The reactor was made out of borosilicate glass that is a material that has been extensively used by researchers for photocatlysis using sunlight as a UV source (Boyjoo et al., 2013; Shahrezaei et al., 2012b). Shiota et al. (2016) demonstrated that borosilicate (pyrex type) has good photon emission capabilities. During all the experiments, 850 mL of aqueous phenol feed solution with a concentration of 30 ppm was transferred into the reactor. The initial pH of the feed solution was adjusted accordingly using HCl (1.0 M) or NaOH (1.0 M) and the pH level was measured using a pH meter (Inolab model

no. 7110). The composite catalyst was loaded into the reactor and a peristaltic pump was used for wastewater recirculation. A compressor was used to feed air into the reactor through the bottom, where it was evenly distributed by a sintered plate type distributor with a pore size of 10 - 15µm. The bed was fluidized by the air.

## 3.6. Reaction kinetics experiments

The Langmuir-Hinshelwood (L-H) model (Equation 26) is generally used to determine the reaction kinetics of organic water impurities such as aniline, phenol and its derivatives. It was reported that the L-H model follows the pseudo first-order decay kinetics (Shahrezaei et al., 2012a). The preference of the L-H model by many researchers is due to its ability to account for both the adsorption (*b*) and photodegradation (*k*) kinetics. The adsorption and photodegradation reaction kinetics were evaluated by monitoring the TOC as a response variable for the degradation of phenol.

The kinetic experiments were setup and operated similarly to the photodegradation experiments (Figure 3-3). However, the TOC analyses were conducted in 30 min intervals for a period of 3 hours. The optimal operating conditions obtained from the photodegradation experiments were used to conduct the reaction kinetic experiments. The TOC reduction ( $TOC_R$) was determined by:

$$TOC_R = \frac{C_{TOC_0} - C_{TOC}}{C_{TOC}} \text{ x } 100\% \tag{61}$$

where $C_{TOC_0}$ and $C_{TOC}$ are the concentrations of total organic carbon initially and after, respectively.

To evaluate the results of Bechambi et al. (2015) and Kim Phuong et al. (2016), where it was reported that when the initial concentration of pollutant is low and/or adsorption is relatively weak, then Equation 26 can be employed. The adsorption study was conducted first by covering the reactor with a dark black plastic to prevent light energy from penetrating into the reactor. As soon as TOC reached equilibrium, the plastic was removed and photodegradation commenced.

Samples of 50 mL were taken from the agitated wastewater solution in 30 min intervals, filtered through a 25 mm syringe filter consisting of a 0.45 µm glass fibre prefilter membrane

and analysed using the Teledyne Tekmar TOC Torch analyser. The TOC data were used to fit both the linear and second-order models to determine the reaction order. In addition, the coefficient of regression ($R^2$) was used to determine the best fitting empirical model and the chosen empirical model was used to determine the apparent reaction rate constant.

# CHAPTER 4

## 4. Results and discussion

The study involved investigating the treatment of petroleum wastewater by means of the HPO process. Computational fluid dynamic simulations were carried out to understand and optimize the hydrodynamics (axial liquid velocity, local gas hold-up and turbulent quantities) inside the fluidized bed photoreactor. In addition, the photodegradation experiments were conducted to determine the efficiency of this process, moreover, response surface modelling was applied to optimize the photodegradation operating parameters. The reaction kinetics were investigated to understand the reaction mechanism of the photodegradation. The results and analysis of experimentation, simulation and statistical modelling are discussed in this section.

### 4.1. CFD simulation

The influence of CFD setting methods (time step size, discretization scheme and grid size) on the simulation accuracy and convergence was studied by using a 3-level factorial design (Table 4-2) and the simulations were validated by comparing them to experimental data obtained from Kulkarni et al. (2007). Optimization of the setting methods was examined by using the desirability technique which would result in a model consisting of optimal CFD setting methods. The model developed was then validated by studying the effect of superficial gas velocity on the global gas hold-up where the CFD simulations were compared to experimental results generated by the author.

#### *4.1.1. Grid independence*

A grid independent study was conducted as shown previously in Figure 3-1. Three sizes of the simulation grids (coarse, medium and fine) were generated using the commercial software ANSYS mesh. For all the cases of the grid independent study, the CFD setting methods such as discretization scheme, time step size, turbulence model and interfacial forces were all kept constant. The results shown in Table 4-1 are summarized results meaning detailed results of the grid independent study are shown in Appendix A (Grid independence study results). The results obtained (Table 4-1) show that the fine grid size gave the least error (0.0308), whereas the coarse grid size gave the highest error (0.0524).

A grid size with fine structured cells produces reasonable accuracy due to the fact that the grid is aligned with the discretization of the governing equations of each cell (Laborde-Boutet et al., 2009). Furthermore, fine grid structures work well for studies consisting of particle sizes

similar to the grid size (Cloete et al., 2014). The cell size for the fine grid was 1.2 mm, which is smaller than the bubble size used (1.96 mm). However, the grid was well aligned with the flow path thus producing the least amount of error. The medium grid had the lowest error when compared to the coarse grid. However, there was no significant difference in the error between the medium and coarse grids, as shown by Table 4-1. Therefore, to simplify and reduce the number of simulations to be carried out; only the fine and coarse grids were considered in the numerical optimization study.

**Table 4-1.** Grid independence study.

| Grid resolution | Error |
|---|---|
| Fine (500 000) | 0.0308 |
| Medium (166 000) | 0.0506 |
| Coarse (80 000) | 0.0524 |

### *4.1.2. Numerical optimization*

As mentioned in section 3.2.4 (*numerical procedure*), the CFD simulations were carried out by varying the number of cells, discretization scheme and time step size to determine the combination that would produce the best accurate simulation data with minimal simulation time. Table 4-2 shows the 3-level factorial design where the CFD settings where optimized by using a numerical optimization technique called desirability.

The comparison between the simulation data and the experimental results (obtained from Kulkarni et al., 2007) was done by evaluating the axial liquid velocity, local gas hold-up, turbulent kinetic energy and turbulent dissipation rate, thereby resulting in four response surface parameters. In addition, the average relative error (ASSE) was used to assess the accuracy of all the simulations and was calculated using Equation 84. Table 4-2 shows the ASSE data (four response parameters) for all CFD simulations along with their respective desirability function. After conducting an analysis of the response parameters, it was noted that there was a significant difference between the ASSE data for each response parameter. For instance, in the first row of Table 4-2, the ASSE values for the axial liquid velocity, gas hold-up, turbulent kinetic energy ($k$) and turbulent dissipation rate ($\varepsilon$) were 0.061, 0.0133, 0.0003, and 0.0237, respectively. Therefore, to obtain a simulation run that had the least average error, a numerical optimization technique referred to as the desirability function was used.

The desirability approach is the most widely used technique for the optimization of multiple response processes (Islam et al., 2009). This numerical optimization technique uses statistical mathematical formulations (Equations 18 to 21) to evaluate the desirability of each response parameter by assigning numbers between 0 and 1. Here, 0 represents an undesirable value and 1 a completely desirable value. Furthermore, the individual desirability values were then combined using a geometric mean giving an overall desirability (Equation 22) (Islam et al., 2009). It is worth noting that from this point onwards, the individual simulation Runs under Table 4-2 will be coded to provide clarity when discussing the simulation results and to avoid confusion. The coded names are shown as such:

| | | |
|---|---|---|
| F - Fine grid | 1 - 1st order scheme | 0.1 - Large time step (L) |
| M - Medium grid | 2 - 2nd order scheme | 0.01 - Intermedia te time step (I) |
| C - Coarse grid | Q - QUICK scheme | 0.001 - Small time step (S) |

For instance, when referring to Run 1 under Table 4-2, the coded name of F2S will be used that signifies a fine grid of 500 000 cells, 2nd order discretization scheme and a small time step size.

From Table 4-2, F2S and CQS had the highest desirability values, whereas FQL had the least desirability. It is worth noting that out of a total of 18 simulations conducted for the optimization study, only 15 are shown in Table 4-2. The three additional simulations were automatically removed from the table by the statistical tool due to their significantly low desirability values.

The low desirability value obtained by FQL was due to a relatively large time step size (0.1) coupled with a high discretization scheme (QUICK). In addition, convergence of FQL was fairly hard although the simulation time was relatively fast; it resulted in erroneous data as can be shown by its low desirability. F2S and CQS had desirability values of 0.985 and 0.978, respectively, denoting good accuracy. Li and Zhong, (2015) conducted a CFD simulation study where they studied the hydrodynamics in a three-phase bubble column. They varied the discretization schemes, times step size and grid-size. Their grid-sizes were relatively coarse (32 436, 56 865 and 95 788), however, they found that the $2^{nd}$ order discretization scheme and time step size of 0.001 had the lowest error in both the radial and axial positions.

Furthermore, an Analysis of Variance (ANOVA) was conducted on the simulation results to show the interaction between the CFD settings methods (Appendix B (CFD optimization

results). In addition, an empirical first order polynomial equation was developed that can be used to determine the error from the CFD setting methods. From the ANOVA study, it was seen that each of the CFD setting methods was significant (P-values were less than 0.05). In the current study, the simulation results for axial liquid velocity, gas hold-up and turbulence profiles were compared to experimental data obtained from literature (Kulkarni et al., 2007). For each response variable, two simulations with the least error were selected and comparison with experimental results is shown graphically.

**Table 4-2.** Numerical optimization results.

| Run | Factor 1 | Factor 2 | Factor 3 | Response 1 | Response 2 | Response 3 | Response 4 | | |
|---|---|---|---|---|---|---|---|---|---|
| | A: No. of cells | B: Scheme | C: Time step | SSE (Axial liq. Velocity) | SSE (Gas hold-up) | SSE ($k$) | SSE ($\varepsilon$) | Desirability | |
| 1 | 500,000 | 2nd order | 0.001 | 0.061* | 0.0133* | 0.0003 | 0.0237* | 0.985 | Selected |
| 2 | 80,000 | QUICK | 0.001 | 0.089 | 0.0208 | 0.0002 | 0.026* | 0.978 | |
| 3 | 80,000 | 2nd order | 0.001 | 0.169 | 0.0148* | 0.0001* | 0.0262 | 0.975 | |
| 4 | 80,000 | 1st oder | 0.001 | 0.081 | 0.0236 | 0.0004 | 0.0239 | 0.964 | |
| 5 | 500,000 | QUICK | 0.001 | 0.086 | 0.0222 | 0.0006 | 0.0238 | 0.951 | |
| 6 | 500,000 | 1st oder | 0.01 | 0.073 | 0.1091 | 0.0001* | 0.0369 | 0.854 | |
| 7 | 80,000 | 2nd order | 0.01 | 0.127 | 0.0202 | 0.0016 | 0.0562 | 0.824 | |
| 8 | 80,000 | 2nd order | 0.1 | 0.183 | 0.0348 | 0.0019 | 0.0369 | 0.813 | |
| 9 | 500,000 | 2nd order | 0.01 | 0.063* | 0.1013 | 0.0012 | 0.0361 | 0.799 | |
| 10 | 500,000 | QUICK | 0.01 | 0.066 | 0.0978 | 0.0010 | 0.0590 | 0.792 | |
| 11 | 80,000 | QUICK | 0.1 | 0.170 | 0.1309 | 0.0013 | 0.0742 | 0.691 | |
| 12 | 500,000 | 1st oder | 0.001 | 0.121 | 0.1896 | 0.0003 | 0.0437 | 0.660 | |
| 13 | 500,000 | 1st oder | 0.1 | 0.117 | 0.1754 | 0.0015 | 0.0691 | 0.607 | |
| 14 | 500,000 | 2nd order | 0.1 | 0.131 | 0.1809 | 0.0014 | 0.0691 | 0.599 | |
| 15 | 500,000 | QUICK | 0.1 | 0.213 | 0.1837 | 0.0017 | 0.0713 | 0.562 | |

* Values that have the least error in their respective columns and are graphically discussed in the succeeding sections.

### *4.1.3. Response surface analysis*

The contour plots are a good approach to obtain an insight into the effect of each variable in a factorial experiment (Fakhri et al., 2016). Since the current experiment consisted of several factors, therefore making it a quantitative experiment; contour plots are useful in visualizing the effects of several factors on a response parameter. Figure 4-1 shows a contour plot of the effect of discretization scheme and number of cells on a response parameter (error), whereby the time step size was kept constant (0.001). Literature has shown that an increase in the number of cells results in a more accurate (less error) solution at a cost of prolonged computation time,

whereas a decrease in the number of cells produces a less accurate solution with less computational time (Laborde-Boutet et al., 2009).

This can be seen in Figure 4-1 where the 2nd order scheme obtained an error of 0.169 for 80 000 cells and decreased to 0.066 for 500 000 cells. However, the 1st order and QUICK scheme did not display the same trend. This was due to the fact that the QUICK scheme is stubborn to converge, particularly in a fine mesh, thus resulting in an erroneous solution (Li & Zhong, 2015). The 1st order scheme is quite straightforward to converge and requires less computational time, however, it results in a less accurate solution.

The misalignment between the simulation grid and the flow path, particularly in the liquid recirculation zones, increases the numerical diffusion error in the 1st order scheme (Laborde-Boutet et al., 2009). It is evident when observing the difference between the 1st order and QUICK scheme for both number of cells. There is a decrease in error signifying that the QUICK scheme is more accurate than the 1st order scheme. From Figure 4-1, it is evident that a simulation grid of 500 000 cells and a 2nd Order discretization scheme results in good accuracy (least error) and convergence.

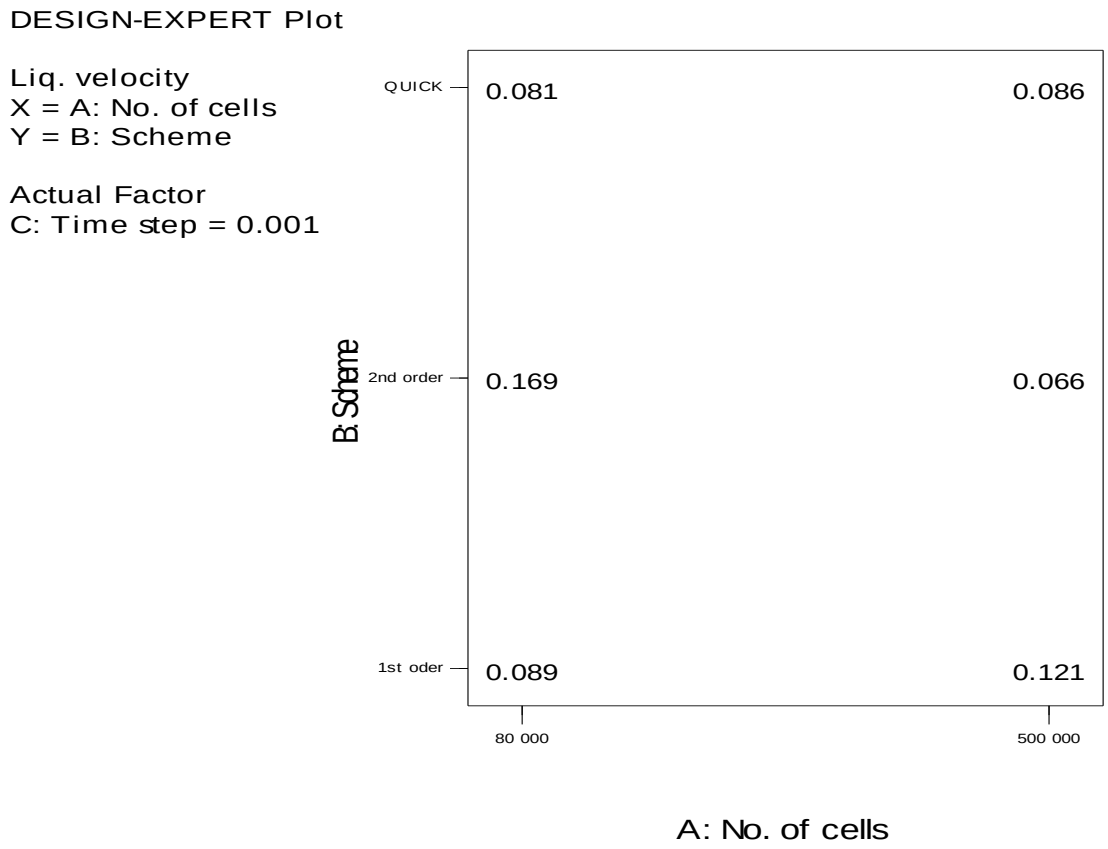


**Figure 4-1.** Effect of discretization scheme and number of cells on a response parameter (error), whereby the time step size was kept constant (0.001).

### *4.1.4. Axial liquid velocity profiles*

**Figure 4-2** shows the comparison between CFD and experimental data for axial liquid velocity profiles at different axial locations (*H/D* = 0.2, *H/D* =2.6 and *H/D* = 5.0) of the reactor. Here, an axial location of *H/D* = 0.2 is near the distributor region, *H/D* = 2.6 is located at the middle of the reactor and *H/D* = 5.0 is towards the top of the reactor, before the gas disengagement zone. The plot for axial liquid velocity profile displayed a radial variation for all three figures, whereby, the liquid velocity had an upward movement at the centre and a downward movement near the wall.

This was caused by the recirculation of the liquid as the gas flows up the column (Kulkarni et al., 2007). Bubbles tend to move at higher velocities than the liquid in the central region, therefore the dissipation rate is less than the energy input rate. This form of energy transfer maintains the liquid recirculation rate (Kulkarni et al., 2007). The experimental data in **Figure 4-2**a showed turbulent swirling flow between 0.2 and 0.5 (normalized radial distance) and this

is towards the distributor region where gas is introduced into the reactor and the recirculating liquid is changing its flow direction. The axial liquid velocity was low towards the distributor region and increased up the reactor where the flow was fully developed. As the bubbles enter the reactor, they tend to accelerate due to the buoyancy force that is initially greater than the drag and gravitational forces. Due to momentum conservation, the displaced liquid will experience the same acceleration and this was modelled by the virtual mass force. The bubbles accelerate until the buoyant force is in equilibrium with the sum of the drag and gravitational forces. At this point, the bubbles have reached their terminal velocity and continue travelling up the reactor till the disengagement section is reached.

The F2S (2nd Order scheme) accurately captured the axial liquid velocity profiles in all three locations and gave the best prediction. However, the CFD prediction of the axial liquid velocity was poor towards the wall and this was due to the presence of small eddies that limit the ability of the standard $k$-$\varepsilon$ model to model near the wall turbulence. It has been reported that the 2$^{nd}$ order scheme uses a multidimensional linear reconstruction method thus resulting in second-order accuracy (ANSYS, 2010) and good convergence. On the other hand, the QUICK scheme uses a higher-order discretization method that requires high computing power and causes convergence difficulties. Laborde-Boutet et al. (2009) studied the influence of numerical discretization schemes. They reported that the high-order schemes reduce the numerical diffusion errors significantly. However, higher-grade numerical schemes (QUICK and third-order MUSCL scheme) are recommended for rotating and swirling flows (Laborde-Boutet et al., 2009) and are persistent in converging.

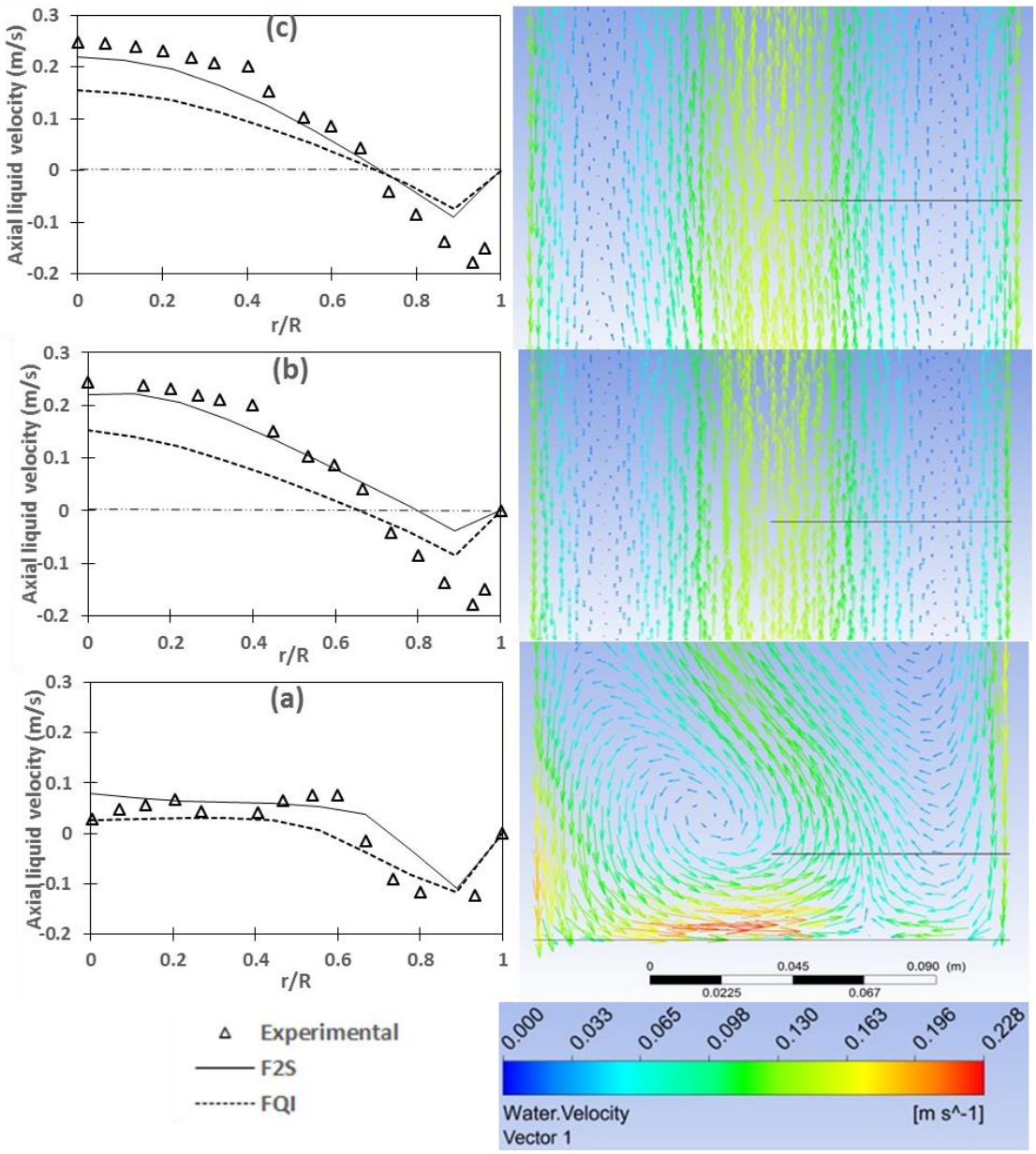


**Figure 4-2.** Comparison between the simulated and experimental axial liquid profiles at different axial positions. (a) H/D = 0.2; (b) H/D = 2.6 and (c) H/D = 5.0.

The axial liquid velocity data showed a turbulent swirling profile towards the bottom of the reactor (H/D = 0.2) and the profile developed well at distances away from the distributor region. The swirling profile obtained in **Figure 4-2**a was due to the turbulence introduced by the bubbles as they enter the reactor. A suitable way to visualize eddy turbulence in the liquid phase, that is shown in **Figure 4-2**a, is by using a vector plot. **Figure 4-3** shows a comparison between an XY plot (**Figure 4-3**a) and a vector plot (**Figure 4-3**b) where the XY plot represents

the axial liquid velocity at an axial location of H/D = 0.2. The vector plot shows the axial liquid velocity towards the distributor region of the reactor. The axial liquid velocity shown in **Figure 4-3**a was drawn from the black line shown in **Figure 4-3**b and represents data drawn from the centre of the reactor all the way to the wall.

As stated earlier, **Figure 4-3**a exhibits a vortex trend between the normalised radial distances of 0.2 to 0.5. This kind of trend was properly captured by the vector plot. In **Figure 4-3**b, specifically on the black line towards the centre of the reactor, there is a swirling flow of the liquid that is caused by the entering bubbles and the downward flow liquid at the wall. However, towards the wall of the reactor, there is a downward flow of the liquid velocity as shown by the downward facing vector line arrows. This downward flow shown by the vector plot can also be seen in the XY plot (**Figure 4-3**a) where the liquid velocity is negative at normalised radial distances of 0.75 to 0.98. Therefore, the vector plot has supported the trend that was shown by the XY plot. Detailed vector plots of the axial liquid velocity are shown in Appendix C.

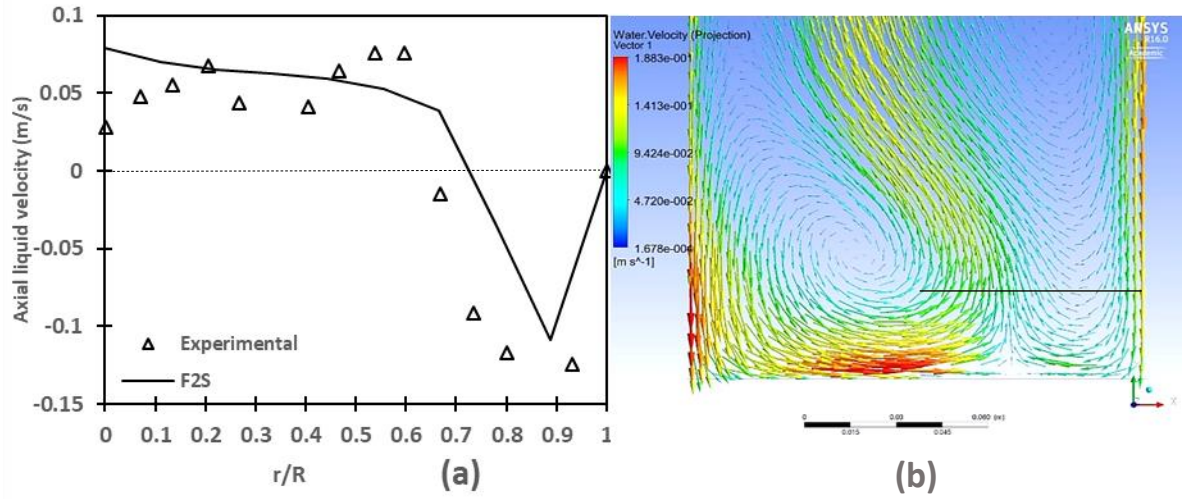


**Figure 4-3**. Comparison between (a) XY plot and (b) vector plot of axial liquid velocity profile.

### *4.1.5. Local gas hold-up profiles*

An efficient and simple way to understand mixing within the reactor is to study the variation of gas hold-up. Figure 4-4 shows the plot of gas hold-up at different axial locations with a superficial gas velocity of 20 mm/s. The simulations were carried out in the homogeneous regime implying that the bubbles move with virtually similar velocities, sizes and with minimal



(b)

coalescence and break-up. This creates an added advantage of specifying a single bubble diameter (1.96 mm).

The simulation results (Figure 4-4) gave a high gas hold-up towards the centre and a radial decrease when approaching the wall with an average radial gas hold-up of about 0.116. It is shown in **Figure 4-2** that the liquid velocity varies at different axial locations of the reactor. Therefore, the lift force induced by the liquid causes the bubbles to rise faster towards the centre of the reactor and slower towards the wall (Kulkarni et al., 2007). This is comparable to the results of Kulkarni et al. (2007) and Tabib et al. (2008) who obtained an average radial gas hold-up of about 0.085 and 0.10, respectively. The prediction of the gas hold-up was poor towards the distributor region (Figure 4-4a) and developed well at distances away from the distributor (Figure 4-4b and c) implying that the free surface modelling was suitable towards the top. The gas hold-up axial profile develops due to the axial changing reduced pressure gradient that increases the bubble free area towards the disengagement zone. This results in more gas bubbles towards the centre and less near the wall. The CFD local gas hold-up profile for F2S compared well with the experimental data in Figure 4-4b and c. in relation to C2S.

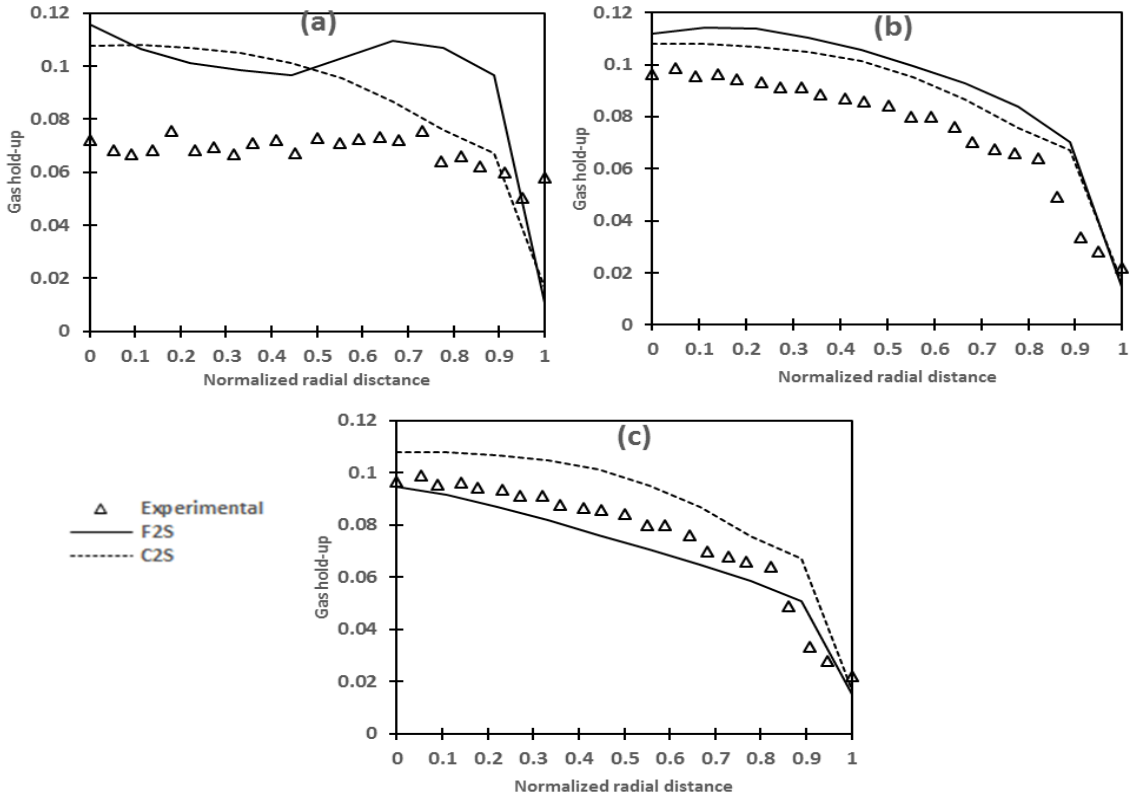


**Figure 4-4.** Comparison between the simulated and experimental gas hold-up profiles at different axial positions. (a) H/D = 0.2; (b) H/D = 2.6 and (c) H/D = 5.0.

Figure 4-5 shows the comparison between an XY plot and a contour plot for radial profile of gas hold-up. The data for Figure 4-5a was obtained from the black line shown in Figure 4-5b at an axial distance of H/D = 2.6. Figure 4-5b shows an aerial view of the gas hold-up and it can be seen that the local gas hold-up is ~ 0.115 at the centre of the reactor and radially decreases to a value of about 0.02 near the wall of the reactor. Similar to the axial liquid velocity data, the local gas hold-up data had a flat trend towards the distributor region (H/D = 0.2), due to the gas being introduced, and developed a radial profile at distances away from the distributor region. The F2S gave the best prediction of local gas hold-up, particularly at distances away from the distributor region.

As the bubbles rise, they entrain some of the liquid and due to mass conservation, an equal amount of liquid needs to fall back. The falling liquid creates a velocity gradient that results in driving the bubbles towards the centre causing the bubbles to concentrate towards the central region. This was modelled by the Lift force. In addition, it is pleasing to see the contour plot in agreement with the XY plot. Complete contour plots of the reactor are shown in Appendix D.

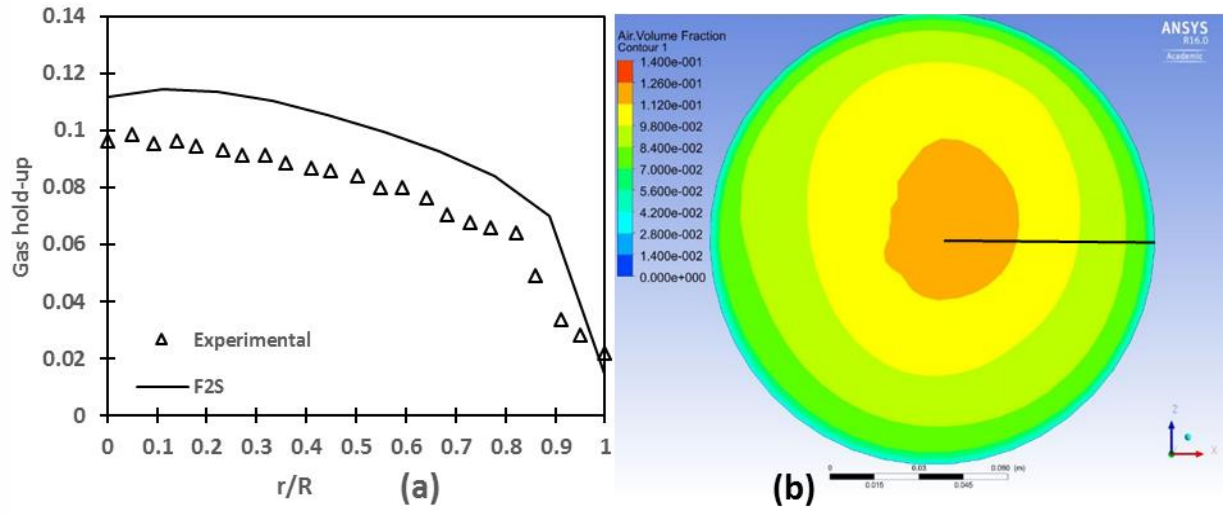


**Figure 4-5.** Comparison between (a) XY plot and (b) contour plot of radial gas hold-up.

### *4.1.6. Turbulent kinetic energy profiles*

Modelling turbulence is often a complex task due to an increase in the number of terms that require closure in the momentum equation. In the current study, the standard *k-ε* model, coupled with near-wall enhancement treatment, was used due to its simplicity, good convergence and low computational requirements. The two turbulent quantities that were used to capture the

turbulent characteristics were the turbulent kinetic energy ($k$) and turbulent dissipation rate ($\varepsilon$) where the bubble-induced turbulence is modelled from their governing equations.

As the bubble moves through the liquid phase, it transfers its pressure energy into the liquid and this energy is converted into turbulent kinetic energy due to the drag force (Equation 57). At steady state conditions, the total energy carried by a swarm of bubbles is mostly used to pump the stagnant liquid, from bottom to top, resulting in an intense liquid recirculation (Kulkarni et al., 2007). This is also confirmed by the axial liquid profiles (**Figure 4-2**) where the liquid velocity increased due to the acceleration of the bubbles and this, in turn, provides more turbulent kinetic energy. As a result, the energy related with the liquid is less at the bottom than at the top. This is shown by Figure 4-6 where the turbulent kinetic energy increases at distances away from the distributor region. However, the induced turbulent liquid motion is locally dissipated (turbulent dissipation rate) through eddies found in the liquid phase.

The turbulent kinetic energy showed an overall trend of constant value towards the centre and decreased near the wall (Figure 4-6). At distances away from the distributor region, there was an increase in the turbulent kinetic energy that corresponds to literature. Since the energy provided by the bubbles to the liquid is due to the drag force; and the lift force causes the bubbles to concentrate towards the central region, the turbulent kinetic energy tends to be higher in the centre of the reactor than near the wall. C2S accurately predicted the turbulent kinetic energy towards the distributor (Figure 4-6a) and deviated slightly at distances towards to the top of the reactor (Figure 4-6b and c) but predicted the overall trend of the experimental data better than F1I. The standard $k$-$\varepsilon$ model is grounded on the assumption of isotropic flow. This suggests that it assumes that the normal stress components are equal to each other (Tabib et al., 2008). This causes the turbulent characteristics to be equally distributed, resulting in inaccurate turbulence profiles.

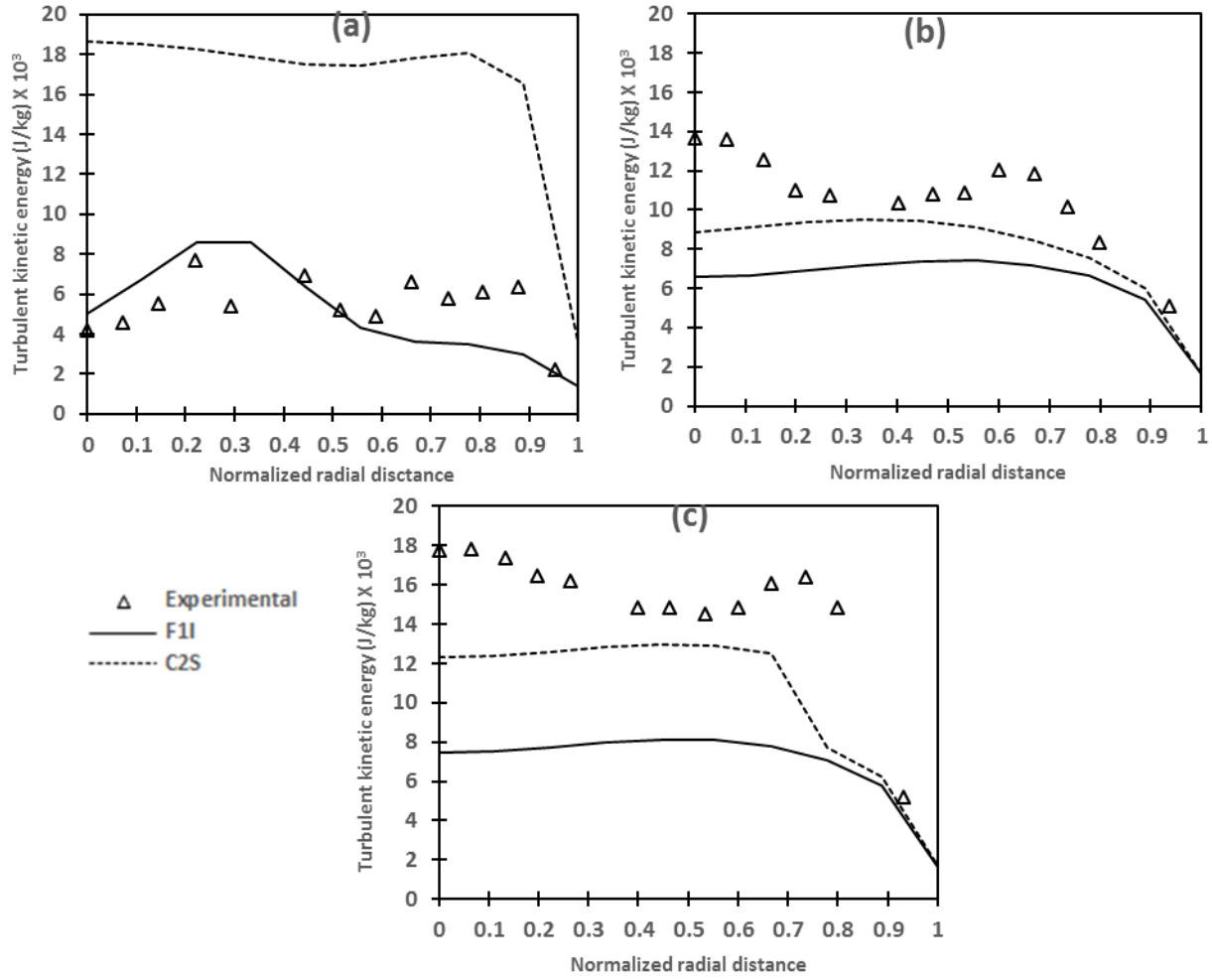


**Figure 4-6.** Comparison between the simulated and experimental turbulent kinetic energy profiles at different axial positions. (a) H/D = 0.2; (b) H/D = 2.6 and (c) H/D = 5.0.

### *4.1.7. Turbulent energy dissipation rate*

Figure 4-7 shows the radial variation of the turbulent energy dissipation rate at different column heights. The dissipation rate profiles showed a constant trend towards the centre with a slight increase from $r/R$ = 0.2 to $r/R$ = 0.8 followed by a sharp increase near the wall. This similar trend was reported by Liu & Hinrichsen (2014) and Kulkarni et al. (2007). Analogous to the turbulent kinetic energy, the dissipation rate increased away from the distributor due to an increase in the turbulent kinetic energy away from the distributor region. The radial and axial variation of turbulent energy dissipation rate is obtained from the turbulent model used and subsequently computed by suitable volume integration (Tabib et al., 2008). Since the turbulent

energy dissipation rate is the frequency at which the turbulent kinetic energy is being dissipated by the small eddies, it should balance to the energy introduced by the bubbles (Equation 86).

For instance, as the bubbles travel up the reactor part of the energy introduced by the bubbles is transferred into the liquid phase and converted into turbulent kinetic energy. The turbulent kinetic energy is characterized by large and small eddies. The small eddies are located towards the wall of the reactor and they dissipate most of the turbulent kinetic energy. This is the reason why the turbulent energy dissipation rate increases towards the wall. The turbulent dissipation rate data corresponds well with the turbulent kinetic energy data. F2S gave the best prediction whilst CQS deviated significantly from experimental data, particularly, at distances away from the distributor.

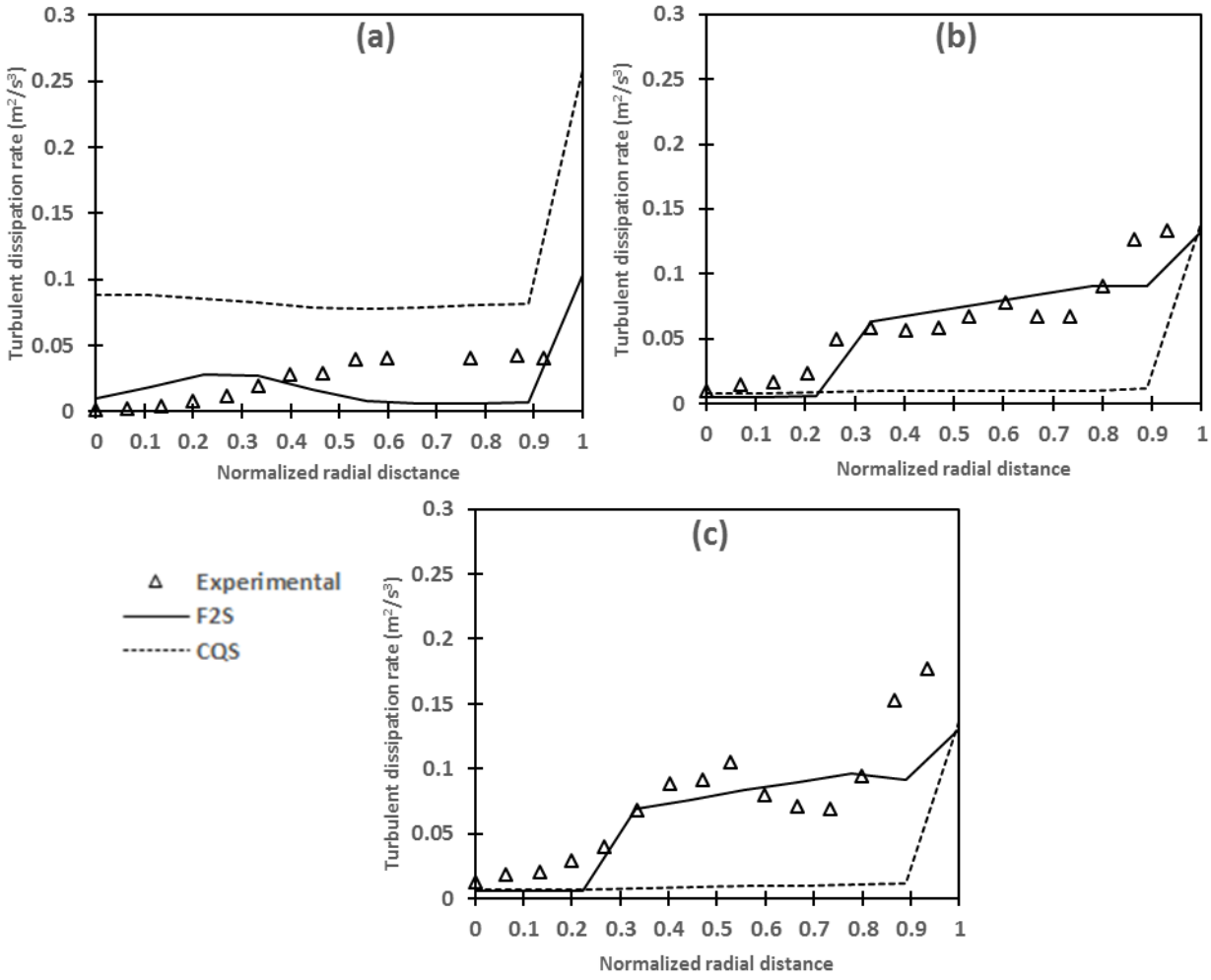


**Figure 4-7.** Comparison between the simulated and experimental turbulent dissipation rate profiles at different axial positions. (a) H/D = 0.2; (b) H/D = 2.6 and (c) H/D = 5.0.

### *4.1.8. Bubble size distribution*

Figure 4-8 shows the effect of superficial gas velocity on the bubble size distribution. It can be seen that the superficial gas velocity significantly affects the bubble size. An increase in the superficial gas velocity (from 8.66 mm/s to 23.10 mm/s) resulted in an increase in the bubble size (from 3 mm to 11 mm). From Figure 4-8d, it can be seen that the bubbles had a spherical cap-like shape that was formed at high superficial gas velocities. The superficial gas velocity range used in the current study was well within the homogeneous regime, although, a superficial gas velocity of 23.10 mm/s gave a bubble size of about 11 mm. Besagni & Inzoli (2016) referred to this characteristic as the psuedo-homogenous regime and they further stated that at this regime, the bubbles entrain the smaller swarm of bubbles through their wake causing the break-up phenomena. This high bubble size obtained at a low superficial gas velocity is as a result of the type of distributor used (sintered plate). According to Li et al. (2009), the bubble size distribution along with the gas hold-up are strongly influenced by the distributor design. Furthermore, these two parameters are used to determine the interficial area between the gas and liquid phases. They further reported that the sintered plate distributor results in high average gas hold-up and bubble sizes as compared to other forms of distributors (pipe and orifice).

Fluidized bed photoreactors often use air mainly for mixing along with other factors. It is therefore necessary to model and understand bubble distribution in a fluidized bed photoreactor. The first few bubbles that enter the reactor through the distributor often determine the formulation of the initial bubble size. As the bubbles travel up the reactor, the initial bubble size range changes due to factors such as vorticity caused by shear flow, varying bubble rise velocities, wake entrainment, size deformation and liquid phase turbulence (Li et al., 2009). The bubble shape deformation, that is usually referred to as bubble break-up or coalescence, is caused by turbulent eddies that result in non-uniform bubble sizes and shapes.

The population balance model (PBM) or Multiple Size Group (MUSIG) model are often used to model and capture the phenomena of bubble break-up and coalescence and bubble size distribution. In the current study, that uses a quantitative approach, the bubble size distribution was experimentally determined at four different superficial gas velocity size ranges (8.66 mms to 23.10 mm/s). It is worth noting that the superficial gas velocity range studied is well within the homogeneous regime, therefore, bubble shape deformation (bubble break-up and coalescence) is insignificant.

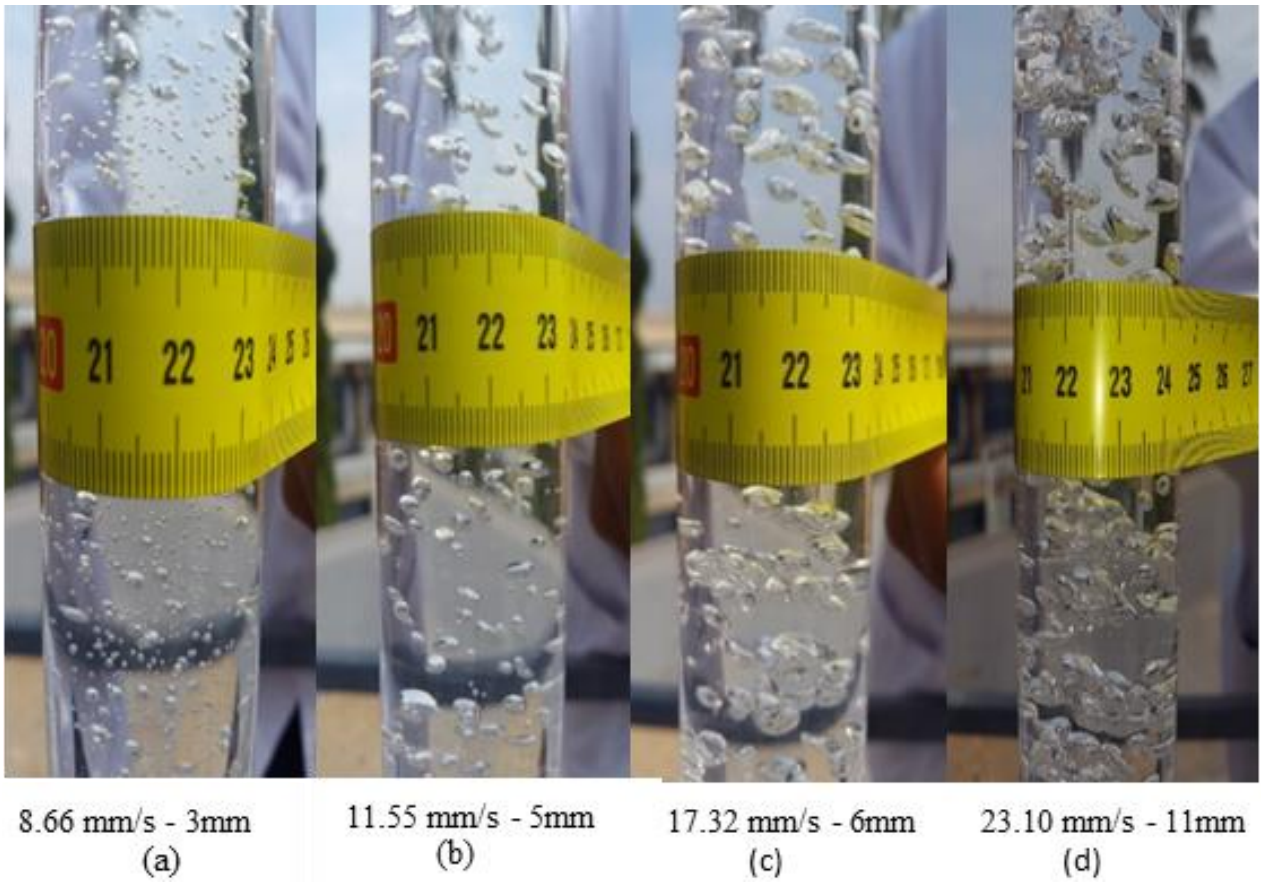


**Figure 4-8.** Effect of superficial gas velocity on the bubble distribution.

### *4.1.9. Effect of superficial gas velocity*

The mathematical model developed in this study predicted the experimental data of Kulkarni et al. (2007) fairly well using the optimized setting methods. To verify the effectiveness of the model, it was further employed to study the effect of superficial gas velocity on the global gas hold-up. The simulation data was compared to the experimental global gas hold-up results determined in the present study. The optimal setting methods, as shown by Table 4-3, were used for all the simulation cases from here onwards.

**Table 4-3.** Optimal setting methods for CFD simulations.

| Parameter | Setting |
|---|---|
| Grid size | 500 000 cells, 1.2mm |
| Discretization scheme | Momentum: 2nd order Upwind<br>Volume fraction: QUICK<br>Turbulence Eqs.: 2nd order Upwind |
| Time step size | 0.001 |

Figure 4-9 shows the effect of superficial gas velocity on the global gas hold-up in the reactor. The simulation data was compared to the experimental results. The simulation data showed a good prediction of the experimental results from a superficial gas velocity of 11.55 mm/s to 17.32 mm/s. The reactor was operated in the homogenous regime based on the superficial gas velocities studied. Literature has shown that within the homogeneous regime, as the bubbles travel to the top surface of the reactor, gas properties such as size, shape and velocity are constant and can be easily specified in the simulation (Pourtousi et al., 2015). It was found that an increase in superficial gas velocity results in an increase in the global gas hold-up. The increase in global gas hold-up is due to an increase in the amount of bubbles present in the reactor. This similar trend was also found by Pourtousi et al. (2015) where they determined the effect of superficial gas velocity on the overall gas hold-up. At a superficial gas velocity of 15 mm/s, they obtained an overall gas hold-up of ~ 0.048, whereas in the current study, a superficial gas velocity of 14.44 mm/s gave a global gas hold-up of 0.052 and 0.050 for experimental and simulation results, respectively. This agreement of the simulation data with the experimental results shows that the developed model is effective.

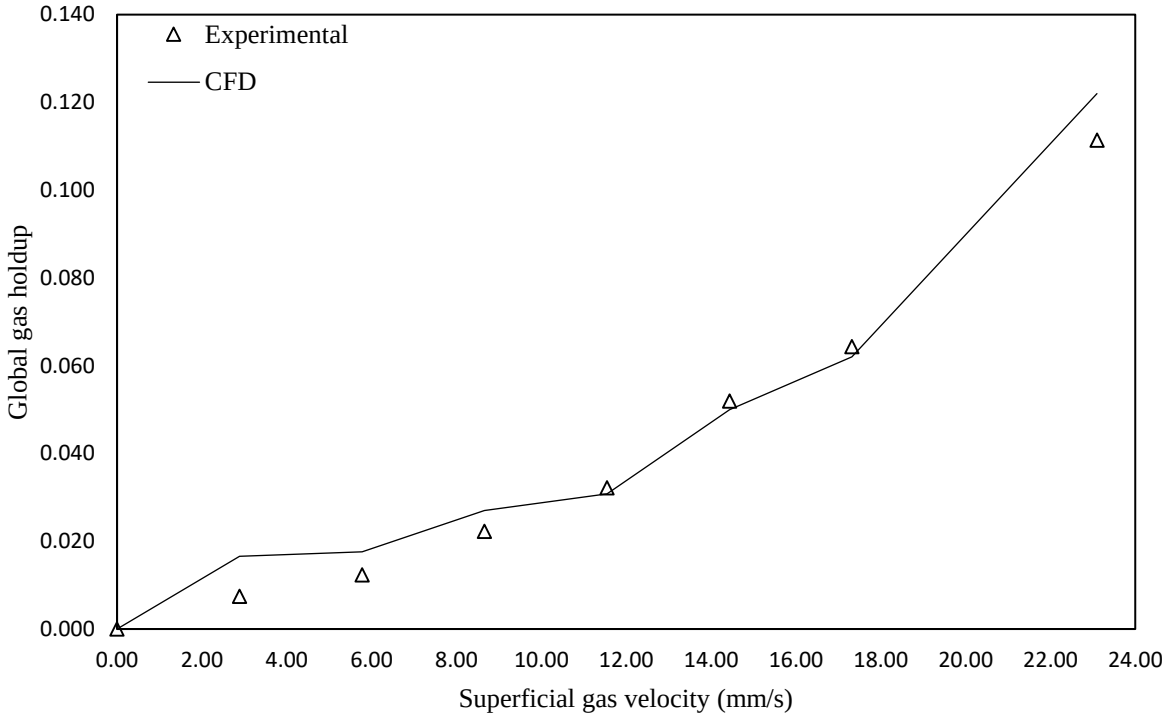


**Figure 4-9.** Effect of superficial gas velocity on the global gas hold-up: comparison between CFD simulation and experimental results.

## 4.2. Photodegradation

### *4.2.1. Model fitting and statistical analysis*

Response surface methodology seeks to find the relationship between the process variables and the response variable. The process variables that predominantly affect the efficiency and performance of the system, were selected based on past experiments. The central composite design was used to determine the collective effects of the process variables on the photodegradation of phenol. The response variable (photodegradation %) for both experimental and predicted along with the combination of the respective process variables is shown in Table 4-4. Based on the experimental response, the maximal degradation of phenol achieved was 65.9%, whereas the minimum degradation obtained was 7.83%. The low degradation efficiency (7.83%) was obtained at 0 g/L catalyst loading. The zero-catalyst loading was investigated to show the presence of a catalyst has an effect on the photodegradation process. The photodegradation efficiency obtained in the current study was relatively low as compared to literature (Shahrezaei et al. 2012b; Zulfakar et al. 2011) and this was due to the bigger particle size used in the current work.

Shahrezaei et al. (2012b) conducted a process modelling and kinetic study on the photodegradation of petroleum wastewater using $TiO_2$ catalyst. The maximal degradation they obtained was 80.84% with a reaction time of 120 min using a nano-sized catalyst (0.1 g/L). Zulfakar et al. (2011) used a nano-sized $TiO_2$ catalyst (0.33 g/L), similar to Shahrezaei et al. (2012b), to photodegrade phenol. The catalyst was immobilized and they achieved a maximal degradation of about 100% with a reaction time of 250 min, whereas in the current study, the maximal degradation (65.9%) was achieved in 180 min, with a particle size range of 300 – 1000 µm and a catalyst loading of 1 g/L. Accordingly, literature studies using $TiO_2$ as a photocatalyst achieve high photodegradation efficiency with nano-sizes whereas, the current study obtained a relatively low photodegradation efficiency at micrometer sizes. This is an indication that an increase in the particle size of the catalyst results in a decrease in the performance of the system. This is due to the fact that an increase in the particle size (from nanometer to micrometer), causes a decrease in the specific surface area and available active sites for adsorption and photodegradation of the pollutants. Thus reducing the efficiency of the process.

**Table 4-4.** Full factorial CCD experimental matrix with experimental and predicted responses.

| Run | *A*: Initial pH level | *B*: Catalyst loading (g/L) | *C*: Reaction time (min) | *D*: Superficial velocity (mm/s) | Degradation (%) | |
|---|---|---|---|---|---|---|
| | | | | | Experimental | Predicted |
| 1 | 3.5 | 1 | 120 | 8.66 | 35.94 | 34.20 |
| 2 | 6.5 | 1 | 120 | 8.66 | 40.52 | 47.28 |
| 3 | 3.5 | 3 | 120 | 8.66 | 53.55 | 43.60 |
| 4 | 6.5 | 3 | 120 | 8.66 | 42.82 | 57.64 |
| 5 | 3.5 | 1 | 240 | 8.66 | 38.13 | 43.99 |
| 6 | 6.5 | 1 | 240 | 8.66 | 54.27 | 54.51 |
| 7 | 3.5 | 3 | 240 | 8.66 | 50.34 | 31.52 |
| 8 | 6.5 | 3 | 240 | 8.66 | 36.15 | 43.00 |
| 9 | 3.5 | 1 | 120 | 17.32 | 51.90 | 41.25 |
| 10 | 6.5 | 1 | 120 | 17.32 | 48.10 | 44.36 |
| 11 | 3.5 | 3 | 120 | 17.32 | 55.57 | 52.78 |
| 12 | 6.5 | 3 | 120 | 17.32 | 56.50 | 56.84 |
| 13 | 3.5 | 1 | 240 | 17.32 | 65.90 | 68.83 |
| 14 | 6.5 | 1 | 240 | 17.32 | 52.92 | 59.07 |
| 15 | 3.5 | 3 | 240 | 17.32 | 58.74 | 48.18 |
| 16 | 6.5 | 3 | 240 | 17.32 | 50.50 | 46.69 |
| 17 | 2 | 2 | 180 | 11.55 | 58.80 | 53.64 |
| 18 | 8 | 2 | 180 | 11.55 | 56.71 | 58.23 |
| 19 | 5 | 0 | 180 | 11.55 | 7.83 | 9.63 |
| 20 | 5 | 4 | 180 | 11.55 | 31.80 | 39.09 |
| 21 | 5 | 2 | 60 | 11.55 | 28.31 | 38.61 |
| 22 | 5 | 2 | 300 | 11.55 | 45.20 | 41.25 |
| 23 | 5 | 2 | 180 | 5.77 | 34.97 | 44.79 |
| 24 | 5 | 2 | 180 | 23.10 | 42.00 | 58.54 |
| 25 | 5 | 2 | 180 | 11.55 | 46.00 | 46.15 |
| 26 | 5 | 2 | 180 | 11.55 | 45.00 | 48.25 |
| 27 | 5 | 2 | 180 | 11.55 | 46.20 | 44.32 |
| 28 | 5 | 2 | 180 | 11.55 | 46.80 | 46.15 |
| 29 | 5 | 2 | 180 | 11.55 | 46.00 | 47.36 |
| 30 | 5 | 2 | 180 | 11.55 | 46.90 | 48.15 |

The two responses, predicted and experimental, were determined through the combination of the process variables as shown in Table 4-4. The predicted values were computed by means of the final second-order empirical model (Equation 62) in terms of coded factors through the use of the Design Expert® Software of Stat-Ease Inc. The predicted values presented a sufficient correlation to the experimental values, although there was a slight deviation in some other experimental runs. The experimental data was fitted to several models (cubic, quadratic and

linear). However, it was found through their subsequent ANOVA that the photodegradation of phenol was best described by the second-order empirical model. From Equation 88, the main effects of initial pH level (*A*) had a significant negative influence on the photodegradation of phenol. This shows that an increase in the initial pH level will result in a decrease in the photodegradation efficiency.

$$y = 46.15 - 4.77\mathrm{A} + 3.60\mathrm{B} + 0.16\mathrm{C} + 1.85\mathrm{D} + 2.95\mathrm{A}^2 - 4.04\mathrm{B}^2 - 0.43\mathrm{C}^2 + 1.88\mathrm{D}^2 - 1.14\mathrm{AB} - 0.52\mathrm{AC} - 1.37\mathrm{AD} + 0.66\mathrm{BC} + 0.66\mathrm{BD} + 0.50\mathrm{CD} \quad (62)$$

In order to evaluate the adequacy of the empirical second-order model, both the ANOVA method and significance test were employed. The significance test was used to determine the regresion coefficients of the empirical second-order model. The ANOVA method was used to evaluate the significance of the empirical second-order model (Jiang et al., 2013), and the results are shown in Table 4-5. The evaluation is done by determining the Probability value (P) and Fisher's test (F) for each regression coeficient in the model. The significance of the interaction between the process variables is determined by the Fisher's test, thereby creating a pattern between the interaction of the process variables (Petrović et al., 2015). This means that, the higher the values of the Fisher's test, the lower the Probability values. Furthermore, the F-values are computed for each tested model and the model with the most significant terms is selected (Fakhri et al., 2016).

From Table 4-5, the F-value for the model was found to be 98.56 resulting in a Probabilty value that is less than 0.0001. This means that the model is suitable for this study (significant). The Probability values were used to specify the interaction strength between the independent variables (Petrović et al., 2015). In addition, model terms that obtain P-values that are less than 0.05 are considered to be statistically significant. As per Table 4-5, the inital pH level (*A*), superficial gas velocity (*D*), quadratic of inital pH level ($A^2$) and interaction of catalyst loading & reaction time (*BC*) and catalyst loading & superficial gas velocity (*CD*) are considered significant model terms. Other model terms are considered to be insignificant and it is recommended to eliminate them so as to simplify the empirical second-order model.

**Table 4-5.** Analysis of variance of the empirical second-order model.

| Source | Sum of Squares | DF | Mean Square | F-Value | Prob > F | |
|---|---|---|---|---|---|---|
| Model | 2099.96 | 14 | 139.59 | 98.56 | <0.0001 | Significant |
| *A* | 267.13 | 1 | 267.13 | 31.65 | 0.0453 | |
| *B* | 0.22 | 1 | 0.22 | 7.17 | 0.2275 | |
| *C* | 14.95 | 1 | 14.95 | 65.36 | 0.0546 | |
| *D* | 371.49 | 1 | 371.49 | 54.63 | 0.0411 | |
| $A^2$ | 249.51 | 1 | 249.51 | 38.14 | 0.0452 | |
| $B^2$ | 161.96 | 1 | 161.96 | 6.78 | 0.2334 | |
| $C^2$ | 134.81 | 1 | 134.81 | 1.59 | 0.0979 | |
| $D^2$ | 35.85 | 1 | 35.85 | 61.44 | 0.0501 | |
| *AB* | 0.92 | 1 | 0.92 | 3.63 | 0.3077 | |
| *AC* | 6.57 | 1 | 6.57 | 7.15 | 0.2278 | |
| *AD* | 106.83 | 1 | 106.83 | 10.14 | 0.1937 | |
| *BC* | 478.19 | 1 | 478.19 | 24.29 | 0.0212 | |
| *BD* | 11.74 | 1 | 11.74 | 9.09 | 0.2039 | |
| *CD* | 25.21 | 1 | 25.21 | 1.68 | 0.4182 | |
| Residual | 381.84 | 15 | 72.12 | - | - | |
| *Lack of Fit* | 354.85 | 10 | 35.92 | 9.54 | 0.1084 | Not significant |
| *Pure Error* | 26.99 | 5 | 5.4 | - | - | |
| Cor Total | 2481.8 | 29 | | | | |

The presence of systematic errors in the model is detected by means of residual analysis. Two factors that often contibute to the residual variance are: pure experimental error and lack of fit. The pure error is computed by considering the difference between the eperimental and predicted values under the same conditions in a random sequence (Petrović et al., 2015). The variations in the model terms are represented by the lack of fit. The P-value for lack of fit was found to be 0.1084 indicating that it was statistically insignificant. The coefficient of determination ($R^2$) in the current study was found to be 0.975. This signifies that 97.5% of the variation was found in the response variable can be described by the model, whereas, 2.5% is residual variability (Islam et al., 2009). Furthermore, the adjusted coefficient of determination ($R^2_{adj}$) was found to be acceptable (0.954), indicating the significance of the model. It is worth noting that Equation 88 is highly significant (P-value < 0.0001), with an acceptable coefficient of determination ($R^2 = 0.954$) and is therefore adequate to predict the photodegradation of phenol.

### *4.2.1. 3D response surface analysis*

Figure 4-10 shows the effect of initial pH level and reaction time on the degradation of phenol. A decrease in the initial pH level resulted in an increase in the photodegradation of phenol. The Zeta potential of Titanium dioxide is 3 mV as investigated by Liao et al. (2009). The influence of initial pH on the photodegradation efficiency can be described by the point of zero charge (pzc), whereby, this value was reported to be 6.2 for $TiO_2$ (Shahrezaei et al., 2012b). This suggests that the surface of $TiO_2$ is negatively charged in alkaline solutions (pH > 6.2) and, conversely, it is positively charged in acidic conditions (pH < 6.2). This was also confirmed by the empirical second-order model where the initial pH level had a negative regression coefficient (-4.77*A*). This suggests that a high initial pH level has a negative influence on the photodegradation of phenol.

Since phenol and its derivatives are negatively charged in aqueous solution due to the OH groups (Shahrezaei et al., 2012b), it is therefore expected that their electrostatic attraction to the catalyst particles will be more favourable in acidic conditions and repulsive in alkaline conditions. Furthermore, the negatively charged anions are adsorbed into the pores (pore diffusion) of the catalyst as mentioned in *Section 2.5*. The initial pH results revealed that the photodegradation of phenol is favourable in acidic condition as opposed to alkaline conditions. From the current study, at these acidic conditions (pH = 3.5), the maximal photodegradation efficiency of phenol was found to be 52.2%. Saien & Nejati (2007) studied the photodegradation of petroleum wastewater (phenol) using a nano-sized $TiO_2$ photocatalyst and they obtained a maximal photodegradation of 70% at a pH level of 3 and reaction time of 120 min.

It is illustrated in Figure 4-10 that an increase in the reaction time from 120 min to 210 min resulted in an increase in the photodegradation of phenol from 39.9% to 52.8%, whereas, the photodegradation of phenol remained constant with a further increase in the reaction time beyond 210 min. When the process reached a reaction time of 210 min, this implies that the active surfaces on the catalyst are fully occupied and the process has reached equilibrium.

The interaction between the process variables can be better understood by plotting three-dimensional response surface plots and these are discussed in detail in this section. These surface plots are graphical demonstrations of the developed empirical second-order model (Equation 78). They assist in analyzing the interaction among the process variables (Fakhri et al., 2016) and to determine the optimal level for each process variable for the degradation of

phenol. In addition, there exist an infinite number of combinations for any two tested process variables, therefore, these plots reveal the type of interactions between these variables (Petrović et al., 2015).

Literature has shown that petroleum wastewater contains various organic compounds (Coelho et al., 2006) and, quite often, these organic pollutants differ greatly when it comes to solubility in water, speciation behaviour and hydrophobicity (Shahrezaei et al., 2012b). In addition, some of these pollutants can occur in negative, neutral or positive forms in solution and these discrepancies in ionic behaviour can significantly affect the photodegradation efficiency of the process. Consequently, the initial pH level of the solution plays a major role in the photodegradation efficiency of the system.

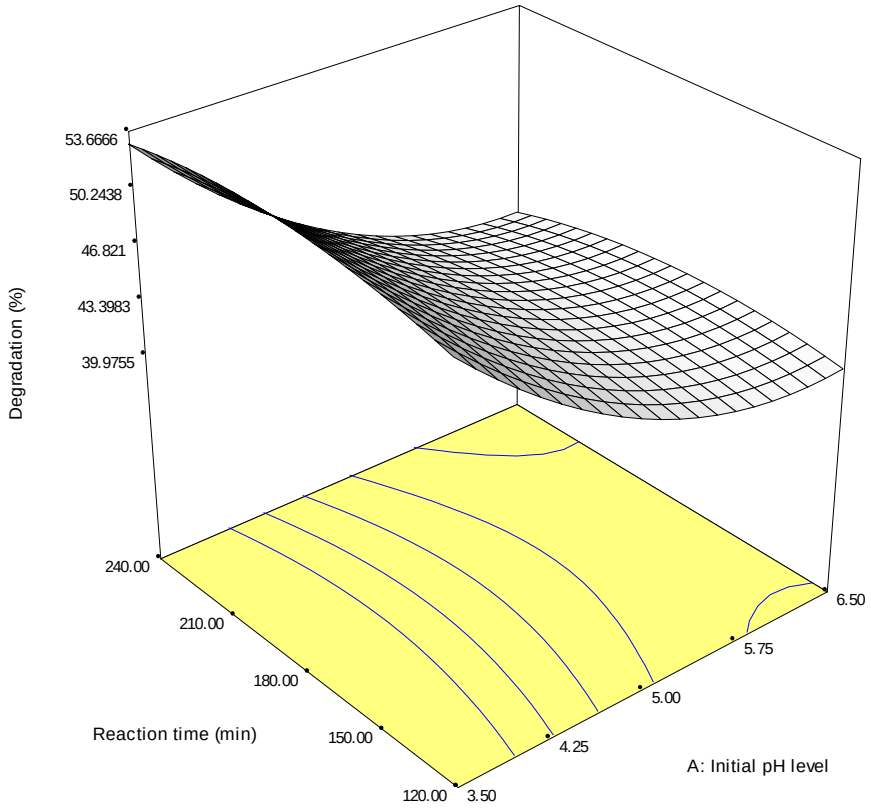


**Figure 4-10.** Effect of reaction time and initial pH level on the photodegradation of phenol.

Figure 4-11 shows the effect of catalyst loading and initial pH level on the photodegradation of phenol. Since a composite catalyst was used, the values displayed here (1.0-3.0 g/L) were those of the composite catalyst as a whole. The catalyst dosage range chosen in this study was based on preliminary experiments that have shown that an increase in the $TiO_2$ particle size necessitates an increase in catalyst dosage. The results, from Figure 4-11, show that an increase in the catalyst loading, from 1.0 to 2.0 g/L, results in an increase in the photodegradation of phenol. This is due to an increase in the number of active sites available for adsorption and photodegradation of phenol. However, a further increase beyond 2.0 g/L results in a decrease in the photodegradation efficiency. Therefore, the optimal catalyst loading in the current study was chosen to be 2.0 g/L that gave a photodegradation efficiency of 47.3%.

The catalyst loading is an important process variable that affects photodegradation efficiency of organic pollutants in a fluidized bed photoreactor. It has been found that in photocatalytic systems, a high catalyst loading is ineffective due to excess catalyst particles preventing the UV light penetration thus resulting in the reduction of photodegradation efficiency. Therefore, an optimal catalyst loading is necessary to avoid the hindering of UV light penetration. It is also good practice to ensure good economic usage of the catalyst to reduce the cost of catalyst loading (Zulfakar et al., 2011).

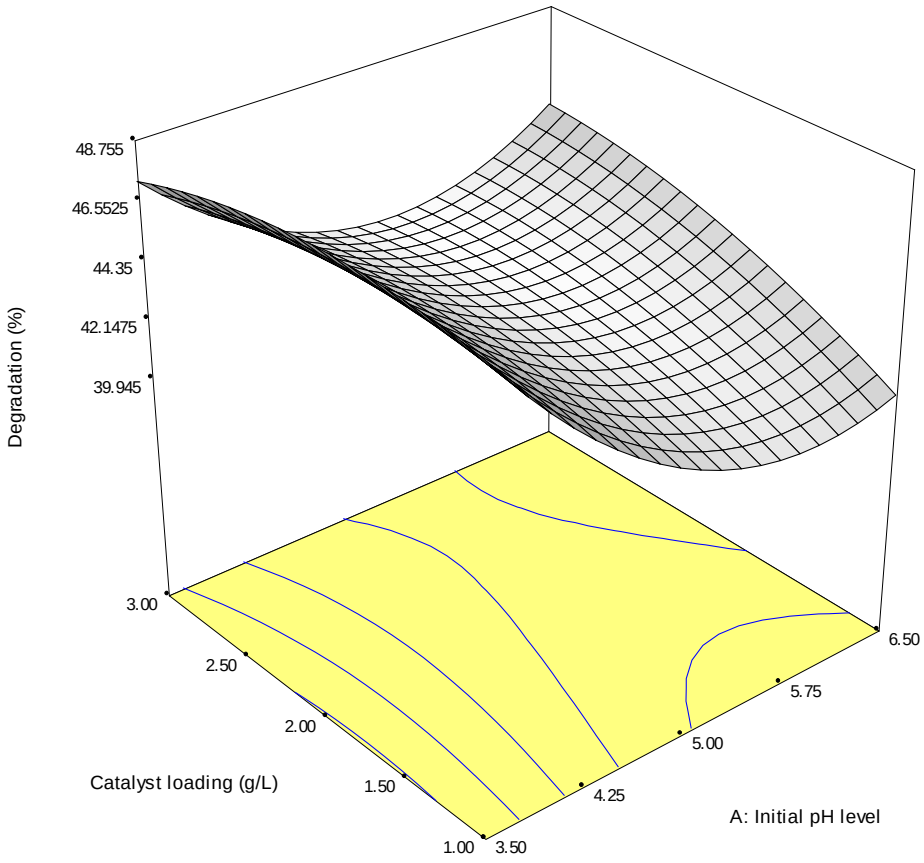


**Figure 4-11.** Effect of catalyst loading and initial pH level on the photodegradation of phenol.

Figure 4-12 shows the effect of superficial gas velocity and catalyst loading on the photodegradation of phenol. The results show that an increase in the superficial gas velocity results in an increase in the photodegradation efficiency. The optimal superficial gas velocity was found to be 17.32 mm/s that gave a maximal photodegradation efficiency of 48.6% with a catalyst loading of 2.0 g/L. The superficial gas velocity was varied within the homogeneous regime (8.66-17.32 mm/s). According to the hydrodynamic study, the bubble size distribution was uniform and the global gas hold-up was below 0.13 (Figure 4-8). An increase in the superficial gas velocity results in an increase in the number of bubbles present in solution due to an increase in the drag force, thus increasing the global gas hold-up. This increase in the global gas hold-up results in an increase in the availability of oxygen (to prevent electron-hole recombination) and enhances the mixing inside the reactor.

The central idea of a fluidized bed photoreactor is that fluidization and air was used in the current study for fluidization (and agitation). The use of air is important due to the fact that it plays two major roles in photodegradation: mixing inside the reactor and the oxygen acts as an

electron scavenger that prevents electron-hole recombination. The mixing inside the reactor (hydrodynamics) has been discussed in *Section 4.1* and it was shown that the gas hold-up assists in understanding the mixing in the reactor. It was also shown that the superficial gas velocity has a significant impact on the global gas hold-up.

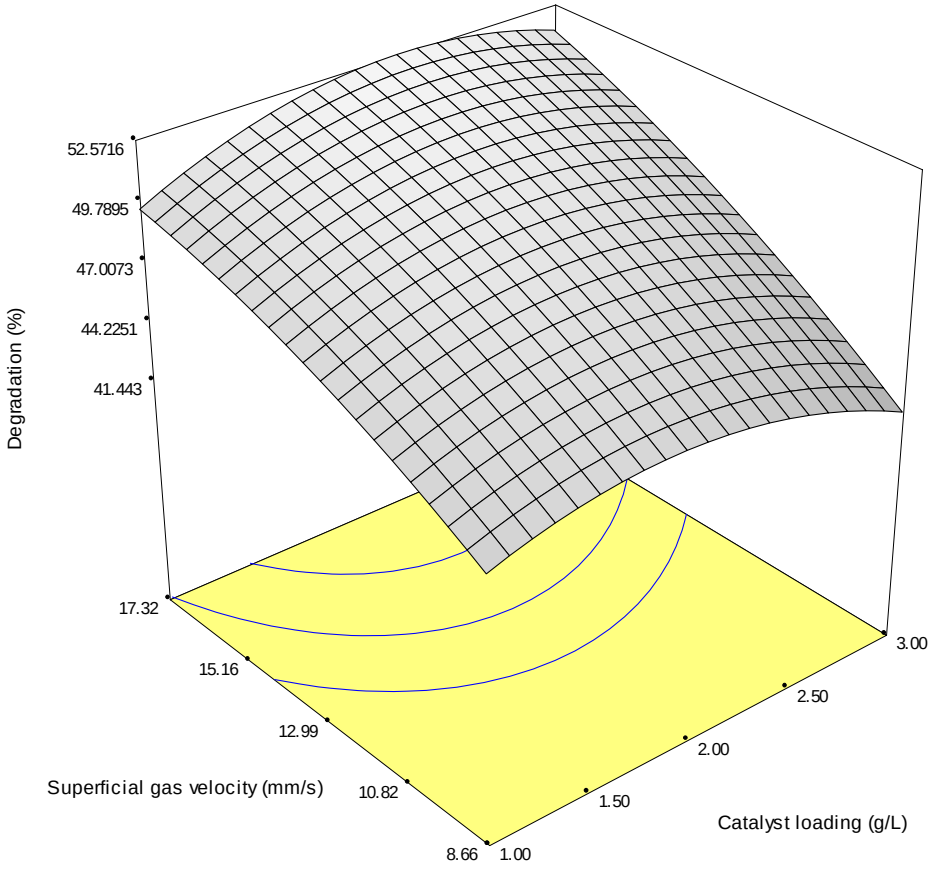


**Figure 4-12.** Effect of superficial gas velocity and catalyst loading on the photodegradation of phenol.

## 4.3. Reaction kinetics

In the current study, the adsorption reaction constant ($b$) was found to be insignificant, consequently, the term in the denominator of Equation 24 (L-H model) was neglected ($bC \sim 0$). Equation 24 was then transformed into a linearized algebraic equation (Equation 26) where the apparent reaction rate constant ($K_{app}$) was determined by using the gradient of the slope and $t$ is the reaction time in minutes. The apparent reaction rate encapsulates both the degradation reaction rate ($k_r$) and the adsorption reaction rate constants ($b$), and it was assumed that $b$ is negligible, compared to $k_r$, and the assumption was confirmed by conducting adsorption experiments. The adsorption experiments were conducted at optimal conditions to evaluate the

composite catalyst's adsorption capacity. The initial concentration of phenol for the adsorption study was 30 ppm and after 75 min, only 7.33% of phenol was adsorbed. Therefore, it is evident that the rate of adsorption was minimal.

The photodegradation kinetics of phenol under solar irradiation and $TiO_2$ catalyst were studied. The kinetic experiments were conducted using the optimal photodegradation operating conditions that were found, using RSM, to be: superficial gas velocity of 17.32 mm/s, catalyst loading of 1.0 g/L, initial pH level of 3.5 and reaction time being 210 min. An initial concentration of 30 ppm (for phenol) was used for all reaction kinetic experiments and sampling was done at different time intervals. The reaction rate data was modelled using both the first-order (L-H model) and second-order kinetics by measuring the concentration of phenol at different time intervals. From the slope of the graph in Figure 4-13a, the apparent reaction rate constant was found to be 0.0046 $min^{-1}$ that is within the range of what Shahrezaei et al. (2012b) obtained to be 0.007-0.013 $min^{-1}$.

The coefficient of determination ($R^2$) was found to be 0.9931. A high value of $R^2$ evidently shows that the L-H model was applied with a good degree of precision. In addition, the $R^2$ obtained in this study was similar to that found by Shahrezaei et al. (2012b) ($R^2 > 0.997$). This means that it can be used to predict future outcomes. The second order model was applied onto the reaction rate data and gave a relatively low value for $R^2 = 0.9698$ and $K_{ap} = 0.0002$ L/(mg.min)$^{-1}$ (Figure 4-13b). Apollo et al. (2014) studied the photodegradation kinetics of phenol and methyl orange using solar irradiation and ZnO catalyst supported on silica. Although they did not use the L-H model, they showed that the degradation kinetics of phenol using ZnO-$SiO_2$ catalyst followed the pseudo first-order kinetics. At an initial concentration of 30 ppm (phenol), they obtained a photodegradation reaction rate constant of 0.0107 and $R^2$ being 0.9941.

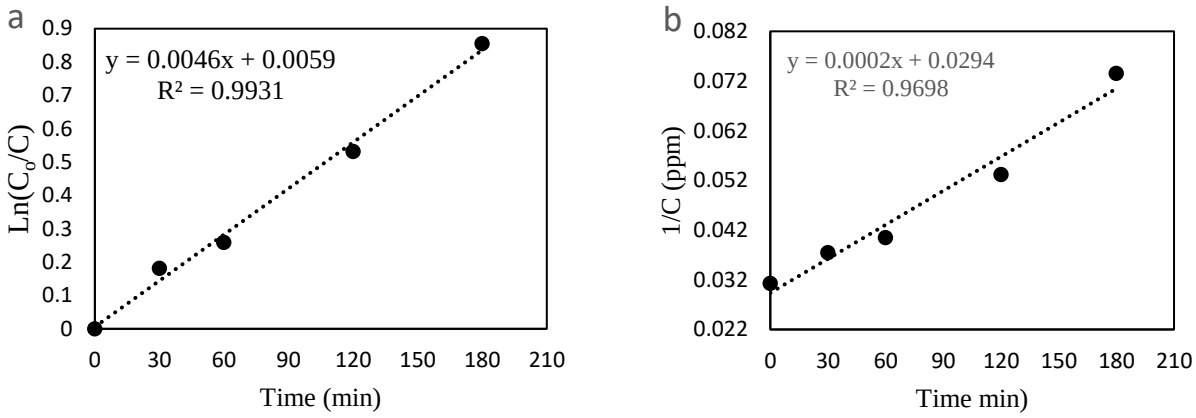


**Figure 4-13.** Linear fit for photodegradation reaction. a) L-H (first-order) model b) Second-order model.

From understanding the photodegradation kinetics of phenol under optimal conditions, further experiments were conducted to monitor the reduction of TOC using the optimal conditions. Figure 4-14 shows the effect of the optimal conditions on the reduction of TOC at different time intervals. After 210 min of irradiation, only 63.7% of TOC reduction was achieved. From the RSM results, it was shown that 52.7%, that was the concentration of phenol, was degraded in 150 min. Therefore, it is evident that beyond 150 min, there was still some intermediates present in solution. Zulfakar et al. (2011) investigated the photodegradation of phenol using immobilized $TiO_2$ photocatalyst and UV light. They reported that the main intermediates formed during the degradation of phenol are p-benzoquinone, catechol, hydroquinone and resorcinol. They further mentioned that these intermediates tend to compete with phenol for the available active sites on the catalyst thus resulting in a decrease in the apparent reaction rate constant. In addition, the formation of intermediates is highly dependent on the initial concentration of phenol.

It has been reported that as the hydroxyl radicals destroy phenol, it is converted into its derivatives (intermediates) and those derivatives are further converted into $H_2O$, $CO_2$ and weak acids (Shahrezaei et al., 2012b). Furthermore, literature shows that the intermediates significantly affect the apparent reaction rate constant (Zulfakar et al., 2011). Therefore, it is necessary to understand the reaction chain by monitoring the TOC reduction during the photocatalytic degradation of phenol. Total organic carbon has the ability to indirectly reveal the degradation of both phenol and phenolic derivatives (intermediates).

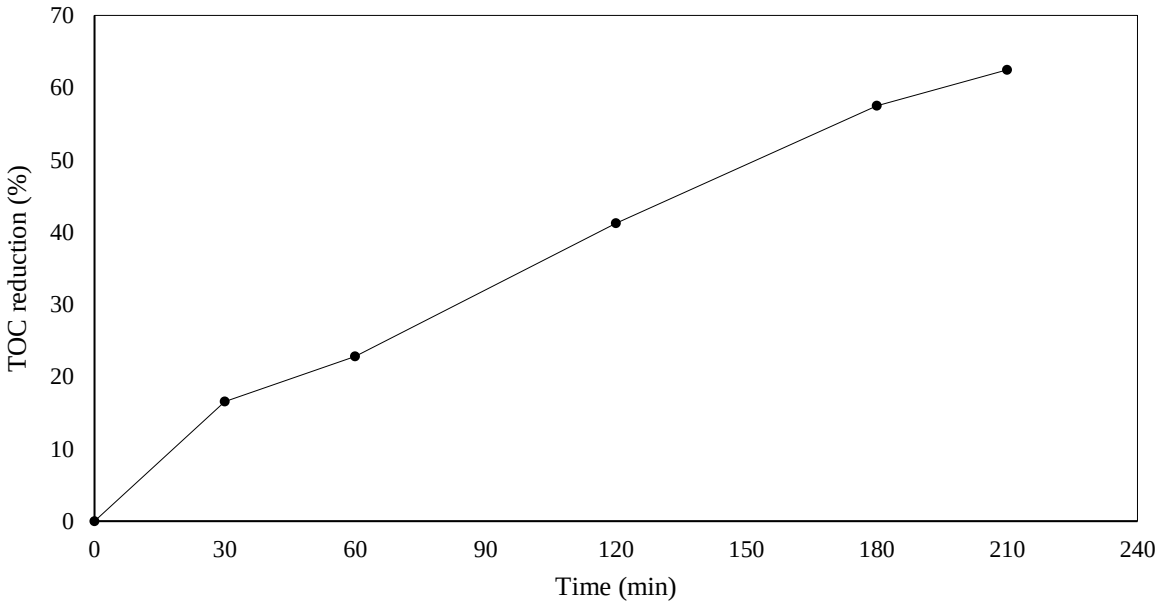


**Figure 4-14.** Reduction of TOC at different time intervals.

## 4.4. Sedimentation tests

Figure 4-15 shows the colloidal stability of titanium dioxide at different particle sizes, where, turbidity of the suspensions was monitored at different time intervals. The nano-sized particles had a sluggish decrease in turbidity from 888 to 458 NTU, whereas, the micro-sized particles showed a sharp decrease in turbidity from 0 to 10 min and remained constant from 70 min at around 84 NTU. It is worth noting that performance of a solid-liquid sedimentation process is significantly affected by electrolyte concentration and pH of solution (Fernández-Ibáñez et al., 2003). Therefore, to rule out these effects, the sedimentation tests were carried out at a neutral pH and using de-ionized water. After 100 min of sedimentation, the nano-size achieved a turbidity reduction of 48.4%, whereas, the micro-size achieved 83.7%.

As mentioned in *Section 1.3*, $TiO_2$ is nano-sized (powder form) meaning that it has a large specific surface area for adsorption and photodegradation but the limiting factor is filtering it out of solution. The reason for attaching $TiO_2$ onto silica was to increase the particle size thereby enabling a much easier filtration process. Several studies such as Xi & Geissen, (2001) have attempted the separation of titanium dioxide from aqueous solution by using cross-flow microfiltration (CFM) to improve the overall process of solar photocatalysis. Although the results from this study were encouraging, at commercial level, microfiltration and membrane maintenance will significantly increase the operating costs (Fernández-Ibáñez et al., 2003). If

solar photodegradation is to be as competitive as its competitors, it requires a low cost and robust separation technique (sedimentation). The sedimentation tests were conducted by investigating the colloidal stability through experimental suspensions.

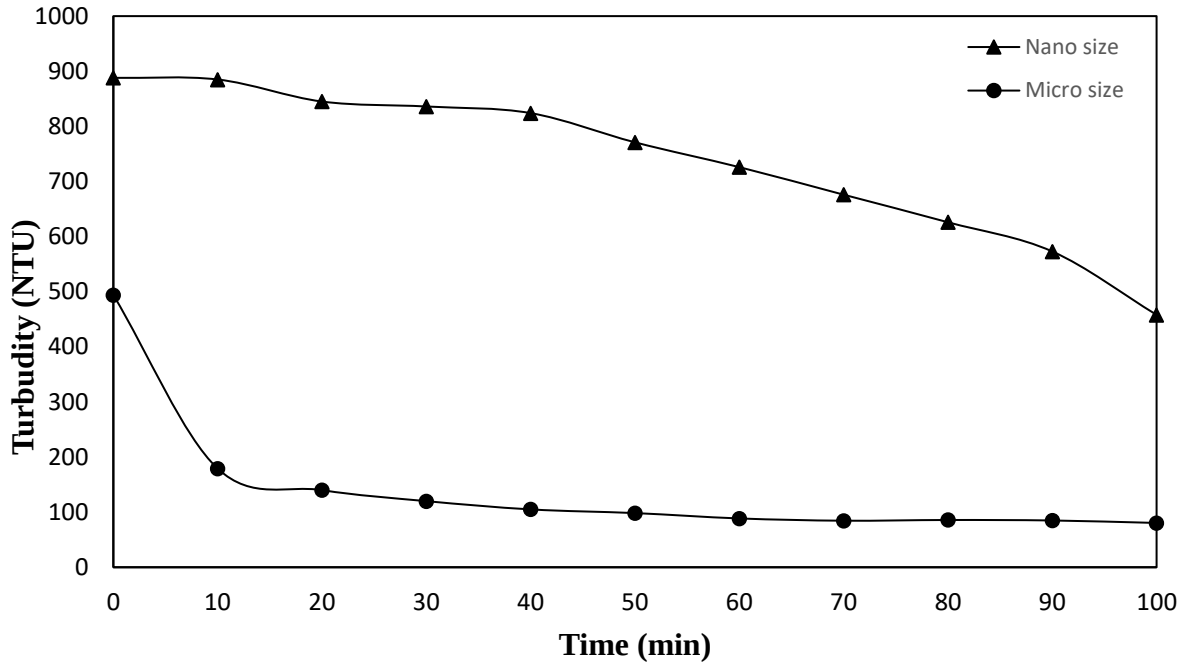


**Figure 4-15.** Effect of turbidity during the sedimentation process.

The composite catalyst in the current study achieved a low photodegradation performance (63.7% removal) but its ability to be filtered has been enhanced and this can be seen by the sedimentation experiments. The experiment involved comparing $TiO_2$ catalyst at different particle sizes (nanometer and micrometer). Figure 4-16a and b show the different particle sizes at time t = 0 and Figure 4-16c and d were the different particle sizes after 24 hours of sedimenting. Figure 4-16c (micrometer) showed a rapid settling rate whilst Figure 4-16d (nanometer) was extremely slow. It is therefore evident from the sedimentation experiments that increasing the particle size of $TiO_2$ significantly reduces the cost of filtration at an expense of low process performance. Therefore, one must find an optimal balance between the cost of filtration and process efficiency.

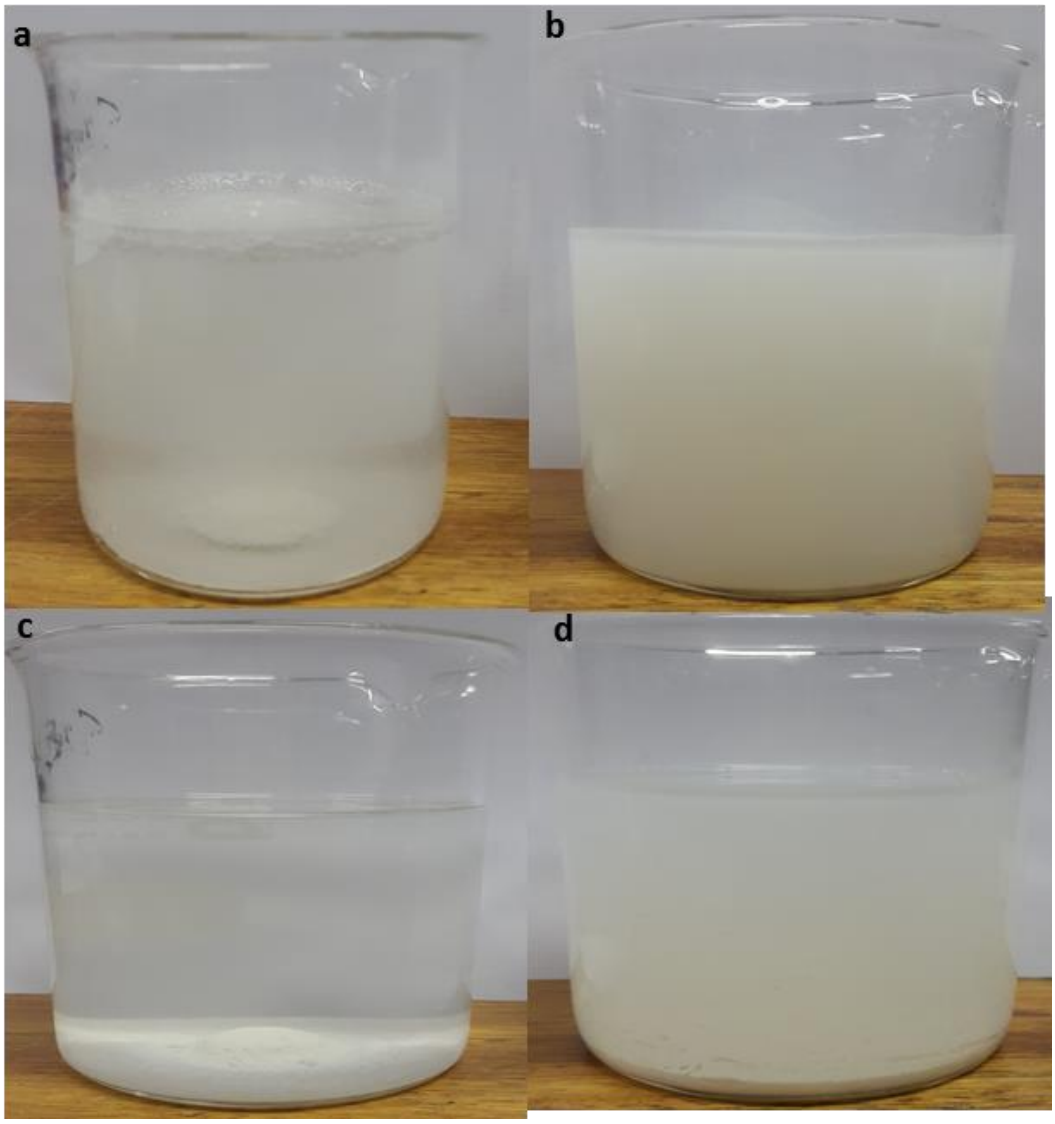


**Figure 4-16.** Comparison of settling rate for $TiO_2$ catalyst at different sizes (nanometer and micrometer). (a) Micrometer size at time t = 0, (b) Nanometer size at time t = 0, (c) Micrometer size at time t = 24 h, (d) Nanometer size at time t = 24 h.

# CHAPTER 5

## 5. Conclusion and recommendations

### 5.1. Conclusion

The purpose of this study was to use CFD techniques to investigate the flow dynamics and turbulence inside the fluidized bed photoreactor. Furthermore, response surface modelling was applied to optimize the operating conditions for the photocatalytic degradation of petroleum wastewater. The petroleum wastewater was simulated by synthesizing a stock solution consisting of phenol that is an organic compound that is mostly found in petroleum wastewater. The concentration of phenol in the stock solution was 30 ppm and was degraded using solar irradiation.

The CFD model was developed by investigating the hydrodynamic conditions such as axial liquid velocity, radial gas hold-up profiles, turbulent kinetic energy and turbulent kinetic dissipation rate. The numerical optimization technique (Desirability) was applied to determine the optimal CFD model settings. The developed model was validated by comparing simulated hydrodynamic data with experimental results (conducted by the author). The grid independence study revealed that the finer the grid size, with structured cells, the better the accuracy of the simulation data. The numerical optimization study showed that to obtain good convergence and accuracy, the following simulation setting methods should be used: grid resolution of 500 000 cells, 2nd order discretization scheme and a small (0.001) time step size. The flow pattern inside the reactor revealed that the bubbles to gather at the centre of the reactor thus inducing a high velocity profile towards the centre of the reactor. The experimental bubble distribution study showed that the bubbles had a spherical-like shape due to low superficial gas velocity and the homogeneous regime. The CFD data showed a good agreement with the experimental CFD data from Kulkarni et al. (2007) and a thorough analysis of the hydrodynamic conditions gave understanding of the flow pattern and turbulence inside the reactor.

Photocatalytic degradation has shown to be a potential wastewater treatment process. The process variables, which predominantly affect the efficiency and performance of petroleum wastewater degradation were optimized using response surface modelling. The photodegradation efficiency in the current study was found to be relatively low (65.9%) as compared to literature (80.84%) and this was attributed to the increase in catalyst particle size

(from nanometer to micrometer). The optimal operating conditions were determined, using RSM, to be: superficial gas velocity of 17.32 mm/s, composite catalyst loading of 2.0 g/L, initial pH level of 3.5 and reaction time being 210 min. The developed second-order empirical model presented a sufficient correlation to the photodegradation experimental data values, although there was a slight deviation in some other experimental runs.

The reaction kinetics for the photocatalytic degradation of petroleum wastewater (phenol) were evaluated using the L-H model and it was found that the photocatalytic degradation of petroleum wastewater follows pseudo first-order reaction kinetics. Fitting the linear curve on the reaction data gave a high coefficient of determination ($R^2 = 0.9931$) that was comparable to literature. The TOC photodegradation data (Figure 4-14) showed a removal efficiency of 63.7% that was low when compared to literature and this was caused by the reduction in the composite catalyst specific surface area and restricting the experiments to reach equilibrium.

There is a misalignment between the photodegradation efficiency and cost of catalyst separation post-treatment. Conventionally, $TiO_2$ is used in its nano-sized form. This method produces excellent photodegradation efficiency. However, the nano-size increases the cost of separation post-treatment. Therefore, binding the catalyst by using silica reduces the photodegradation efficiency but improves the separation process and this was shown by the sedimentation experiments. In the current study, the catalyst particle size was increased from nano-to-microsize thus resulting in a low photodegradation efficiency at decreased cost of separation. It is therefore evident from the sedimentation experiments that increasing the particle size of $TiO_2$ significantly reduces the cost of filtration at the expense of low process performance. Therefore, one must find an optimal balance between the cost of filtration and process efficiency.

## 5.2. Recommendations

The CFD model that was developed in this study showed good correlation to experimental results. It is therefore recommended to further apply the model to study other phenomena such as solid concentration distribution, mass transfer and light distribution in a fluidized bed photoreactor. A study on the effect of catalyst particle size on the photodegradation performance should be conducted to obtain the optimal particle size. This will assist in obtaining a balance between the catalyst particle size and photodegradation performance. Furthermore, improvements of the sedimentation technique needs to be studied by

investigating variables such as effect of pH level of solution, flocculants and electrolyte concentration on the sedimentation efficiency.

# REFERENCES


ABHANG, R.M., KUMAR, D. & TARALKAR, S. V. (2011). Design of Photocatalytic Reactor for Degradation of Phenol in Wastewater. *International Journal of Chemical Engineering and Applications*. 2(5). p. 3144–3148.

ANSYS, (2010). *ANSYS FLUENT Theory Guide*. p.80.

ANSYS, (2011). *ANSYS Meshing User ' s Guide*. p. 1–522.

ANTAL, S. P. , LAHEY, R.T., & FLAHERTY, J.E. (1991). Analysis of phase distribution in fully developed laminar bubbly two-phase flow. *International Journal of Multiphase Flow*. 17(5). p. 635–652.

APOLLO, S., MOYO, S., MABUOA, G. & AOYI, O. (2014). Solar Photodegradation of Methyl Orange and Phenol Using Silica Supported ZnO Catalyst. *International Journal of Innovation, Management and Technology*. 5(3). p. 5–8.

ARAUJO, P.W. & BRERETON, G. (1996). Experimental design. I. Screening. TrAC - *Trends in Analytical Chemistry*, 15(1). p. 26–31.

BECHAMBI, O., SAYADI, S. & NAJJAR, W. (2015). Photocatalytic degradation of bisphenol A in the presence of C-doped ZnO: Effect of operational parameters and photodegradation mechanism. *Journal of Industrial and Engineering Chemistry*. 32. p. 201–210.

BESAGNI, G. & INZOLI, F. (2016). Bubble size distributions and shapes in annular gap bubble column. *Experimental Thermal and Fluid Science*. 74. p. 27–48.

BEZERRA, M.A., SANTELLI., R.E., OLIVEIRA, E. , VILLAR, L.S. & ESCALEIRA, L.A. (2008). Response surface methodology (RSM) as a tool for optimization in analytical chemistry. *Talanta*. 76(5). p. 965–977.

BOX, G.E. & WILSON, K.B. (1951). ON THE EXPERIMENTAL ATTAINMENT OF OPTIMAL CONDITIONS. *Journal of the Royal Statistical Society*. 13(1). p. 1–45.

BOYJOO, Y., ANG, M. & PAREEK, V. (2014). CFD simulation of a pilot scale slurry photocatalytic reactor and design of multiple-lamp reactors. Chemical Engineering Science. 111. p. 266–277.

BOYJOO, Y., ANG, M. & PAREEK, V. (2013). Some aspects of photocatalytic reactor modeling using computational fluid dynamics. *Chemical Engineering Science*. 101. p. 764–784.

BURNS, A.D., FRANK, T., HAMILL, I. & SHI, J. (2004). The Favre Averaged Drag Model for Turbulent Dispersion in Eulerian Multi-Phase Flows. (392). p. 1–17.

CALLAO, M.P. (2014). Multivariate experimental design in environmental analysis. TrAC - *Trends in Analytical Chemistry*. 62. p. 86–92.

CHENG, Z., QUAN, X., XIANG, J., HUANG, Y. & XU, Y. (2012). Photocatalytic degradation of bisphenol A using an integrated system of a new gas-liquid-solid circulating fluidized bed reactor and micrometer Gd-doped TiO2 particles. *Journal of Environmental Sciences* (China). 24(7). p. 1317–1326.

CLOETE, S., JOHANSEN, S.T. & AMINI, S. (2014). Grid independence behaviour of fluidized bed reactor simulations using the Two Fluid Model: Effect of particle size. *Powder Technology*. 269. p. 153–165.

COELHO, A., CASTRO, A.V., DEZOTTI, M. & SANT'ANNA, G.L. (2006). Treatment of petroleum refinery sourwater by advanced oxidation processes. *Journal of Hazardous Materials*. 137(1). p. 178–184.

COLMENARES, J.C., LUQUE, R., CAMPELO, J.M., COLMENARES, F., KARPIŃSKI, Z. & ROMERO, A.A. (2009). Nanostructured photocatalysts and their applications in the photocatalytic transformation of lignocellulosic biomass: An overview. *Materials*. 2(4). p. 2228–2258.

DOLD, P.L. (1989). Curent practice for teatment of petrroleum refinery wastewater and toxics removal. *Water Pollution Research Journal of Canda*. 34(3).

ELLENBERGER, J. & KRISHNA, R. (2003). Shaken, not stirred, bubble column reactors: Enhancement of mass transfer by vibration excitement. *Chemical Engineering Science*. 58(3–6). p. 705–710.

FAKHRI, A., RASHIDI, S., TYAGI, I., AGARWAL, S. & GUPTA, V.K. (2016). Photodegradation of Erythromycin antibiotic by γ-Fe2O3/SiO2 nanocomposite: Response

surface methodology modeling and optimization. *Journal of Molecular Liquids*. 214. p. 378–383.

FERNÁNDEZ-IBÁÑEZ, P., BLANCO, J., MALATO, S. & DE LAS NIEVES, F.J. (2003). Application of the colloidal stability of TiO2 particles for recovery and reuse in solar photocatalysis. *Water Research*. 37(13). p. 3180–3188.

GERMANO, M., PIOMELLI, U., MOIN, P. & CABOT, W.H. (1991). A dynamic subgrid-scale eddy viscosity model. *Physics of Fluids A: Fluid Dynamics*. 3. p. 1760–1765.

GRACE, J.R., CLIFT, R. & WEBER, M.E. (1985). Bubbles, Drops and Paticles, Journal of Fluid Mechanics. 94(4). p. 350–375.

HAQUE, M.M., BAHNEMANN, D. & MUNEER, M. (2012). Photocatalytic Degradation of Organic Pollutants : Mechanisms and Kinetics. Organic Pollutants Ten Years After the Stockholm Convention - *Environmental and Analytical Update*. 3. p. 294–326.

HILL, W.J. & HUNTER, W.G. (1966). A Review of Response Surface Methodology: A Literature Review. *Technometrics*. 8(4). p. 571–590.

ISLAM, M.A., SAKKAS, V. & ALBANIS, T.A. (2009). Application of statistical design of experiment with desirability function for the removal of organophosphorus pesticide from aqueous solution by low-cost material. *Journal of Hazardous Materials*. 170(1). p. 230–238.

JIANG, W., JOENS, J.A., DIONYSIOU, D.D. & O'SHEA, K.E. (2013). Optimization of photocatalytic performance of TiO2 coated glass microspheres using response surface methodology and the application for degradation of dimethyl phthalate. *Journal of Photochemistry and Photobiology A: Chemistry*. 262. p. 7–13.

KHAING, T.H., LI, J., LI, Y., WAI, N. & WONG, F. (2010). Feasibility study on petrochemical wastewater treatment and reuse using a novel submerged membrane distillation bioreactor. *Separation and Purification Technology*. 74. p. 138–143.

KHUNE, M., AKACH, J. & OCHIENG, A. (2014). Solar Photodegradation of Phenol using a Composite Catalyst of Silica and TiO 2. *International Conference on Chemical Engineering & Advanced Computational TEchnologies*. 24–25. p. 2–5.

KIM PHUONG, N.T., BEAK, M-W., HUY, B.T. & LEE, Y.-I. (2016). Adsorption and photodegradation kinetics of herbicide 2,4,5-trichlorophenoxyacetic acid with MgFeTi layered double hydroxides. *Chemosphere*. 146. p. 51–59.

KREPPER, E., LUCAS, D. & PRASSER, H.M. (2005). On the modelling of bubbly flow in vertical pipes. *Nuclear Engineering and Design*. 235(5). p. 597–611.

KULKARNI, A.A., EKAMBARA, K. & JOSHI, J.B. (2007). On the development of flow pattern in a bubble column reactor: Experiments and CFD. *Chemical Engineering Science*. 62(4). p. 1049–1072.

LABORDE-BOUTET, C., LARACHI, F., DROMARD, N., DELSART, O. & SCHWEICH, D. (2009). CFD simulation of bubble column flows: Investigations on turbulence models in RANS approach. *Chemical Engineering Science*. 64(21). p. 4399–4413.

LEE, K., KU, H. & PAK, D. (2016). OH radical generation in a photocatalytic reactor using TiO2 nanotube plates. Chemosphere, 149. p. 114–120.

LI, G., YANG, X. & DAI, G. (2009). CFD simulation of effects of the configuration of gas distributors on gas-liquid flow and mixing in a bubble column. *Chemical Engineering Science*. 64(24). p. 5104–5116.

LI, W. & ZHONG, W. (2015). CFD simulation of hydrodynamics of gas-liquid-solid three-phase bubble column. *Powder Technology*, 286. p. 766–788.

LIAO, D.L., WU, G.S. & LIAO, B.Q. (2009). Zeta potential of shape-controlled TiO2 nanoparticles with surfactants. *Colloids and Surfaces A: Physicochemical and Engineering Aspects*, 348(1–3). p. 270–275.

LIU, Y. & HINRICHSEN, O. (2014). Study on CFD-PBM turbulence closures based on k-ε and Reynolds stress models for heterogeneous bubble column flows. *Computers and Fluids*. 105. p. 91–100.

MASOOD, R.M.A., RAUH, C. & DELGADO, A. (2014). CFD simulation of bubble column flows: An explicit algebraic Reynolds stress model approach. *International Journal of Multiphase Flow*. 66. p. 11–25.

MEI, R. & KLAUSNER, J. (1994). Shear lift force on spherical bubbles. International *Journal*

*of Heat and Fluid Flow*. 15(1). p. 62–65.

MOHAJERANI, M., MEHRVAR, M. & EIN-MOZAFFARI, F. (2012). Computational Fluid Dynamics (CFD) Modeling of Photochemical Reactors. *Applied Computational Fluid Dynamics*. p. 155–176.

MONTGOMERY, D.C. (2012). Design and Analysis of Experiments 7th ed.,

NASTAR, M. & RAMASAR, V. (2012). Transition in south african water governance: Insights from a perspective on power. *Environmental Innovation and Societal Transitions*. 4. p. 7–24.

OCHIENG, A., ODIYO, J. & MUTSAGO, M. (2003). Biological treatment of mixed industrial wastewaters in a fluidised bed reactor. *Journal of Hazardous Materials*. 96(1). p. 79–90.

OHNO, T., SARUKAWA, K., TOKIEDA, K. & MATSUMURA, M. (2001). Morphology of a TiO2 Photocatalyst (Degussa, P-25) Consisting of Anatase and Rutile Crystalline Phases. *Journal of Catalysis*. 203(1). p. 82–86.

OLMOS, E., GENTRIC, C., VIAL, CH., WILD, G. & MIDOUX, N. (2001). Numerical simulation of multiphase flow in bubble column reactors. Influence of bubble coalescence and break-up. *Chemical Engineering Science*. 56(21–22). p. 6359–6365.

PETROVIĆ, S., STOJADINOVIĆ, S., ROŽIĆ, LJ., RADIĆ, N., GRBIĆ, B. & VASILIĆ, R. (2015). Process modelling and analysis of plasma electrolytic oxidation of titanium for TiO2/WO3 thin film photocatalysts by response surface methodology. *Surface and Coatings Technology*. 269. p. 250–257.

PFLEGER, D. & BECKER, S. (2001). Modelling and simulation of the dynamic flow behaviour in a bubble column. *Chemical Engineering Science*. 56(4). p. 1737–1747.

POURTOUSI, M., GANESAN, P. & SAHU, J.N. (2015). Effect of bubble diameter size on prediction of flow pattern in Euler-Euler simulation of homogeneous bubble column regime. Measurement: *Journal of the International Measurement Confederation*. 76. p. 255–270.

POURTOUSI, M., SAHU, J.N. & GANESAN, P. (2014). Effect of interfacial forces and turbulence models on predicting flow pattern inside the bubble column. *Chemical*

*Engineering and Processing: Process Intensification*. 75. p. 38–47.

PRIMO, O., RIVERO, M.J., ORTIZ, I. & IRABIEN, A. (2007). Mathematical modelling of phenol photooxidation: Kinetics of the process toxicity. *Chemical Engineering Journal*. 134(1–3). p. 23–28.

QI, N., ZHANG, HU., JIN, BO. & ZHANG, K. (2011). CFD modelling of hydrodynamics and degradation kinetics in an annular slurry photocatalytic reactor for wastewater treatment. *Chemical Engineering Journal*. 172(1). p. 84–95.

RUIZ, J., KAISER, A.S., ZAMORA, B., CUTILLAS, C.G. & LUCAS, M. (2015). CFD analysis of drift eliminators using RANS and LES turbulent models. *Applied Thermal Engineering*. 105. p. 979–987.

SAIEN, J. & NEJATI, H. (2007). Enhanced photocatalytic degradation of pollutants in petroleum refinery wastewater under mild conditions. *Journal of Hazardous Materials*. 148(1–2). p. 491–495.

SANONGRAJ, W., CHEN, Y., CRITTENDEN, J.C., DESTAILLATS, H., HAND, D.W., PERRAM, D.L. & TAYLOR, R. (2007). Mathematical Model for Photocatalytic Destruction of Organic Contaminants in Air. *Journal of the Air & Waste Management Association*. 57(9). p. 1112–1122.

SANTARELLI, C. & FRÖHLICH, J. (2015). Direct Numerical Simulations of spherical bubbles in vertical turbulent channel flow. *International Journal of Multiphase Flow*. 75. p. 174–193.

SANTARELLI, C. & FRÖHLICH, J. (2016). Direct Numerical Simulations of spherical bubbles in vertical turbulent channel flow. Influence of bubble size and bidispersity. *International Journal of Multiphase Flow*. 81. p. 27–45.

SARKAR, S., BHATTACHARJEE, C. & CURCIO, S. (2015). Studies on adsorption, reaction mechanisms and kinetics for photocatalytic degradation of CHD, a pharmaceutical waste. *Ecotoxicology and Environmental Safety*. 121. p. 154–163.

SATO, Y., SADATOMI, M. & SEKOGUCHI, K. (1981). Momentum and heat transfer in two-phase bubble flow-I. Theory. *International Journal of Multiphase Flow*. 7(2). p. 167–177.

SHAHREZAEI, F., MANSOURI, Y., ZINATIZADEH, A.S.L. & AKHBARI, A. (2012a). Photocatalytic degradation of aniline using TiO 2 nanoparticles in a vertical circulating photocatalytic reactor. *International Journal of Photoenergy*. 2012. p. 1–8.

SHAHREZAEI, F., MANSOURI, Y., ZINATIZADEH, A.S.L. & AKHBARI, A. (2012b). Process modeling and kinetic evaluation of petroleum refinery wastewater treatment in a photocatalytic reactor using TiO 2 nanoparticles. *Powder Technology*. 221. p. 203–212.

SHET, A. & VIDYA, S.K. (2016). Solar light mediated photocatalytic degradation of phenol using Ag core – TiO2 shell (Ag@TiO2) nanoparticles in batch and fluidized bed reactor. *Solar Energy*. 127. p. 67–78.

SHIOTA, T., SATO, Y., KISHI, T. & YASUDA, K. (2016). Photon emission induced by brittle fracture of borosilicate glasses. *Journal of Luminescence*. 173. p. 208–212.

SILVA, M.K., D'ÁVILA, M.A. & MORI, M. (2012). Study of the interfacial forces and turbulence models in a bubble column. *Computers and Chemical Engineering*. 44. p. 34–44.

SMAGORINSKY, J. (1963). General circulation experiments wiht the primitive equations I. The basic experiment. *Monthly Weather Review*. 91(3). p. 99–164.

TABIB, M. V., ROY, S.A., JOSHI, J.B., (2008). CFD simulation of bubble column-An analysis of interphase forces and turbulence models. *Chemical Engineering Journal*. 139(3). p. 589–614.

WANG, Z., LIU, J., DAI, Y., DONG, W., ZHANG, S. & CHEN, J. (2012). CFD modeling of a UV-LED photocatalytic odor abatement process in a continuous reactor. *Journal of Hazardous Materials.* 215–216. p. 25–31.

XI, W. & GEISSEN, S.U. (2001). Separation of titanium dioxide from photocatalytically treated water by cross-flow microfiltration. *Water Research*. 35(5). p. 1256–1262.

ZHANG, D., DEEN, N.G. v KUIPERS, J.A.M. (2006). Numerical simulation of the dynamic flow behavior in a bubble column: A study of closures for turbulence and interface forces. *Chemical Engineering Science*. 61(23). p. 7593–7608.

ZULFAKAR, M., HAIRUL, N.A.H., AKMAL, H.M.R. & RAHMAN, M.A. (2011).

Photocatalytic degradation of phenol in a fluidized bed reactor utilizing immobilized TiO2 photocatalyst: Characterization and process studies. *Journal of Applied Sciences*. 11(13). p. 2320–2326.

# APPENDICES

## Appendix A (Grid independence study results)

Figure A-1 shows the simulation data from a grid independence study. The grid independence study was conducted by keeping all the CFD settings (time step size, discretization scheme and turbulence model) constant for all cases. The simulation data was compared to experimental results obtained from Kulkarni et al., 2007. Figure A-1 shows a comparison between the simulation and the experimental results where the local gas hold-up was used as a response.

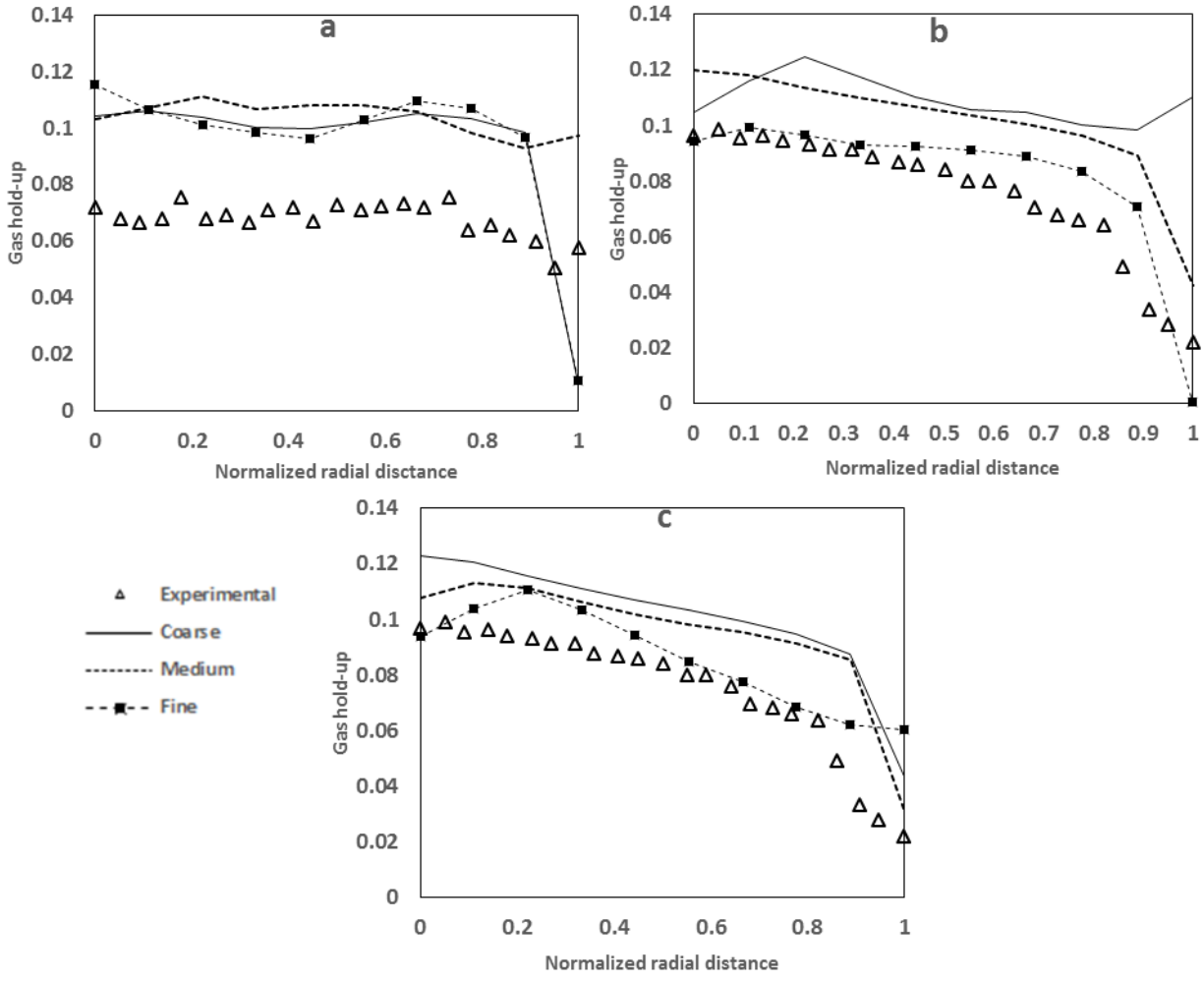


**Figure A-1:** Grid independent study; comparison between simulation and experimental results.

## Appendix B (CFD optimization results)

The simulations were conducted by varying the CFD settings (time step size, discretization scheme and grid size) that had a significant influence on the simulation accuracy and convergence. The varying of the CFD settings was done by using a 3-level factorial design which enables the study of the interdependency of the CFD settings and the simulation data was compare to Kulkarni et al., 2007. Table B-1 shows the ANOVA design from the 3-level factorial study where significance of the model is shown.

**Table B-1:** Analysis of variance for selected factorial optimization study.

| Source | Sum of Squares | DF | Mean Square | F Value | Prob > F | |
|---|---|---|---|---|---|---|
| Model | 0.097 | 12 | 8.13E-03 | 4.1 | 0.02128 | Significant |
| *E* | 0.012 | 1 | 0.012 | 6.15 | 0.01314 | |
| *F* | 0.016 | 2 | 8.12E-03 | 4.09 | 0.01964 | |
| *G* | 0.02 | 2 | 9.99E-03 | 5.04 | 0.01657 | |
| *EF* | 9.90E-03 | 2 | 4.95E-03 | 2.49 | 0.02862 | |
| *EG* | 0.034 | 2 | 0.017 | 8.49 | 0.01053 | |
| *RG* | 0.027 | 3 | 9.00E-03 | 4.53 | 0.01859 | |
| Residual | 3.97E-03 | 2 | 1.98E-03 | | | |
| Cor Total | 0.1 | 14 | | | | |

*E* – Number of cells, *F* – Discretization scheme and *G* – Time step size

The developed empirical polynomial model is shown by Equation B1. It was developed through the statistical optimization study using Design Expert® Software of Stat-Ease Inc. (version 6.0.6). The developed model can be used to determine the percentage error of the simulation results.

$$\%Error = 0.034 - 0.00432E + 0.091\mathrm{F} + 0.083\mathrm{G} - 0.037EF + 0.068\mathrm{EG} - 0.11\mathrm{FG} \ldots\ldots\ldots (\mathrm{B1})$$

**Table B-2:** Diagnostics case statistics.

| Run | Actual Value | Predicted Value |
|---|---|---|
| 1 | 0.014 | -0.006 |
| 2 | 0.175 | 0.195 |
| 3 | 0.015 | 0.039 |
| 4 | 0.181 | 0.157 |
| 5 | 0.131 | 0.127 |
| 6 | 0.184 | 0.188 |
| 7 | 0.243 | 0.243 |
| 8 | 0.109 | 0.109 |
| 9 | 0.020 | 0.020 |
| 13 | 0.020 | 0.040 |
| 14 | 0.190 | 0.170 |
| 15 | 0.015 | -0.009 |
| 16 | 0.013 | 0.037 |
| 17 | 0.024 | 0.028 |
| 18 | 0.022 | 0.018 |

## Appendix C (Vector plots)

Figures C-1 to C3 show the velocity vector plot of the axial liquid velocity at different locations in the reactor. The most significant fluid sections in the reactor were inlets and outlets for both fluids (water & air). The velocity vector graphs were helpful in visualizing turbulent swirling profiles and areas of fully developed flow.

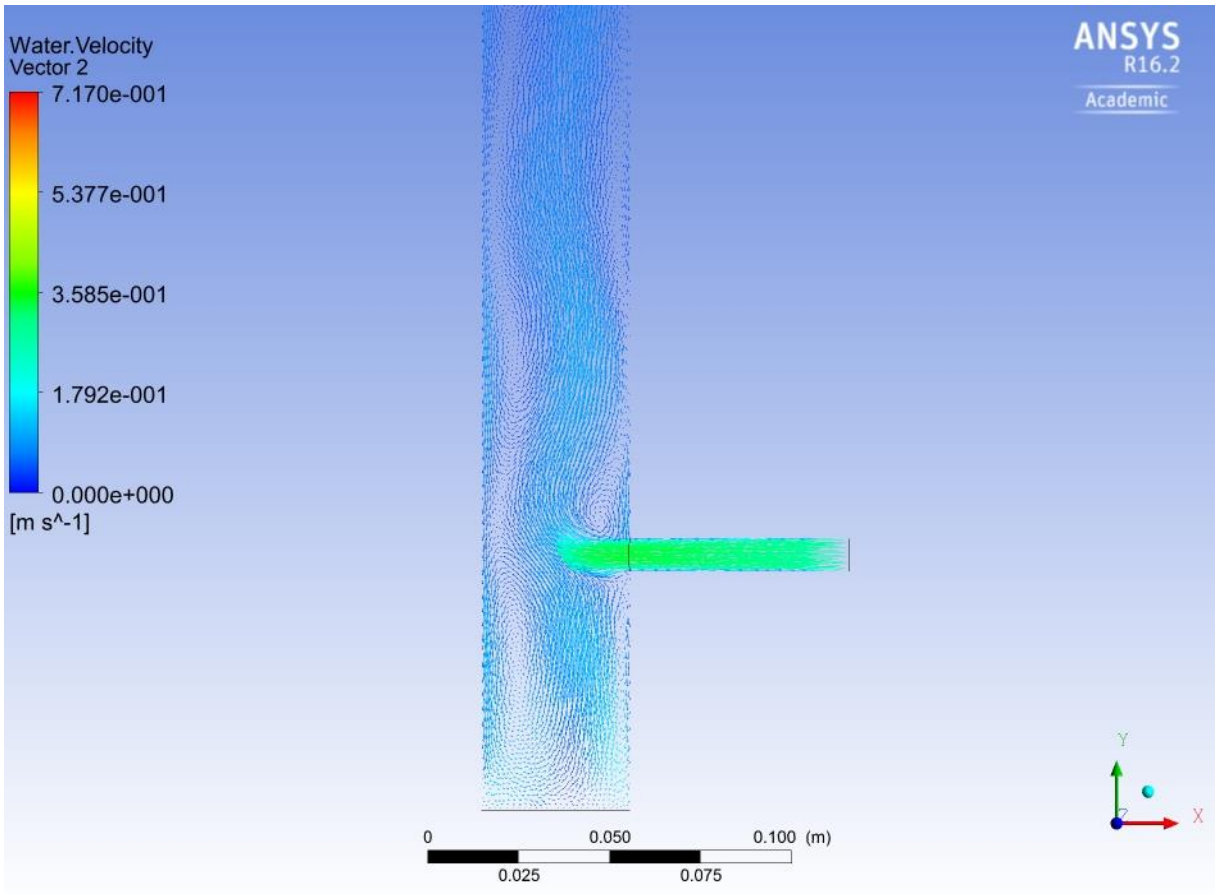


**Figure C-1:** Vector plot for axial liquid velocity at the distributor zone.

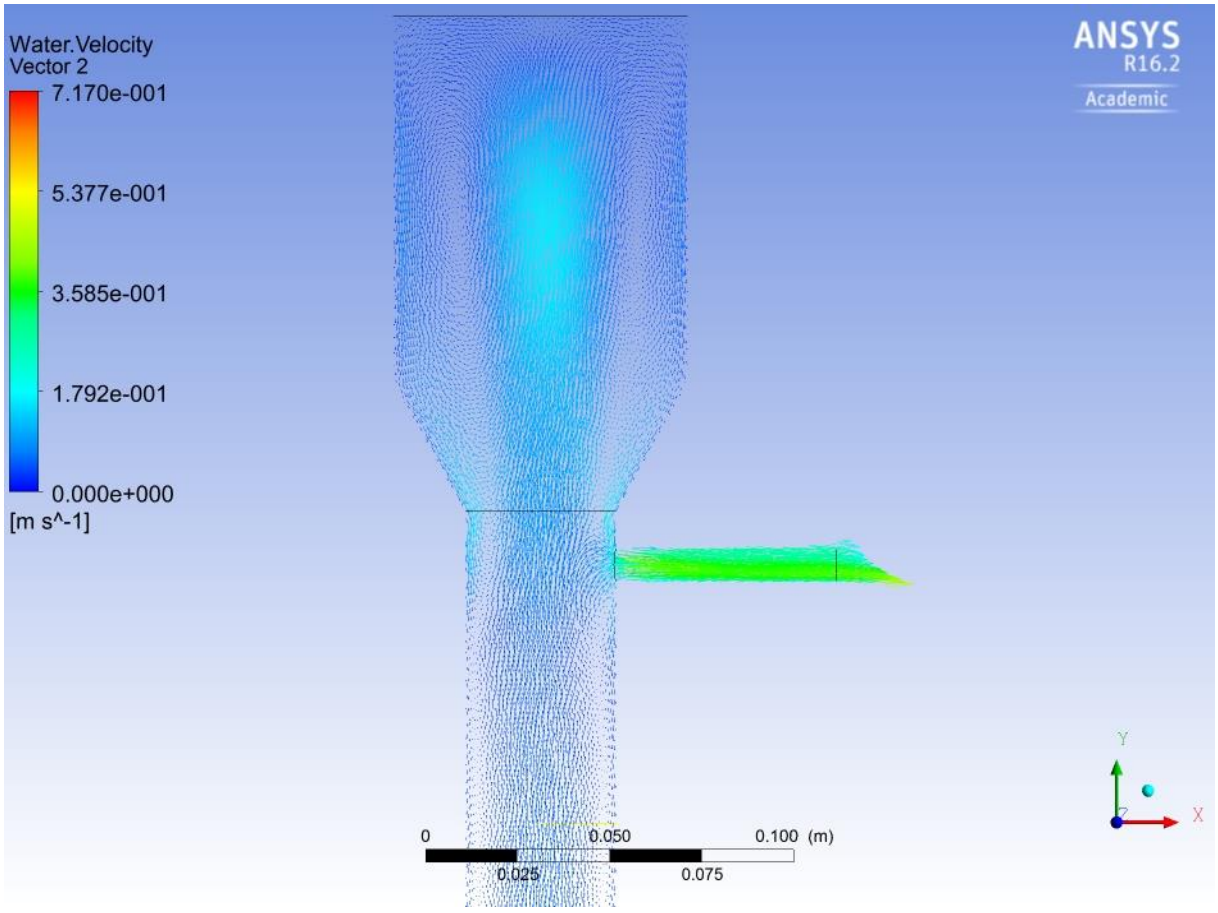


**Figure C-2:** Vector plot for axial liquid velocity at the disengagement zone.

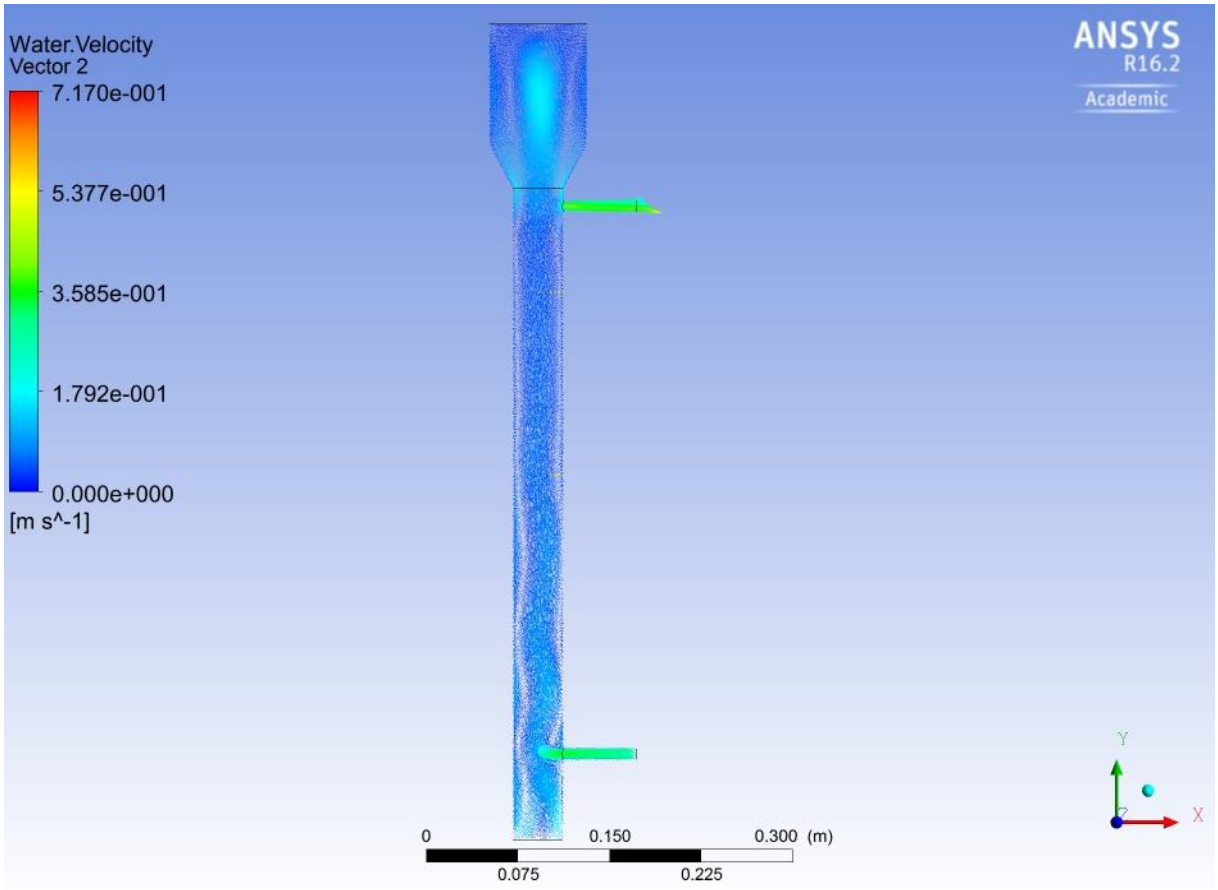


**Figure C-3:** Vector plot for axial water velocity for the entire computational domain.

## Appendix D (Contour plots)

Figures D1 and D2 show contour plots of the gas volume fraction at different locations in the reactor. The contour plots were helpful in determining as to where is the gas concentrated as it flows up the reactor.

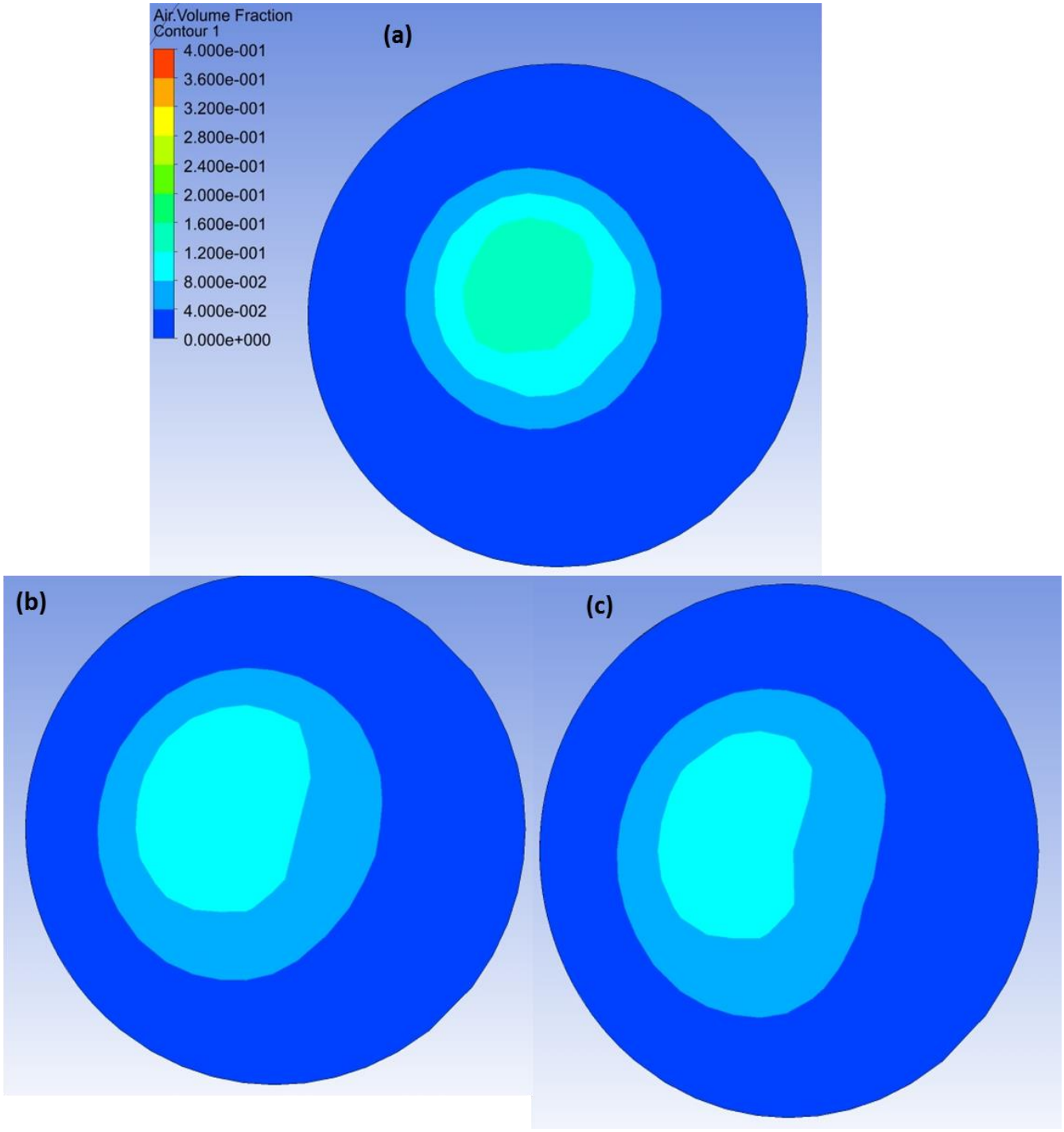


**Figure D-1:** Contour plot of aerial view for local gas hold-up at three axial positions.

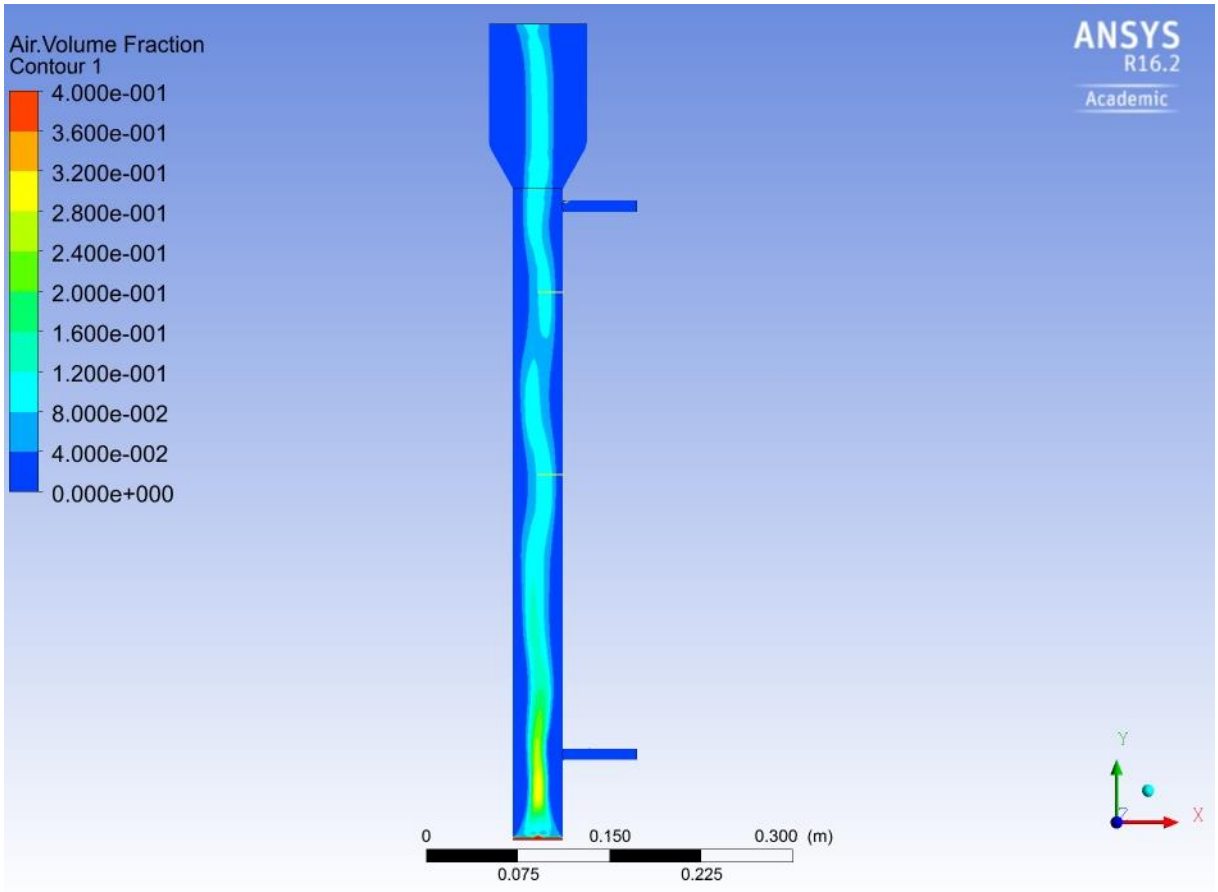


**Figure D-2:** Contour plot of local gas hold-up for the entire computational domain.

## Appendix E (Computational domain study)

Figures E-1 and E-2 show a preliminary simulation study that was done to determine the effect of decreasing the computational domain.

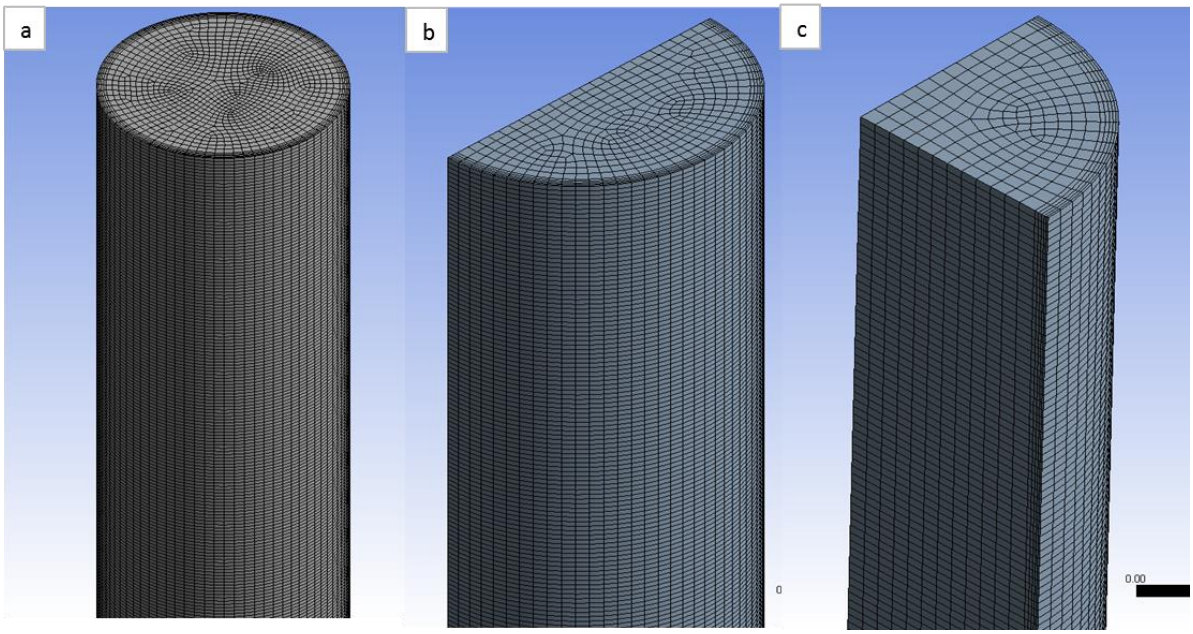


**Figure E-1:** Simulation grids for three different computational sizes. (a) Full; (b) Half and (c) Quarter.

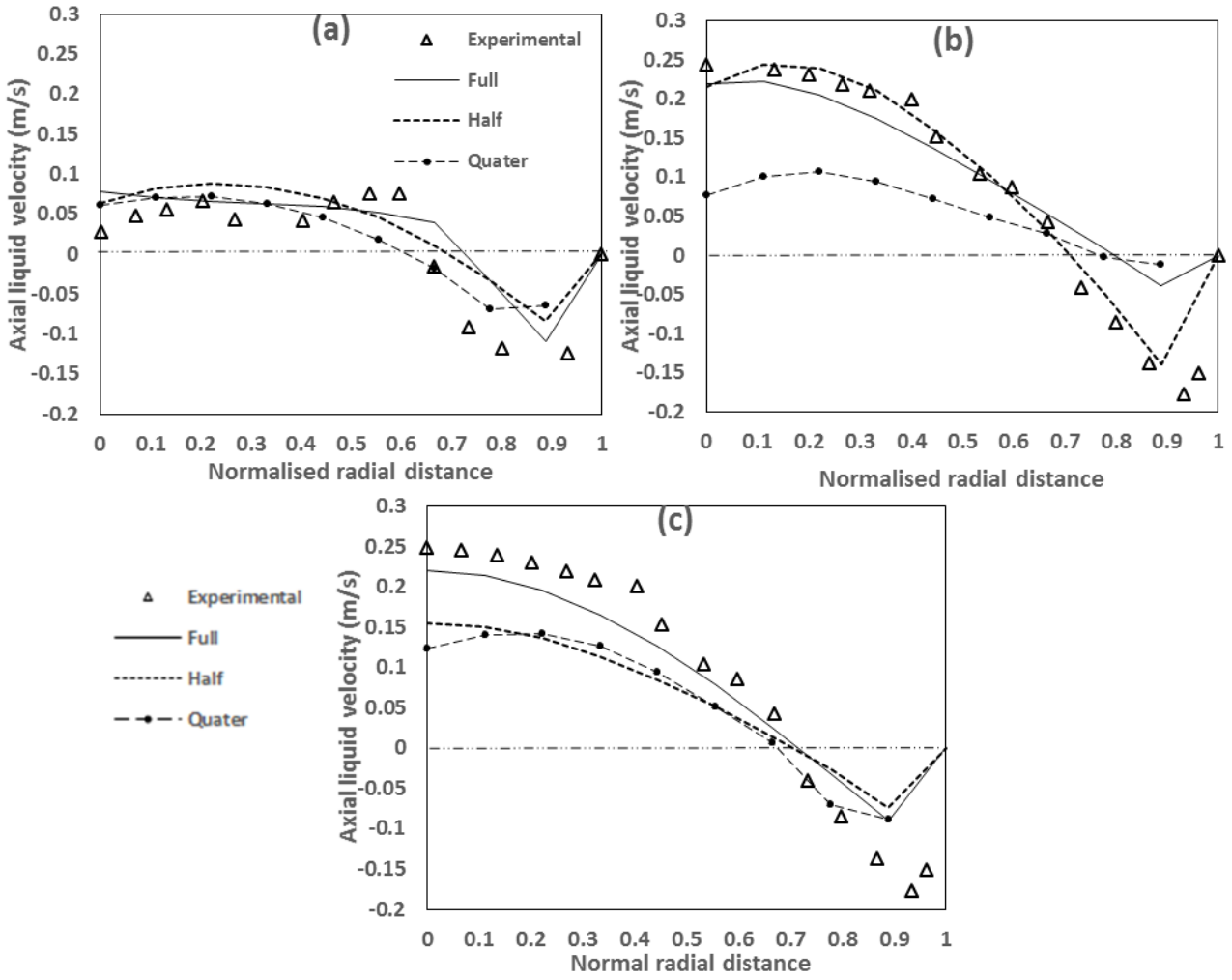


**Figure E-2:** Comparison between simulation and experimental results for axial liquid velocity at different computational domain sizes.

## Appendix F (List of equations)

Bubble induced turbulence is as a result of the displacement of the liquid phase caused by the gas flowing through the liquid phase (Zhang et al., 2006). Sato et al. (1981) used this model (Equation 44) to predict the bubble induced turbulence in bubble column reactors.

$$\mu_{BIT,l} = \rho_L C_{\mu,BIT} \in_G d_B |u_G - u_L| \tag{F1}$$

where $d_B$ is the bubble diameter and $C_{\mu,BIT}$ is a model constant set to 0.6 in accordance with previous studies (Masood et al., 2014; Pourtousi et al., 2015). The interphase force term is due to phenomena such as cohesion, friction, pressure and other effects, therefore, a suitable expression that is linked to the interphase force term is needed to close Equation 40.

$$\sum_{j=1}^{n} \vec{F}_k = \sum_{j=1}^{n} K_{gl}\left(\vec{u}_g - \vec{u}_l\right) \tag{F2}$$

where $\vec{u}_g$ and $\vec{u}_l$ are the gas and liquid phases velocities and $K_{gl}$ is the interphase momentum exchange coefficient.

In fluid-fluid flow scenarios, the secondary phases are considered to be bubbles or particles. For example, when modelling a bubble column reactor that consists of a liquid phase and a gas phase (unequal amount of phases), the liquid phase is modelled as the primary fluid due to the fact that the gas phase will form bubbles or droplets (dispersed). The momentum interphase exchange coefficient in such processes is described by:

$$K_{gl} = \frac{\rho_g f}{6\tau_g} d_g A_i \tag{F3}$$

where $f$ is the friction function and is expressed based on the respective interphase exchange coefficient model, $A_i$ is the interfacial transfer area and $\vartheta_k$ is the particulate relaxation time:

$$\vartheta_k = \frac{\rho_g d_g^2}{18\mu_g} \tag{F4}$$

where $\mu_g$ and $d_g$ are the viscosity and diameter of the secondary phase, respectively.

The interfacial area is a cross sectional area that exists when two different phases come into contact and is expressed per unit volume of mixture. The modelling of this variable is very essential due to the fact that it assists in predicting the transfer of energy, momentum and mass from one fluid to another. Therefore, when modelling a multiphase reactor using the Eulerian model, the interfacial area was calculated by resolving the algebraic relationship between the interfacial area concentration and the bubble diameter specified (ANSYS, 2010). The interfacial area model originates from the surface area to volume ratio of the particle (Equation F5).

$$A_i = \frac{\pi d_g^2}{\frac{1}{6}\pi d_g^3} = \frac{6}{d_p} \tag{F5}$$

However, there are various algebraic interfacial area models that can be used to model the interfacial area. In the current study, the Symmetric Model was used (Equation F6). The diversity of this model is that it includes the volume fraction that directs the interfacial area concentration to approach 0 as the volume fraction approaches 1 (ANSYS, 2010).

$$A_i = \frac{6 \in_g \left(1 - \in_g\right)}{d_g} \tag{F6}$$

**Modelling interfacial drag force**

The terminal rise velocity of the bubble and is given by (ANSYS, 2010):

$$u_T = \frac{\mu_l}{\rho_l d_b} Mo^{-0.149}\left(J - 0.857\right) \tag{F7}$$

where *Mo* is the Morton number related to the fluid property and is defined by:

$$Mo = \frac{\mu_l^4 g \Delta\rho}{\rho_l^2 \sigma^3} \tag{F8}$$

where $\sigma$ is the surface tension and *J* is given by the piecewise function:

$$J = \begin{cases} 0.94H^{0.757} & 2 < H \le 59.3 \\ 3.42H^{0.441} & \mathrm{H} > 59.3 \end{cases} \tag{F9}$$

*H* is expressed as:

$$H = \frac{4}{3} EoMo^{-0.149} \left( \frac{\mu_l}{\mu_{ref}} \right)^{-0.14} \tag{F11}$$

where $\mu_{ref}$ = 0.0009 kg/(m.s) is the reference viscosity of water at a specific temperature and pressure (Qi et al., 2011). *Eo* is the Eötvös number defined as:

$$Eo = \frac{g \Delta \rho d_b^2}{\sigma} \tag{F12}$$

**Modelling interfacial lift force**

The Saffman-Mei model was extended by Mei & Klausner, (1994) by empirically representing it as:

$$C'_L = \begin{cases} 6.46 \text{ x } f\left(\text{Re}_p, \text{Re}_\omega\right) & \text{Re}_\text{p} \le 40 \\ 6.46 \text{ x } 0.0524 \ \left(\beta \, \text{Re}_\text{p}\right)^{1/2} & 40 < \text{Re}_\text{p} < 100 \end{cases} \tag{F13}$$

where

$$\beta = 0.5 \left( \text{Re}_\omega \big/ \text{Re}_p \right) \tag{F14}$$

and

$$f\left(\text{Re}_p, \text{Re}_\omega\right) = \left(1 - 0.3314 \, \beta^{0.5}\right) e^{-0.1 \text{Re}_p} + 0.3314 \, \beta^{0.5} \tag{F15}$$

**Modelling interfacial wall lubrication force**

$y_w$ is the distance nearest to the wall and when:

$$y_w \le -\left( C_{w2} \big/ C_{w1} \right) d_b \tag{F16}$$

where the values of $C_{w2}$ and $C_{w1}$ become default when:

$$y_w \le 5 d_b \tag{F17}$$

**Turbulence modelling**

In the current study, the effect of the dispersed phase on the turbulence of the multiphase equations was considered since the Eulerian multiphase approach was used along with the standard *k-ε* turbulence model. The terms ($\prod_{\lg}$ and $\prod_{\alpha q}$) are representative of the source terms and are due to the influence of the dispersed phase. The instantaneous equation that is linked to the continuous phase, is derived from the source term $\prod_{\lg}$.

$$\prod_l = C_s \sum_{p=1}^{M} \frac{K_{\lg}}{\in_l \rho_l} X_{\lg} \left[ k_{\lg} - 2k_l + \vec{U}_{\lg} \cdot \vec{U}_{dr} \right] \tag{F18}$$

where $k_{lg}$ is the covariance of the velocities for the both the liquid and gas phase, $C_s$ is a user-modifiable model constant that was specified as 1 (default value), $\vec{U}_{\lg}$ is the relative velocity and $\vec{U}_{dr}$ is the drift velocity computed as:

$$\vec{U}_{dr} = -D_{\lg} \cdot \left( \frac{\nabla \in_g}{\in_g} - \frac{\nabla \in_l}{\in_l} \right) \tag{F19}$$

where $D_{\lg}$ is the fluid particulate dispersion tensor.

$$k_{\lg} = 2k_l \left( \frac{b + \eta_{\lg}}{1 + \eta_{\lg}} \right) \tag{F20}$$

$$k_g = k_l \left( \frac{b^2 + \eta_{\lg}}{1 + \eta_{\lg}} \right) \tag{F21}$$

$$X_{\lg} = \frac{\rho_g}{\rho_g + C_{VM} \rho_l} \tag{F22}$$

where $X_{\lg} \sim 1$ for granular flows.

The formulation of the turbulence models for the dispersed phase is shown by the characteristic particle relaxation time ($\vartheta_{gl}^{F}$) that is associated with the inertial effects that are exerted on the dispersed phase.

$$\vartheta_{gl}^{F} = \frac{\rho_l d_g^2}{18\mu_c f\left(\mathrm{Re}, \in_l\right)}\left(1 + C_{VM}\frac{\rho_l}{\rho_g}\right) \tag{F23}$$

The energetic turbulent eddies can be represented by the time scale ( $\vartheta_l^t$ ) that is described as:

$$\vartheta_l^t = \frac{3C_\mu k_l}{2 \in_l} \tag{F24}$$

The cross-trajectory is the main characteristic that affects the eddy particle interaction time ( $\vartheta_{gl}^t$ ) and is described as:

$$\vartheta_{gl}^t = \frac{\tau_l^t}{\sigma_1\sqrt{\left(1 + C_\beta \xi_\tau^2\right)}} \tag{F25}$$

where $\sigma_1$ is equated to 1 and $C_\beta$ is described as:

$$C_\beta = 1.8 - 1.35\cos^2\theta \tag{F26}$$

$\xi_\tau^2$ can be calculated as:

$$\xi_\tau^2 = \frac{\left|\vec{u}_g - \vec{u}_l\right|}{\sqrt{\frac{2k_l}{3}}} \tag{F27}$$